Estimating Cosmological Parameters and Cluster Masses through Escape Velocity Measurements in Galaxy Clusters

by

Daniel William Gifford

A dissertation submitted in partial fulfillment
of the requirements for the degree of
Doctor of Philosophy
(Astronomy and Astrophysics)
in The University of Michigan
2016

Doctoral Committee:

Assistant Professor Christopher Miller, Chair
Professor August E. Evrard
Associate Professor Oleg Gnedin
Assistant Professor Keren Sharon

I dedicate this thesis to my grandfather William Gifford. Thanks for the book Grandpa.

ACKNOWLEDGMENTS

I am incredibly grateful to everyone who has made this great journey possible through their love, support, and friendship. First and foremost, I would like to thank Christopher Miller, who has been a valued advisor and good friend throughout the last 5 years. Chris and I started at nearly the same time at the University of Michigan, and as his first graduate student, we learned how to work together and build a trusting relationship. Chris is always ready to ask great questions just when I think I have things figured out, and give me a boost when I need a hand with any part of my research. I also know that I can count on Chris when anything happens in my life to offer support. His contagious enthusiasm from his work has made life and research fun throughout my time as a graduate student.

My dissertation committee members, August Evrard, Oleg Gnedin, and Keren Sharon, have been so helpful in giving me feedback regarding my work to this point. They helped guide this thesis to completion by asking great questions and suggesting alternate routes Chris and I had not thought of previously. Thank you so much for all your support.

I want to thank all the people I have collaborated with on scientific projects, but especially the researchers in Chris Miller's group: Craig Harrison, Nicholas Kern, Alejo Stark, Jessica Kellar, and Jesse Golden-Marx. Thank you all so much for the great feedback through many different projects in my graduate career. All of you contributed and had a hand in the work I produced whether it be pulling data from databases, to finding errors in my sometimes messy code. You also made group

meetings open and exciting places to discuss our science. I look forward to seeing where all of your careers take you.

I appreciate the work of the department's administrative staff, especially Brian Cox, Jan Malaikal, and Anne Thompson, who ensured that my time here was smooth. They were always so eager to help and were ready to answer any question I had from booking trips, to registration, to reimbursement. Roy Bonser deserves an award for all the work he has done to keep my research running smoothly when machines decide to break. I also want the thank the others who have worked with Roy over my time here to help him do such a great job for this department. Eric Galayda who is the site manager at the MDM telescope also deserves a special thank you for making my many observing trips to the mountain a great experience.

Before graduate school, I had many mentors who helped guide me as a growing scientist. I would like the thank Mark Harris, my junior high science teacher for showing me that science can be cool at a time when that's all you want to be. Thank you to Ken Slavens and Alice Few as well as all the members of the Tacoma Astronomical Society for introducing me to this amazing field and inspiring young minds to look up and take in the universe. Kenneth Rines and Kristen Larson co-advised me throughout my undergraduate physics degree. Both of them provided me with research opportunities inside the department, and helped me secure a valuable summer research experience at the Smithsonian Astrophysical Observatory before my senior year. At the SAO, I want to thank Matthew Ashby for teaching me everything he knows about the IRAC instrument on Spitzer, and especially my fellow REU classmates for all the ultimate frisbee one could hope for in a summer.

My classmates and professors at Michigan have helped make my time here unforgettable. Thank you for all the good times, difficult tests, and surprise birthday decorations on my desk. To Matthew Miller and Brian Devour, thank you both for being amazing friends and office mates. Both of you have seen me at my highest and

lowest points and were there every step of the way celebrating the highs and supporting me in every way possible during the lows. I will miss our great conversations on everything from sports to the art of building Hot Wheel car tracks.

Last, but certainly not least, I want to thank my friends and family both here and afar for all their love over these past 5 years. First, I need to thank my Grandpa who is the reason I am here studying astronomy. Little did he know that book he purchased for me on the night sky as a young teenager would spark an interest that would take me on journeys both here in the U.S and abroad. Thanks for the book Grandpa. To the Bandits, thanks for keeping a constant smile on my face and reminding me to book that trip to Disney World. To my second set of parents Tom and Joan Butler, thank you for all of your love through this time in my life. Most of all, thank you for allowing me to take your daughter halfway across the country for half a decade to study the science that interests us. To my sister Amanda, thank you for not copying me by going to Michigan for school. I am so proud of the work you are doing teaching young minds, and you inspire me to work hard in everything I do and attack life great enthusiasm. I need to thank my parents for constantly believing in me and raising me to be the man I am today. My Mom read countless papers and my Dad drove me back and forth to TAS events every week for many years. You are both amazing role models, and I owe so much of my success to you. I cannot forget the golden retrievers who have been a part of my family throughout my life: Chance, Mojo, and Mowgli. I still don't know of a better sight when things get tough than a big happy dog pushing a tennis ball into your face. Thanks for all the laughs and games of chase. A huge thank you goes to my wife Gail, who I love, respect, and trust more with each passing day. Going through graduate school together has been a great challenge, but we have created so many wonderful memories starting our life together in Ann Arbor. Your attitude, especially during the last year, has been a constant reminder to me to smile and enjoy this wonderful life we share no matter what it throws at us. Thank you for

believing in me, making the most excellent desserts, and sharing your life with me.

I acknowledge support from an NSF Graduate Research Fellowship. Chapter 2, 3, 4, and 5 of this thesis is based on work published in *The Astrophysical Journal* (Gifford & Miller, 2013; Gifford et al., 2013) and work to be published (Miller et. al. in prep, Gifford et. al. in prep, Gifford & Miller in prep). The work that is published is reproduced here with permission with minor revisions. This material is based upon work supported by the National Science Foundation Graduate Student Research Fellowship under Grant No. DGE 1256260. Christopher Miller also supported this work with support by the National Science Foundation under Grant No. 1311820.

TABLE OF CONTENTS

LIST OF FIGURES

Figure

LIST OF TABLES

Table

ABSTRACT

Galaxy clusters are large virialized structures exist at the intersection of filaments of matter that make up the cosmic web. Due to their hierarchical growth history, they are excellent probes of the cosmology that governs our universe. Here, we aim to use clusters to better constrain cosmological parameters by systematically studying the uncertainties on galaxy cluster mass estimation for use in a halo mass function analysis. We find that the caustic technique is capable on average of recovering unbiased cluster masses to within 30% for well sampled systems. We also quantify potential statistical and systematic biases due to observational challenges. To address statistical biases in the caustic technique, we developed a new stacking algorithm to measure the average cluster mass for a single stack of projected cluster phase-spaces. By varying the number of galaxies and number of clusters we stack, we find that the single limited value is the total number of galaxies in the stack opening up the possibility for self-calibrated mass estimates of low mass or poorly sampled clusters in large surveys. We then utilize the SDSS-C4 catalog of galaxy clusters to place some of the tightest galaxy cluster based constraints on the matter density and power spectrum normalization for matter in our universe.

CHAPTER I

Introduction

1.1 Galaxy Clusters and Cosmology

Galaxy clusters represent the metropolitan centers in our universe. These large, virialized structures form through a combination of gravitational collapse and hierarchical merging at the intersection of filaments of matter that make up the cosmic web. Clusters therefore act as tracers of peaks in the large-scale matter density. The cosmology that governs the universe determines the distribution of matter within it, and therefore clusters offer a means to understand parameters which govern structure growth, matter density, and cosmic expansion. Clusters have been used to study cosmology since Zwicky first discovered dark matter in the Coma cluster Zwicky (1933). Hoessel et al. (1980) used Brightest Cluster Galaxies (BCGs) as standard candles and derived, albeit with low significance, that cosmic expansion is accelerating consistent with our current picture of cosmology. More recently, galaxy clusters have been used primarily in one of two ways to probe cosmology. The first way is through the halo mass function and cluster counts (Press & Schechter, 1974; Reiprich & Böhringer, 2002; Tinker et al., 2008; Vikhlinin et al., 2009; Rozo et al., 2010). The second, spatial clustering (both angular and 3D) of clusters, has also been used to understand the matter distribution of the universe (Bahcall & West, 1992; Mo et al., 1996; Colberg et al., 2000; Wang et al., 2008). Here, I focus on the former as it pertains to the

contents of this thesis.

The halo mass function builds upon the theory of spherical gravitational collapse of linearly evolved matter perturbations. Shown as a differential function of cluster mass, the functional form is

$$\frac{dn}{d\ln M} = \frac{\bar{\rho_m}}{M}\left|\frac{d\ln\sigma^{-1}}{d\ln M}\right| f(\sigma), \tag{1.1}$$

where $\bar{\rho}_m$ is the co-moving mean matter density, σ is the square root of the variance of linearly-evolved, CDM fluctuations, filtered on mass scale M, and $f(\sigma)$ is a function of the filtered perturbation spectrum. Despite the strong predictive power of analytic models based on spherical or elliptical collapse (Press & Schechter, 1974; Sheth & Tormen, 1999), they do not manage to account for all the complexity of halo formation and are therefore limited in their use in precision cosmology constraints. Instead, modern studies empirically fit for $f(\sigma)$ in N-body simulations which have resulted in much more precise calibrations of the halo mass function (Jenkins et al., 2001; Evrard et al., 2002; Tinker et al., 2008). Tinker et al. (2008) found that while their fit to the mass function in a suite of simulations is not universal (with respect to cosmology and redshift) in addition to an overall shape dependence with redshift, their models were still accurate to within 5%.

One of the fundamental challenges when matching a halo mass function to observations is that we do not directly observe cluster mass. Because clusters are dominated in mass by dark matter, we must instead rely on observable properties that arise from, or correlate strongly with, the total mass in order to utilize the halo mass function to constrain cosmological parameters. It is immediately obvious that we must have at our disposal not only the means to accurately estimate cluster mass, we must also clearly understand the uncertainties and potential systematic affects in our estimates. As I discuss below, cluster mass estimation plays a major role in both understand-

ing properties and evolution of clusters as well as making them viable cosmological tracers. In fact, there are observable proxies of mass in almost every waveband. In the X-ray, Borgani et al. (2001); Reiprich & Böhringer (2002) found a lower value for σ_8 than was previously accepted, and Vikhlinin et al. (2009) used x-ray clusters in several redshift bins to place constraints on Ω_Λ in addition to Ω_M and σ_8. In the optical, Rines et al. (2007) used dynamical mass estimates of 72 clusters within the SDSS DR4 footprint to constrain Ω_M and σ_8. Also in the optical, Rozo et al. (2010) calibrated a mass-richness scaling relation to constrain the same two parameters. Both authors folded in the latest WMAP results into their analysis to achieve even stronger constraints.

Accurately estimating cluster masses is now the limiting factor when using the halo mass function to constrain cosmology, as large surveys now in progress contain more than enough numbers to limit statistical uncertainties. Many large modern surveys rely on scaling relations between the total mass of the cluster and direct observables such as richness or velocity dispersion in the optical, SZ signal in the sub-millimeter, and X-ray luminosity/gas mass. Scaling relations between an observable and mass exist because of complex astrophysics and cluster assembly history. The exact parametrization of the relationship must then be calibrated via a more physical mass estimation technique such weak lensing, hydrostatic mass, or virial/caustic techniques (see below). However, these techniques themselves can impart biases resulting in incorrect scaling relation normalizations. For instance, comparison between weak lensing and hydrostatic mass estimates can exhibit differences anywhere between $0 - 30\%$ (von der Linden et al., 2014; Planck Collaboration et al., 2015; Hoekstra et al., 2015). Only the most extreme of these closes the gap between cosmological constraints reported by the first SZ cluster count analysis (Planck Collaboration et al., 2014b) and the Planck CMB anisotropy results (Planck Collaboration et al., 2014a). This highlights the need for a stronger understanding of the systematics involved

in all mass estimation techniques in order to reach the precision cosmology modern experiments seek to achieve.

1.2 Summary of Galaxy Cluster Mass Estimation

While galaxy clusters are composed mostly of dark matter, observers rely heavily on the baryonic, light-interacting components to identify and understand the nature of these objects. In fact, clusters are the only objects for which current technology enables three physically independent mass estimation techniques. The first, hydrostatic equilibrium through gas measurements, are measured in the x-ray through Bremsstrahlung radiation given off by hot 10^8K gas heated by the release of potential energy in addition to astrophysical interactions. The second, weak lensing, requires high resolution observations of large numbers of background galaxies to uncover the shear profile through statistical analysis. This technique also requires a detailed understanding of the background redshift distribution and, often times, accurate photometric redshift estimates. The third, cluster dynamics, utilizes the motions of galaxies within the cluster. Redshift measurements enable the use of virial and Jeans analyses in addition to escape velocity and other phase-space methods to recover the gravitational potential. All these techniques are directly related to the gravitational potential or its derivative and can be physically modeled to obtain accurate mass estimates. These physical mass estimation techniques usually make strong assumptions about the state of the cluster such as its radial density profile, equilibrium condition, or dynamic state.

In order to evaluate the total cluster mass through X-ray observations, one must assume that the gas is in hydrostatic equilibrium with the cluster gravitational potential. Under the assumption of spherical symmetry for an ideal gas, we can write

the pressure and potential gradients as,

$$\frac{dP}{dr} = \frac{d(k_B T \rho/\mu m_p}{dr}, \; \frac{d\Phi}{dr} = \frac{GM(r)}{r^2} \tag{1.2}$$

where $M(r)$ is the total mass within a radius r, ρ is the total mass density, ρ is the mass density of particles, m_p is the proton mass, and μ is the mean molecular weight of the gas. The equation of hydrostatic mass is then

$$M(r) = \frac{-k_B T(r) r}{\mu m_p G} \left[\frac{d \ln \rho}{d \ln r} + \frac{d \ln T}{d \ln r} \right]. \tag{1.3}$$

Given that both the density profile and temperature profile are observable in X-ray data, the total mass profile can be solved for. Of course, the gas can be in hydrostatic equilibrium, but also maintain pressure support through non-thermal turbulence, magnetic fields, or bulk motion. Failure to account for these effects can lead to biased mass estimates in addition to other uncertainties (Evrard et al., 1996; Rasia et al., 2006). Mahdavi et al. (2013) compared clusters observed in both X-ray with XMM-Newton and the Chandra space observatory with weak lensing measurements and find that non-cool core clusters are lower than weak lensing estimates by 15-20% at radii near r_{500} which could be due to the systematics listed above. X-ray gas is highly collisional which results in fast relaxation relative to other dynamical timescales. X-ray clusters also exhibit less triaxiality in their mass distributions within their central regions (Gavazzi, 2005). This is an advantage over dynamical and weak lensing methods which must account for velocity anisotropy as well as line-of-sight effects from cluster shape and large scale structure. There are several important difficulties when using hydrostatic mass estimates from X-ray observations. First, the X-ray flux is difficult to observe outside the very central region of the cluster ($r > r_{500}$). Observationally, X-ray detection must be performed in space as the earth's atmosphere absorbs this high-energy light. This limits the number and duration of

observations that can be performed simply due to observing time competition and priority. In an era where thousands of clusters are being studied via other techniques, X-ray comparison lags behind.

Weak lensing has grown in popularity with the advent of high resolution imaging platforms on the Hubble Space Telescope as well as adaptive optics systems on ground based observatories. The technique works by relating the two components of the shear and the convergence to the derivative of the lensing potential

$$\kappa = 0.5\nabla^2_\theta \Psi, \tag{1.4}$$

$$\gamma_1 = 0.5(\partial^2_1 \Psi \partial^2_2 \Phi), \tag{1.5}$$

$$\gamma_2 = \partial^2_{12} \Psi. \tag{1.6}$$

A spherically symmetric mass distribution will induce a shear tangentially to the radial vector. The lensing signal is measured in terms of the azimuthally averaged surface mass density contrast and is related to the projected tangential shear of source galaxies as well as the critical mass density. As a mass estimator, weak lensing is attractive because it is the only observable related to the potential that doesn't depend on baryonic astrophysics within the cluster. As mentioned above, X-ray estimates must assume the gas is in hydrostatic equilibrium, but must also contend with heating effects from AGN and various non-thermal effects. Dynamical mass estimators must rely on the assumption that the galaxies and dark matter density profiles and velocities trace the gravitational potential in similar ways. Weak lensing is not without its own challenges. The shear and convergence from the lensing observations are measured under the thin lens approximation. This assumes that the scale of the lens is much smaller than the distance the photons travel from the background source to the lens and the lens to the observer. As a cluster is often not in isolation, large scale structure often will influence the final lensing observables. Becker & Kravtsov

(2011) investigated how correlated and uncorrelated large scale structure around a cluster can effect mass estimates. They found that correlated structure contributes 20-30% to the scatter in weak lensing observations. They show that the scatter in low mass halos is dominated by uncorrelated large scale structure, and large halos have scatter dominated by correlated large scale structure and triaxiality. Becker & Kravtsov (2011) also found a small but non-negligible bias of 5-10%. This bias can be attributed to several factors including incorrect density fitting function, substructure in cluster outskirts, and applying the assumption of a spherically symmetric density model to a triaxial system. Averaging can help mitigate the last of these potential biases (Corless & King, 2007). Hoekstra et al. (2011) found that uncorrelated large scale structure along the line of sight does not bias weak lensing estimates, but does add an additional 15-30% which depends on cluster mass. Weak lensing estimates are also limited by the mass-sheet degeneracy where the surface mass density can only be determined up to a degeneracy transformation that depends on an arbitrary constant; however, if the redshift distribution of background galaxies is known, the degeneracy can be broken (Seitz & Schneider, 1997; Bradač et al., 2004). Another area weak lensing struggles is in estimating masses for low-mass clusters. This is becoming less of a problem as ground-based telescope resolution continues to improve, but measuring the statistical shear pattern for low mass systems requires a large number of highly resolved background galaxies.

Using galaxy dynamics is one of the most widely used and classic ways to constrain cluster mass distributions. One of the ways to do so is by solving the Jeans equations relating the gravitational potential to various intrinsic velocity moments. The most used Jeans equation for a spherical system is

$$-\frac{d\Phi}{dr} = \frac{1}{\rho}\frac{d(\rho\langle v_r^2\rangle)}{dr} + 2\beta\frac{\langle v_r^2\rangle}{r}, \tag{1.7}$$

where $\beta(r)$ is the velocity anisotropy parameter,

$$\beta(r) = 1 - \frac{\langle v_t^2 \rangle(r)}{\langle v_r^2 \rangle(r)} \tag{1.8}$$

The gravitational acceleration $d\Phi/dr = GM_{tot}(r)/r^2$ can help us rewrite the Jeans equation as

$$M_{tot}(r) = \frac{\langle v_r^2 \rangle r}{G} \left[\frac{d \ln \rho}{d \ln r} + \frac{d \ln \langle v_r^2 \rangle}{d \ln r} + 2\beta \right]. \tag{1.9}$$

Unfortunately, the projected velocity dispersion depends on $\langle v_r^2 \rangle$ and $\beta(r)$. Because there is no unique solution for $M_{tot}(r)$, an independent estimate is necessary to break the mass-anisotropy degeneracy. Another traditional dynamical mass estimator is the virial mass (Carlberg et al., 1996). The virial mass is defined as

$$M_v = \frac{3}{G} \sigma^2 r_v \tag{1.10}$$

where r_v is the 3-dimensional virial radius and σ is the line-of-sight velocity dispersion. The virial mass is a simple prescription for estimating total cluster mass, but requires the cluster to be in virial equilibrium. This also neglects a surface pressure term that can bias the mass estimates. The advantage of using dynamics is the ease of data collection. Galaxy redshifts are already measured in large numbers in modern surveys, and many telescopes host a spectrograph with sufficient resolution to obtain redshift estimates suitable for cluster dynamical studies. Unbiased velocity dispersions can be measured with as little as 25 galaxies (White et al., 2010; Saro et al., 2013) making it feasible to measure enough redshifts for a good mass estimate in one pass with a multi-slit or fiber-fed spectrograph. The challenges faced in dynamical mass estimation mainly come from the effects of cluster shape and projection. Estimating a projected velocity dispersion first requires separating the member galaxies from the foreground and background populations along the line-of-sight. Most studies have traditionally

used some type of velocity clipping to identify the member population (Fadda et al., 1996), while more sophisticated methods like the C4 algorithm address this challenge by using color-color and redshift information (Miller et al., 2005). Regardless, many clusters have been shown to exhibit prolate shapes (Saro et al., 2013) that, when observed down either the major or minor axis, can influence the projected velocity dispersion and therefore the mass estimate. Currently, there is no way to account for this effect, and it remains a limiting systematic to the Jeans and virial mass estimates.

Ideally, we would like to have a technique that allows for mass estimates of large numbers of clusters individually but has low scatter, is relatively insensitive to triaxiality, and avoids baryonic astrophysical biases. The only physical mass estimation technique currently capable of individually measuring masses for large number of cluster across a large mass range is dynamics. Dynamical techniques are well studied and methods for interloper rejection already exist to decrease the effects of l.o.s systematics. While the virial theorem and Jeans analysis have been around a very long time, potential improvements upon these techniques are limited given the assumptions they make. Recently, a new brand of dynamical mass estimators use radius-velocity phase-spaces to estimate mass (Diaferio, 1999; Wojtak & Łokas, 2010; Mamon et al., 2013). While in their infancy, leveraging phase-space information may prove to reduce the uncertainties on individual mass estimates and relax some of the assumptions made in the methods highlighted above.

1.3 The Caustic Mass Estimation Technique

1.3.1 Inferring Mass from the Escape Velocity Measurement

One dynamical phase-space technique that shows promise with the advent of large, well sampled optical surveys of clusters is the caustic technique (Diaferio & Geller, 1997; Diaferio, 1999). The term "caustic" refers to the velocity edge visible in

radius-velocity phase-space that defines the escape velocity profile of the cluster. The characteristic trumpet shape associated with these features is due to spherical infall (Kaiser, 1987) and is identifiable to well outside the virialized region where cluster mass is typically estimated. The technique relies on the physical trait that under Newtonian dynamics, the escape velocity is related to the gravitational potential of the system,

$$v_{esc}^2(r) = -2\Phi(r). \tag{1.11}$$

Galaxies that have not escaped and whose dynamics are dominated by the gravitational potential of the galaxy cluster will exist in a well defined region of $r - v$ phase-space, where r is the physical or projected cluster-centric distance/radius and v is the 3-dimensional or projected 1-dimensional velocity respective to the bulk cluster motion. Given these characteristics, the edge of this region defined by an iso-density contour that contains the bound member galaxies of the cluster, defines $v_{esc}(r)$.

Once the escape velocity is identified, the most straightforward way to estimate the density profile is through the Poisson equation,

$$\nabla^2\Phi(r) = 4\pi G\rho(r). \tag{1.12}$$

Because we directly measure $\Phi(r)$ through the caustic surface, we must differentiate it multiple times to recover the density profile; however, the estimated escape velocity profile can be noisy, and differentiating a noisy function will result in unphysical mass profiles (cumulative mass $< r$ cannot decrease). One way of dealing with this would be to fit a smooth, constantly decreasing function to the escape velocity profile, but another is to utilize the partial mass equation,

$$dm = 4\pi r^2\rho(r)dr. \tag{1.13}$$

By multiplying the right hand side of the Equation 1.13 by $v_{esc}^2(r)/-2\Phi(r)$, which is unity by the argument in Equation 1.11, multiplying each side by the gravitational constant and integrating,

$$GM(<R) = \int_0^R -2G\pi v_{esc}^2(r)\frac{\rho(r)r^2}{\Phi(r)}dr, \tag{1.14}$$

where R is the radius within which the cumulative mass is estimated. Of the terms in Equation 1.14, $\rho(r)$ and $\Phi(r)$ cannot be directly measured. In the caustic technique, we measure the escape velocity v_{esc} with full 3D phase space information in simulations or the line-of-sight escape velocity $\langle v_{los,esc}^2\rangle(r)$ in real and mock observations of galaxy clusters. The line-of-sight measurement is related to the full escape velocity by $v_{esc}^2(r) = g(\beta(r))\langle v_{los,esc}^2\rangle(r)$ where $g(\beta(r))$ is derived in Diaferio (1999) and is defined as,

$$g(\beta(r)) = \frac{3-2\beta(r)}{1-\beta(r)}, \tag{1.15}$$

and $\beta(r)$ is the velocity anisotropy parameter,

$$\beta(r) = 1 - \frac{\sigma_\theta^2+\sigma_\phi^2}{\sigma_r^2}. \tag{1.16}$$

For isotropic systems, $\beta = 0.0$ and $g(\beta) = 3.0$ which is commonly used to convert from 3D velocities when only observing one velocity component. Replacing $v_{esc}^2(r)$ with the line-of-sight measurement and the anisotropy correction $g(\beta(r)$, we lump the non-measurable terms into a filling factor $\mathcal{F}(r)$. Equation 1.14 can now be written as,

$$GM(<R) = \int_0^R \mathcal{F}_\beta(r)v_{esc}^2(r)dr, \tag{1.17}$$

where R is the radius within which the cumulative mass is estimated, and the filling

factor,

$$\mathcal{F}_\beta(r) = -2Gr^2 g(\beta(r)) \frac{\rho(r)}{\Phi(r)} \tag{1.18}$$

The value of $\mathcal{F}_\beta(r)$ must therefore be approximated and cannot be directly measured in observations. Diaferio (1999) first noticed that the average value of $\mathcal{F}_\beta(r)$ outside the cluster core is approximately constant and estimated a value of $\mathcal{F}_\beta = 0.5$ looking at dark matter subhalo populations in simulations. Later, Serra et al. (2011) found a value of $\mathcal{F}_\beta = 0.7$ by randomly sampling dark matter particles from simulations. Svensmark et al. (2015) stack similar mass systems in simulations and find a value in-between the two previous values of $\mathcal{F}_\beta = 0.59 - 0.63$. This discrepancy begs further study which I address in Chapters II, III, IV, and V of this thesis.

1.3.2 Theory of Density-Potential Pairs

Consider a mass distribution described by a spherical profile such that the mass density ρ and the potential Φ radial profiles are related by the Poisson equation and

$$\Phi(r) = -4\pi \mathrm{G} \Big[\frac{1}{r} \int_0^r \rho(r') r'^2 dr' + \int_r^\infty \rho(r') r' dr' \Big]. \tag{1.19}$$

Equation 1.19 allows one to analytically calculate the potential profile Φ for spherical density models in a static universe and for isolated systems.

There exist analytic formulae which have been shown to fit the density profiles of halos in N-body simulations. Here we present the following three: the NFW profile, the Gamma profile (Dehnen, 1993), and the Einasto profile (Einasto, 1969; Retana-Montenegro et al., 2012). Using equation 1.19, we have:

$$\rho(r) = \frac{\rho_0}{(r/r_0)(1+r/r_0)^2} \tag{1.20a}$$

$$\Phi(r) = -\frac{4\pi \mathrm{G}\rho_0 (r_0)^2 \ln(1+r/r_0)}{r/r_0} \tag{1.20b}$$

$$\rho(r) = \frac{(3-n)\mathrm{M}}{4\pi}\frac{r_0}{r^n}(r+r_0)^{4-n} \tag{1.21a}$$

$$\Phi(r) = \frac{\mathrm{GM}}{r_0}\frac{-1}{2-n}\Big[1-\Big(\frac{r}{r+r_0}\Big)^{2-n}\Big], n \neq 2 \tag{1.21b}$$

$$= \frac{\mathrm{GM}}{r_0}\ln\frac{r}{r+r_0}, n = 2$$

$$\rho(r) = \rho_0 \mathrm{exp}\Big[-\Big(\frac{\mathrm{r}}{\mathrm{r_0}}\Big)^{1/\mathrm{n}}\Big] \tag{1.22a}$$

$$\Phi(r) = \frac{-\mathrm{GM}}{r}\Big[1 - \frac{\Gamma\big(3n, \frac{r}{r_0}^{(1/n)}\big)}{\Gamma(3n)} + \frac{r}{r_0}\frac{\Gamma\big(2n, \frac{r}{r_0}^{(1/n)}\big)}{\Gamma(3n)}\Big] \tag{1.22b}$$

where ρ_0 or M is the normalization, r_0 is the scale radius, and n is the index. Equations 1.20, 1.21 and 1.22 are examples of density - potential *pairs* which share the same values for the shape parameters in the radial profiles of both the density and the potential. In other words, given a fit to the spherical density profile, one can infer the shape of the gravitational potential through these equations.

In Figure 1.1 we show an example halo with $\mathrm{M_{200}} = 6.3 \times 10^{14} \mathrm{M_\odot}$ and $\mathrm{r_{200}} = 1.34$ Mpc from the Millennium Simulation (Springel et al., 2005). The upper panel shows the spherically averaged density profile and the three model fits from Equations 1.20a, 1.21a, and 1.22a. The models are fit over the range $0.0 \leq r/r_{200} \leq 1$. While the models are nearly identical within r_{200}, they differ significantly in the outskirts.

The lower panel shows the radius/velocity phase space of the particles within this

halo. We use the radial components of the velocities of each particle and include the Hubble flow in the velocities. Notice that the particle edge contains a fair amount of localized structure due to infall. This cluster is dynamically active. The lines in the lower panel of Figure 1.1 show the predicted escape velocity edge for the three models using the Poisson equation and the fits to the density profiles and using Equations 1.20b, 1.21b and 1.22b. We consider each of the three models separately and infer model parameters by minimizing the χ^2 difference to the density profiles. All three models encompass the particles in the phase space.

1.3.3 Measuring the Caustic Profile in Observations

Before we can identify the projected $v_{los,esc}(r)$ surface, we must remove potential interloper galaxies from the phase-space. There are a host of methods to identify and remove interloper galaxies from the projected field-of-view around a galaxy cluster. These include color-based (Miller et al., 2005), σ-clipping, gapper (Fadda et al., 1996), and phase-space selection methods (Serra & Diaferio, 2013). In the work presented in this thesis, we use the shifting-gapper technique where velocity gaps are identified as a function of projected distance from cluster center. In the shifting-gapper technique, galaxies are sorted into bins as a function of radius while keeping the number in each bin constant at $N_{bin} = 25$. When odd multiples of 25 are used, the last radial bin may have less than 25 galaxies. In each bin, the galaxies are sorted by their peculiar velocity and an "f-pseudosigma" (Beers et al., 1990) is calculated and used as the velocity gap to remove perceived interlopers. This parameter is approximately the velocity dispersion of the galaxies in each radial bin when the distribution is close to normal, and is calculated as the difference between the upper and lower quartiles in velocity normalized by a constant. The process of removing interlopers is iterative. For each bin, the velocity difference between the sorted galaxies is calculated and if a gap exists equal-to or greater-than the f-pseudosigma between two galaxies, all

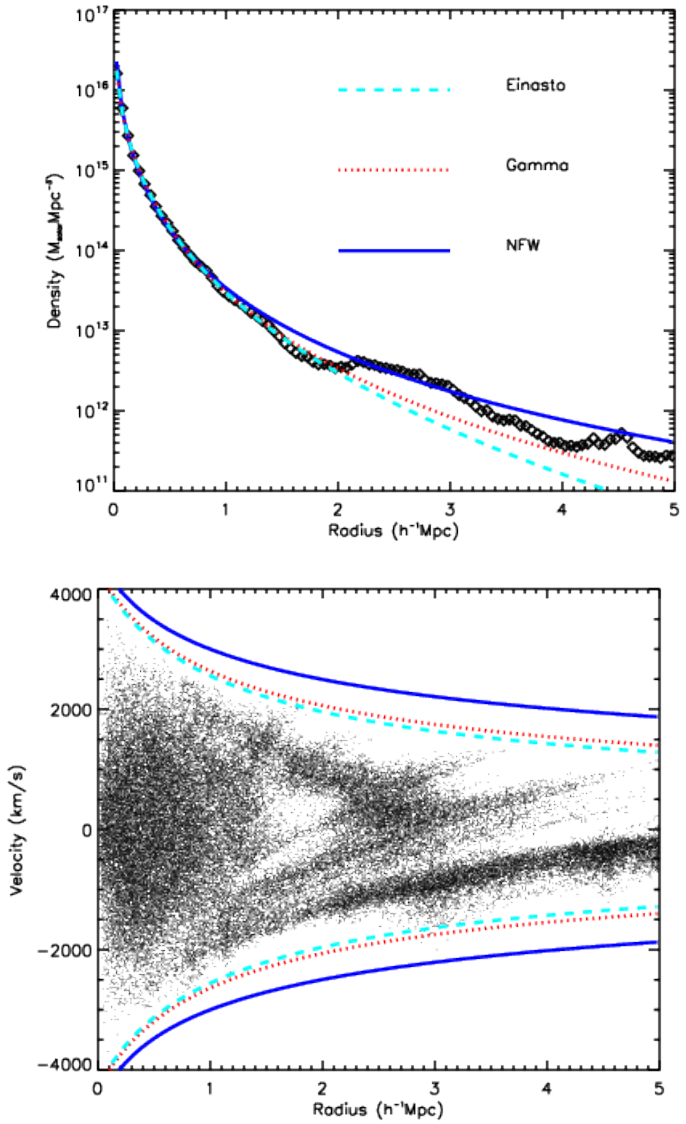

Figure 1.1: **Upper**: The spherically averaged density profile of a halo from the Millennium Simulation. The three lines are fits to the density profile over the range $0 \leq r_{200} \leq 1$ using Equations 1.20a,1.21a,and 1.22a. **Lower**: The radius-velocity phase-space of the particles. These are the radial components of the particle velocities and include the Hubble flow. The lines are the predicted escape velocity profile from the Poisson equation and fits to the density profiles (Equations 1.20b, 1.21b, and 1.22b).

galaxies above (for positive velocities) or below (for negative velocities) the gap are removed from the sample. This process is repeated for each bin and we stop if convergence is reached, less than 5 galaxies remain in a bin, or if f-pseudosigma < 500 km/s. The final galaxy sample can then be used to estimate the projected phase-space density.

In observed data, we identify the projected $v_{los,esc}(r)$ surface by applying standard kernel density estimation techniques to the dynamical tracers in the $r - v$ phase-space. We must keep in mind that the observed tracers have inherent observational uncertainties in both the radial and velocity directions. For low-redshift SDSS-like observations, the spectroscopic precision is ~ 50km s^{-1} or $0.5h^{-1}$Mpc in normalized coordinates and astrometric precision of $0.05h^{-1}$Mpc. Therefore, our kernel must be non-symmetric to account for the factor of ten difference in the two dimensions of the phase-space. Geller et al. (1999) showed that such axis weighting does not have a large effect on the mass profile determination. We use a fixed multi-dimensional gaussian kernel with a width ($h_{r,v}$) in the r and v directions that adapt to the sampling according to (Silverman 1998)

$$\mathrm{K}(x_r, x_v) = \frac{1}{2\pi h_r h_v} e^{-\frac{x_r^2 + x_v^2}{2h_{r,v}^2}} \tag{1.23}$$

$$h_{r,v} = \left(\frac{4}{3N}\right)^{1/5} \sigma_{r,v} \tag{1.24}$$

where N is the number of dynamical tracers in the total phase-space and $\sigma_{r,v}$ is the dispersion in the radial and velocity dimensions. Equation 1.23 minimizes the mean integrated squared error of the density estimate, which is the sum of the square of the statistical bias and the variance, also known as the statistical risk (Stien, 1981; Miller et al., 2002)). While Diaferio (1999) adopt an adaptive kernel technique, we will show in Chapters II and III that a standard fixed kernel recovers the cluster mass estimates with low scatter and bias.

Diaferio (1999) assert that any realistic models of galaxy clusters exhibit escape velocity profiles that at no point exceed $\frac{d\ln v_{esc}}{d\ln r} = \zeta$ where $\zeta = 1/4$. If an iso-density contour breaks this limit along its surface, the $v_{esc}(r)$ value is replaced with a new value that yields $\frac{d\ln v_{esc}}{d\ln r} = \zeta$. Serra et al. (2011) invoke a looser constraint of $\zeta = 2$ rather than $\zeta = 1/4$. This allows the algorithm to remove very drastic changes in $v_{los,esc}$, but does not overly restrict the iso-density contour values.

Once the iso-density contours are determined we must choose which surface corresponds to the escape velocity. We follow the standard procedure of assuming that the data are for time-averaged, self-gravitating, isolated clusters in a steady state. The density-weighted average escape velocity inside radius R is:

$$\langle v^2_{esc}(< R)\rangle = \frac{\int_0^R d^3\mathbf{x}\rho(\mathbf{x})v^2_{esc}(\mathbf{x})}{\int_0^R d^3\mathbf{x}\rho(\mathbf{x})} = -2\frac{\int_0^R d^3\mathbf{x}\rho(\mathbf{x})\Phi(\mathbf{x})}{M(< R)} \tag{1.25}$$

where we have used equation 1.11. The integral in the numerator on the right-hand side of equation 1.25 is twice the total potential energy of the system or $2W$ (Binney & Tremaine, 1987), which leads to:

$$\langle v^2_{esc}\rangle = -\frac{4W(< R)}{M(< R)} \tag{1.26}$$

where W and M are the total potential energy and mass of the system within the radius R. As described in Binney & Tremaine (1987), virialization means that the average system kinetic energy is half of the average system potential energy (KE = αPE and $\alpha = 0.5$) within the virial radius r_{vir}. In combination with Equation 2.1 this leads to

$$\langle v^2_{esc}(r < r_{vir})\rangle - 4\langle v^2(r < r_{vir})\rangle = 0 \tag{1.27}$$

In Chapter III, we test this virialization condition for clusters in the Millennium Simulation to understand at what radii this condition holds.

1.3.4 Applications of the Caustic Technique

The caustic technique has now been applied in a variety of surveys and simulations to recover point mass estimates (e.g. M_{200}) or mass profiles extending to $2-3r_{200}$ to great success. Observationally, Biviano & Girardi (2003) used the caustic technique to estimate mass profiles out to $2r_{200}$ in 43 non-interacting clusters which they found agreed closely with more traditional Jeans analysis when extrapolating outside the virial radius. Caustic mass profiles have also been used to constrain mass-to-light ratios in clusters (Rines et al., 2004) as well as velocity anisotropy profiles (Lemze et al., 2009). Radially, the caustic and weak lensing techniques remain the only two methods capable of estimating mass profiles beyond the central virialized region where equilibrium and virial assumptions must be applied. Diaferio et al. (2005) found close agreement between caustic and weak lensing mass profiles out to $2h^{-1}$ Mpc in 3 clusters. In most of these cases, the clusters were well sampled systems with > 50 galaxies/cluster and sometimes several hundred galaxies in the phase space.

Most of the theoretical work behind the caustic technique has been related to accuracy of the technique in very idealized situations. Despite the many successes in utilizing the caustic technique on well sampled galaxy clusters in the nearby universe, very little has been done to better understand the systematic and statistical limitations of the caustic technique with observational constraints. Initial tests performed in Diaferio (1999) and follow-up work in Serra et al. (2011) sample dark matter subhalos or particles directly to use as position-velocity tracers when testing the technique. In this scenario, they show unbiased mass profiles to within the errors from $r_{200} - 3r_{200}$. The caustic technique makes the assumption that galaxy clusters are spherically symmetric, and therefore triaxial systems and their orientation along the observer's line-of-sight may influence the mass estimate. Svensmark et al. (2015) confirmed this fact and showed that the difference between caustic masses measured along the major axis can be 70% higher than if measured along the minor axis. All

these studies relied on well sampled clusters and sampled from their dark matter density and velocity distributions. Now, with the advent of large cosmological simulations (Springel et al., 2005) and complex semi-analytic prescriptions for Halo Occupation Distributions (De Lucia & Blaizot, 2007; Guo et al., 2011), there is an opportunity to further study the caustic technique within the framework of observational limits.

1.4 Testing the Caustic Technique with Semi-Analytic Catalogs

Throughout much of this thesis, we make use of the Millennium Simulation (Springel et al., 2005) to improve upon and test for statistical and systematic biases present in the caustic technique. The cosmological volume in the simulation provides us with a large number of systems to perform our analyses across a large range in halo mass. In addition to numbers, several semi-analytic galaxy catalogs (Bower et al., 2006; Bertone et al., 2007; De Lucia & Blaizot, 2007; Guo et al., 2011) along with an all-sky light cone have been constructed for the Millennium Simulation which creates the opportunity to study the caustic technique with observational limitations.

Bower et al. (2006) suggest that in its most basic form, a theory of galaxy formation is a set of rules motivated by physical processes which transforms a halo mass function into an observed galaxy luminosity function. In fact, most semi-analytic techniques (which define the rule-set) judge their success primarily by comparing to published galaxy luminosity functions. In this work, we are equally concerned with how well those galaxies trace the underlying radial velocity phase-space, which we use to measure the escape velocity of halos and their gravitational potentials.

Galaxies in the semi-analytic algorithms are first identified at the location of collapsed sub-structure within halos. These are nominally the sub-halos and algorithms

like SUBFIND (Springel et al., 2001) which have been shown to work well to identify all of the sub-structure in N-body simulations (see also Knebe et al. (2011)). Once identified, these sub-halos trace the positions and velocities of the galaxy population. Rules are put in place to define when and how a burst of activity (e.g. star-formation/nuclear) occurs. These sub-halos can grow in total mass (and luminosity) by accreting gas (or a model for gas), other particles, and other sub-halos through merging. It is the merging and other dynamical interactions which are responsible for altering the radial velocity phase-space and thus affecting our ability to use dynamical tracers for the halo mass.

At any given redshift (or snapshot output of an N-body simulation), the sub-halos which have survived a merger up to that point would not be good tracers of the halo radial velocity phase-space (see also Figure 2.3). This is because at the resolution of the Millennium Simulation, the sub-halos in simulations are easier to destroy compared to galaxies in the real Universe, which are much more compact and gravitationally bound. So while an interaction might destroy a sub-halo, there is no reason to think it would destroy a galaxy. In modern semi-analytic techniques, decisions (or a rule set) must be defined to decide what to do with a "galaxy" after its sub-halo is no longer identified in a snapshot. The most common approach is to identify the most-bound particle in the sub-halo before it was destroyed and follow it as a surviving galaxy through future snapshots (i.e., to lower redshifts). These are sometimes called "orphans" as they are semi-analytic galaxies that have lost their dark matter halos.

The above rule does not happen in reality: the evolution of the position and velocity of a galaxy cannot be determined from a single particle. So a technique is applied to define statistically how long a galaxy might survive before it is ripped apart

in a merger (i.e., the merging time due to dynamical friction):

$$t_{merger} = \alpha_{fric} \frac{V_{circ} r_{SH}^2}{G M_{SH} \ln\left(1 + \frac{M_{halo}}{m_{SH}}\right)} \tag{1.28}$$

where V_{circ} is the circular velocity for a mass in a gravitational potential defined by an isothermal sphere at radius r_{SH} of the sub-halo and the masses of the halo and the sub-halo are M_{halo} and M_{SH} respectively (Binney & Tremaine, 1987), and α_{fric} is a coefcient to be needed to reproduce observed luminosity functions at the luminous end (Guo et al., 2011). In this rule-set, a clock is started when a galaxy's sub-halo is destroyed. The surviving galaxy is merged with its nearest galaxy or sub-halo after this time-scale has expired. When the final merging happens, the galaxy is destroyed and its stars, gas, and dark matter are distributed in various ways (i.e., it is a rule-set in the semi-analytic algorithm). However, this statistical rule-set only defines *when* a dark matter orphaned galaxy is destroyed, not how. For instance, the particle which represents the galaxy is no longer actually merging or changing its orbit due to dynamical interactions outside the normal particle-particle interactions. This would require a new rule-set.

The above description is complicated and there are numerous ways in which a semi-analytic techniques can implement dynamical events in the lifetime of a simulated galaxy. This is why we investigate the effects on the caustic masses from different implementations of halo dynamics in the semi-analytic galaxy catalogs.

1.5 This Work

In this work, we study, improve upon, and use the caustic technique to estimate masses and constrain cosmology. The caustic technique is the ideal candidate for this work for several reasons. First, the C4 cluster sample (Miller et al., 2005) contains many clusters with sufficient sampling for the caustic technique to estimate accurate

masses. As I show in Chapter II, the caustic mass estimator is less biased and has less mass scatter than velocity dispersion virial scaling relations (Evrard et al., 2008). As weak lensing and X-ray samples continue to grow, the caustic technique is a viable way to not only estimate cluster masses, but perform other astrophysical studies relating to galaxy cluster potential with a large number of systems currently and into the future. In the years to come, large photometric and spectroscopic surveys such as DESI (Levi et al., 2013) will enable caustic mass estimates of clusters to deeper redshifts further enabling cosmological studies. Building a deeper understanding of the limitations of the caustic technique will influence future studies, especially at the University of Michigan where observers have access to high quality spectroscopic instrumentation on the MDM and Magellan observatories (Bigelow & Dressler, 2003; Martini et al., 2011; Mateo et al., 2012).

This thesis addresses the current lack of systematic study behind the caustic technique with an eye toward observational considerations. Based on this statistical analysis, we apply the technique to a large, low redshift cluster survey and constrain cosmological parameters through the use of the cluster mass function. In Chapter II, I probe the primary systematics the caustic technique faces if halos are correctly identified. There I look into how line-of-sight, sampling, magnitude, color, and incompleteness bias or scatter caustic estimates to understand how observational targeting practices might affect our results. In Chapter III, I measure the theoretical limits for the caustic mass estimation technique. The technique is based on the assumptions that the caustic traces the projected escape velocity profile and that we can correctly identify and measure the caustic profile in projection. Once individual cluster masses are estimated, I discuss in Chapter IV a new caustic identification technique in stacked phase-spaces that can be used to self-calibrate masses in a sample of clusters. Finally, in Chapter V I fold all this knowledge together to estimate caustic masses for the C4 cluster sample in order to constrain cosmological parameters.

CHAPTER II

Identifying Systematic Uncertainties in Estimated Cluster Masses

2.1 Introduction

Upcoming galaxy cluster surveys from the millimeter to the X-ray wavelengths have the potential to identify thousands to hundreds of thousands of groups and clusters (Song et al., 2012; Pillepich et al., 2012). These large cluster samples will be used to constrain the cosmological parameters which govern the growth of structure in our Universe (Miller et al., 2001; Miller & Batuski, 2001; Rozo et al., 2009; Vikhlinin et al., 2009; Benson et al., 2013). Regardless of the luminous tracer used to infer the underlying dark matter distribution (e.g., normal galaxies, emission-line galaxies, luminous red galaxies, quasi-stellar objects, galaxy clusters), our ability to constrain the cosmological parameters depends on the accuracy and precision of the mass.

Unlike most galaxies, the masses of galaxy clusters can be directly inferred via the observational signature of the gravitational potential (or its derivative). In fact, clusters are the only object for which current technology enable three physically independent mass estimation techniques: via the dynamics of the member galaxies, via the hot gas in the intra-cluster medium, and via gravitational lensing. These three techniques provide a vital cross-check on the mass estimation techniques, assuming

one can quantify the statistical precision and accuracy of the cluster mass estimates themselves.

Cosmological N-body and hydrodynamic simulations play a new and important role in characterizing the statistical and systematic uncertainties on cluster mass estimates (Nagai et al., 2007; Becker & Kravtsov, 2011). There has been excellent recent progress on the important step of utilizing realistic mock astronomical observations based on ideal simulations (Meneghetti et al., 2010a; Rasia et al., 2012; Saro et al., 2013). Our primary goal is to utilize a diverse suite of semi-analytic galaxy catalogs to study how well a realistic spectroscopic program can constrain the dynamical masses of galaxy clusters in the low redshift Universe. We quantify our results based on the scatter and bias of the "observed" dynamical mass when compared to the halo masses M_{200}, which refers to the mass within a radius of r_{200}.

When inferring the dynamical masses of clusters, we require an accurate measurement of the galaxy peculiar velocities. With their total dispersion, their dispersion profiles, and/or their escape velocity profile, we can infer cluster masses based on the virial theorem, the Jeans relation for a collision-less fluid, or the caustic technique. To first order, galaxies dynamically respond to the influence of the Newtonian gravitational potential, regardless of their luminosities, shapes, colors, or star-formation histories. Yet galaxies traveling within a cluster environment are likely to have had one or more localized and short-lived gravitational interaction over its lifetime. This "dynamical friction" alters the total cluster velocity distribution away from its simple Newtonian expectations, an effect that needs to be captured by the semi-analytic galaxies. In this work, we use sub-halo catalogs as well as a suite of semi-analytic mock galaxy catalogs, to explore how sensitive dynamical masses are to different prescriptions of this dynamical friction.

Given the above context and the state of both cosmological simulations and semi-analytic galaxy formation, the question as to whether these mock galaxies capture

the true velocity distribution of real galaxies in clusters is still unanswered. However, the current simulated data now contain a wide variety of options for how galaxies are pasted into the clusters. More-so, these semi-analytic techniques create mock galaxy clusters which very closely resemble the observed Universe in many respects (Guo et al., 2011). While the semi-analytic galaxy catalogs are not fully simulated Universes, they do provide us with an opportunity to assess how well our theories and algorithms could do under realistic observational conditions (e.g., non-ideal target selection).

In this study, we focus on how different tracers in the N-body simulations (e.g. sub-halos or semi-analytic galaxies) allow us to observe the gravitational potential and measure the projected escape velocity to infer the cluster mass. This technique is analogous to applying the Jeans equation, except that the cluster observable is the radial escape velocity as opposed to the velocity dispersion and that the escape velocity maps directly to the gravitational potential, whereas the Jeans analysis maps to its derivative. These differences are subtle but important. Regardless, both the Jean's technique and the caustic technique posit that the radius/velocity *phase-space* does indeed map directly to the gravitational potential and through some simplifying assumptions, ultimately to the gravitational mass.

Our primary goal is to present the statistical characterization (accuracy and precision) of caustic inferred halos masses, as well as study the effects of survey strategy when planning spectroscopic follow-up. In Section 2 we discuss the caustic technique in detail and apply this technique in Section 3 on N-body simulations using the underlying particles, the sub-halos, as well as on the semi-analytic mock galaxy catalogs. Using the galaxy catalogs, we incorporate realistic targeting scenarios and show the effects on the measured bias and scatter.

2.2 Methods and Data

2.2.1 Inferring Halo Mass from Gravitational Potential

Under Newtonian dynamics, the escape velocity is related to the gravitational potential of the system,

$$v_{esc}^2(r) = -2\Phi(r). \tag{2.1}$$

If the dynamics of the system are controlled by the gravitational potential, tracers which have not escaped the potential well should exist in a well-defined region of $r - v$ phase space, where r is the physical or projected radius from the center of the cluster and v is the peculiar 3-dimensional velocity or projected 1-dimensional velocity respectively relative to the bulk cluster motion. The edge of this region in $r-v$ space within which bound tracers are allowed to exist defines the escape velocity, $v_{esc}(r)$.

In Figure 1, we show an example halo from the Millennium Simulation where we identify the actual gravitational potential of the dark matter $G\Sigma_i \frac{m}{|x-x_i|}$ (red lines) and the iso-density contour which traces the escape velocity profile of the halo (blue lines). In the left panel, the velocities and radii are 3-dimensional and in spherical coordinates while in the right panel they are projected along one line-of-sight. The surface that defines the density edge in the $r-v$ phase space is an iso-density contour that follows $v_{esc}(r)$ and therefore $\Phi(r)$.

In observed data, we identify the projected $v_{esc}(r)$ surface by applying standard kernel density estimation techniques to the dynamical tracers in the $r-v$ phase-space. The observed tracers have inherent observational uncertainties in both the radial and velocity directions. In this work, we focus on low-redshift SDSS-like observations with spectroscopic precision of $\sim$ 50km s^{-1} or $0.5h^{-1}$Mpc in normalized coordinates and astrometric precision of $0.05h^{-1}$Mpc. Therefore, our kernel must be non-symmetric to account for the factor of ten difference in the two dimensions of the phase-space.

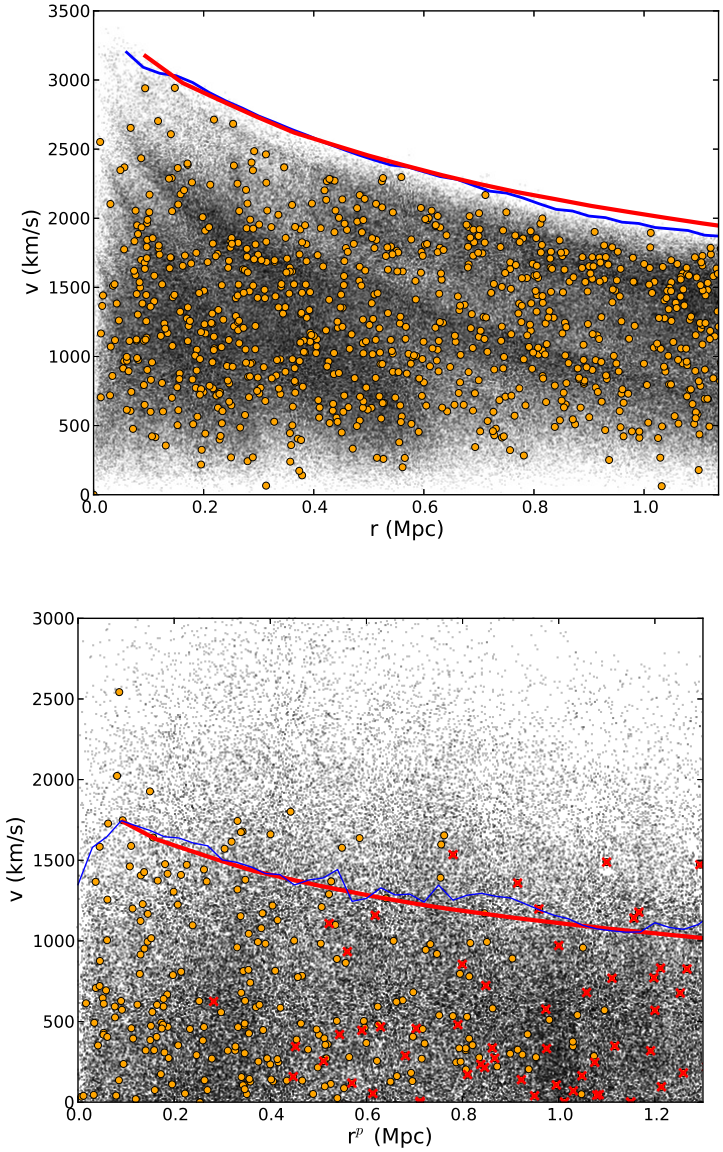

Figure 2.1: **Top**: The gravitational potential (red band) is shown to envelope the edge of the particle (black points) and galaxy (orange circles) data when projected in the 3D radius-redshift space. The edge of the phase-space density can be defined by choosing the correct iso-density contour (blue). **Bottom**: The same halo projected on the sky, which blurs the surface from both the positions and anisotropies in the velocity components. Galaxies that are projected into the space, but live outside the virial radius in 3-dimensions are highlighted with red x's.

Geller et al. (1999) showed that such axis weighting does not have a large effect on the mass profile determination, something that we confirm in this work. We use a fixed multi-dimensional gaussian kernel with a width in the r and v directions that independently adapt to the sampling according to (Silverman 1998)

$$\mathrm{K(r,v)} = \left(\frac{4}{3\mathrm{N}}\right)^{1/5} \sigma_{\mathrm{r,v}} \tag{2.2}$$

where N is the number of dynamical tracers in the total phase-space and $\sigma_{r,v}$ is the dispersion in the radial and velocity dimensions. Equation 2.2 minimizes the mean integrated squared error of the density estimate, which is the sum of the square of the statistical bias and the variance, also known as the statistical risk (Stien, 1981; Miller et al., 2002). While Diaferio (1999) adopt an adaptive kernel technique, we will show that a standard fixed kernel recovers the cluster mass estimates with low scatter and bias.

Diaferio (1999) assert that any realistic models of galaxy clusters exhibit escape velocity profiles that at no point exceed $\frac{d\ln v_{esc}}{d\ln r} = \zeta$ where $\zeta = 1/4$. If an iso-density contour breaks this limit along its surface, the $v_{esc}(r)$ value is replaced with a new value that yields $\frac{d\ln v_{esc}}{d\ln r} = \zeta$. Here, we follow the prescription used in Serra et al. (2011) which invoke a looser constraint of $\zeta = 2$ rather than $\zeta = 1/4$. This allows the algorithm to remove very drastic changes in v_{esc}, but does not overly restrict the iso-density contour values.

Once the iso-density contours are determined we must choose which surface corresponds to the escape velocity. However, here we follow the standard procedure of assuming that the data are for time-averaged, self-gravitating, isolated clusters in a steady state. As described in Binney & Tremaine (1987), virialization means that the average system kinetic energy is half of the average system potential energy (KE $= \alpha$PE and $\alpha = 0.5$) within the virial radius r_{vir}. In combination with Equation 2.1

this leads to

$$\langle v^2_{esc}(r < r_{vir})\rangle - 4\langle v^2(r < r_{vir})\rangle = 0 \tag{2.3}$$

Equation 2.3 is defined for three dimensional measurements of the velocities. In Chapter III we test this virialization condition in the Millennium Simulation and find it to hold when the system average energies are calculated near the virial radius.

In real data we only observe the projected line-of-sight component of both the velocity dispersion and the escape velocity. There could exist some level of anisotropy in the velocity vectors: for example the radial and non-radial components of the velocity are not equal: $\langle v_\theta\rangle = \langle v_\phi\rangle \neq \langle v_r\rangle$. This is parameterized by the anisotropy parameter $\beta(r) = 1 - \frac{\langle v^2_\theta\rangle(r)}{\langle v^2_r\rangle(r)}$. By assuming that the escape velocity profile we measure in projection $v^2_{esc,los}(r_\perp) = v_{esc,\theta}(r_\perp)$, where $r_\perp$ is where the 3-dimensional radius r equals the projected radius r^p, Diaferio (1999) show that

$$\langle v^2_{esc,los}\rangle(r_\perp) = \frac{(1-\beta(r_\perp))}{(3-2\beta(r_\perp))}\langle v^2_{esc}(r_\perp)\rangle \approx g(\beta(r))\langle v^2_{esc}(r)\rangle \tag{2.4}$$

and as in Diaferio (1999), we define the projection correction term:

$$g(\beta(r)) = \frac{3-2\beta(r)}{1-\beta(r)}. \tag{2.5}$$

Recalling that equation 2.3 is for the three-dimensional velocities, it can be re-written in terms of the observed projected quantities (i.e., the projected radii r^p and the line-of-sight velocities of the galaxies):

$$\langle\langle v^2_{los,esc}\rangle(r^p < r^p_{vir})\rangle - 4\langle v^2_{los}(r^p < r^p_{vir})\rangle = 0 \tag{2.6}$$

We calculate the velocity dispersion $\sqrt{\langle v^2_{los}\rangle}$ (hereafter labeled σ^v) using a robust median-weighted technique on galaxies within the projected radius that has $\frac{\delta\rho}{\rho_{crit}} = 200$ (i.e., r_{200}), which is $\langle v^2\rangle_{r_{200}}$. Interlopers are removed via a shifting-gapper

technique described in §2.2.4.

We then choose the iso-density contour that satisfies equation 2.6. There is some uncertainty in the determination of this surface, which we quantify in §2.3.2. We note that we always use the same tracers when calculating the dispersions and the phase-space density

Ideally, we could use the escape velocity profile, which we assume to be the potential profile through equation 2.1, to estimate a mass by using the Poisson equation $\nabla^2\Phi(x) = 4\pi G\rho(x)$ or some variation to arrive at the mass profile. However, this ideal scenario involves the challenge of taking derivatives of a noisy estimate of $\Phi(r)$. Instead, Diaferio & Geller (1997) introduce an alternative estimation through the partial mass differential equation $dm = 4\pi\rho(r)r^2dr$. Invoking equation 2.1, we may rewrite this differential as:

$$dm = -2\pi v_{esc}^2(r)\frac{\rho(r)r^2}{\Phi(r)}dr \tag{2.7}$$

and integrate to arrive at:

$$GM(< R) = \int_0^R -2G\pi v_{esc}^2(r)\frac{\rho(r)r^2}{\Phi(r)}dr \tag{2.8}$$

After identifying the iso-density contour that describes the projected $\langle v_{esc,los}\rangle(r)$, we now have an estimate for $\Phi(r)$ by using equation 2.1 and $g(\beta(r))$ and our equation now becomes:

$$GM(< R) = \int_0^R -2G\pi g(\beta(r))\langle v_{los,esc}^2\rangle(r)\frac{\rho(r)r^2}{\Phi(r)}dr \tag{2.9}$$

$$GM(< R) = \int_0^R \mathcal{F}_\beta(r)\langle v_{los,esc}^2\rangle(r)dr \tag{2.10}$$

where

$$\mathcal{F}_\beta(r) = -2G\pi g(\beta(r))\frac{\rho(r)r^2}{\Phi(r)} \tag{2.11}$$

Diaferio (1999) claim that $\mathcal{F}_\beta(r)$ is roughly constant as a function of radius from 1-$3r_{200}$ as calibrated against simulations. For instance, Diaferio (1999) find $\langle\mathcal{F}_\beta(r)\rangle = 0.5$ and Serra et al. (2011) find $\langle\mathcal{F}_\beta(r)\rangle = 0.7$. We use a constant value calibrated against the Millennium Simulations to be $\mathcal{F}_\beta = 0.65$ and discuss the implications of both the assumption of a constant as well as its calibration in Section 2.4. For a variation of the caustic technique that does not require this calibration, see Chapter III.

2.2.2 Inferring Halo Masses from the Virial Relation

Evrard et al. (2008) show that the velocity dispersion of a dark matter halo obeys a very tight virial relationship when compared with the critical dark matter mass M_{200} of the form:

$$M_{200} = 10^{15}h(z)^{-1}\left(\frac{\sigma_{DM}(M_{200}, z)}{\sigma_{DM,15}}\right)^{\alpha} \tag{2.12}$$

where σ_{DM} is the 1D velocity dispersion of the dark matter, or more precisely the 3D velocity dispersion divided by the $\sqrt{3}$. For the Millennium Simulation, we use the normalization $\sigma_{DM,15} = 1093.0$ km/s and slope $\alpha = 2.94$. Evrard et al. (2008) find these to be consistent between different cosmological simulations.

The scatter in $\sigma_{1D,DM}$ at fixed M_{200} from the N-body simulations for equation 2.12 is $\sim 5\%$. With slope α, this inherent scatter implies a mass scatter from the virial relation to be $\sim 15\%$. However, this amount of scatter only applies when the 3D velocity dispersion is known, which is never the case in the observed Universe. Saro et al. (2013) show that the real scatter in mass as measured from the line-of-sight velocity dispersion is closer to $\sim 40\%$ when 100 red-sequence galaxies are used. This huge increase in scatter stems mostly from the projection of the galaxies and their

velocities along the line-of-sight.

Saro et al. (2013) use the De Lucia & Blaizot (2007) semi-analytic galaxy catalogs but they do not use the Evrard et al. (2008) calibration. Instead, they re-calibrate the slope and amplitude of equation 2.12 using the 3-dimensional information of the *galaxies* as opposed to the particles. Saro et al. (2013) also calibrate their measured scatter in velocity and mass against a specific set of 100 red-sequence galaxies within the 3D virial radius of each halo. In the former case, the slope and amplitude will differ from the dark matter if the galaxies are dynamically biased with respect to the dark matter. In the latter case, relationships for the scatter (e.g., as a function of the number of observed galaxies) become meaningless for larger samples (and it is quite common to have clusters with more than 100 observed galaxies in their $r - v$ phase space).

In this work, we use the virial-mass relationship from Evrard et al. (2008). This is an important distinction, because the different semi-analytic galaxy catalogs can each have inherent dynamical biases between the dark matter and the galaxies that we would otherwise not detect. Similarly, the scatter in the measured line-of-sight velocity dispersions is determined against the particle velocity dispersions. This is also important, in that the observed line-of-sight scatter in the velocity dispersions and masses can be compared between the different semi-analytic galaxy catalogs.

2.2.3 The Halos and the Semi-analytic Galaxy Catalogs

We select 100 halos from the Millennium Simulation to perform this study. While the halos are not chosen on the basis of any specific physical characteristics, our sample aims for fairly even mass sampling over $\sim 10^{14} - 10^{15} M_{\odot}$. The average mass $\langle M \rangle = 2.34 \times 10^{14} M_{\odot}$ and the average critical radius $\langle r_{200} \rangle = 0.95$Mpc. We then use four semi-analytic catalogs (Guo et al., 2011; De Lucia & Blaizot, 2007; Bertone et al., 2007; Bower et al., 2006) created using the Millennium Simulation along with

the identified subhalos within each halo to test the caustic technique in section 2.3.

Bower et al. (2006) suggest that in its most basic form, a theory of galaxy formation is a set of rules motivated by physical processes which transforms a halo mass function into an observed galaxy luminosity function. In fact, most semi-analytic techniques (which define the rule-set) judge their success primarily by comparing to published galaxy luminosity functions. In this work, we are equally concerned with how well those galaxies trace the underlying radial velocity phase-space, which we use to measure the escape velocity of halos and their gravitational potentials.

Galaxies in the semi-analytic algorithms are first identified at the location of collapsed sub-structure within halos. These are nominally the sub-halos and algorithms like SUBFIND (Springel et al., 2001) which have been shown to work well to identify all of the sub-structure in N-body simulations (see also Knebe et al., 2011). Once identified, these sub-halos trace the positions and velocities of the galaxy population. Rules are put in place to define when and how a burst of activity (e.g. star-formation/nuclear) occurs. These sub-halos can grow in total mass (and luminosity) by accreting gas (or a model for gas), other particles, and other sub-halos through merging. It is the merging and other dynamical interactions which are responsible for altering the radial velocity phase-space and thus affecting our ability to use dynamical tracers for the halo mass.

At any given redshift (or snapshot output of an N-body simulation), the sub-halos which have survived a merger up to that point would not be good tracers of the halo radial velocity phase-space (see also Figure 2.3). This is because at the resolution of the Millennium Simulation, the sub-halos in simulations are easier to destroy compared to galaxies in the real Universe, which are much more compact and gravitationally bound. So while an interaction might destroy a sub-halo, there is no reason to think it would destroy a galaxy. In modern semi-analytic techniques, decisions (or a rule set) must be defined to decide what to do with a "galaxy" after

its sub-halo is no longer identified in a snapshot. The most common approach is to identify the most-bound particle in the sub-halo before it was destroyed and follow it as a surviving galaxy through future snapshots (i.e., to lower redshifts). These are sometimes called "orphans" as they are semi-analytic galaxies that have lost their dark matter halos.

The above rule does not happen in reality: the evolution of the position and velocity of a galaxy cannot be determined from a single particle. So a technique is applied to define statistically how long a galaxy might survive before it is ripped apart in a merger (i.e., the merging time due to dynamical friction):

$$t_{merger} = \alpha_{fric} \frac{V_{circ} r_{SH}^2}{G M_{SH} \ln\left(1 + \frac{M_{halo}}{m_{SH}}\right)} \tag{2.13}$$

where V_{circ} is the circular velocity for a mass in a gravitational potential defined by an isothermal sphere at radius r_{SH} of the sub-halo and the masses of the halo and the sub-halo are M_{halo} and M_{SH} respectively (Binney & Tremaine, 1987), and α_{fric} is a coefficient needed to reproduce observed luminosity functions at the luminous end (Guo et al., 2011). In this rule-set, a clock is started when a galaxy's sub-halo is destroyed. The surviving galaxy is merged with its nearest galaxy or sub-halo after this time-scale has expired. When the final merging happens, the galaxy is destroyed and its stars, gas, and dark matter are distributed in various ways (i.e., it is a rule-set in the semi-analytic algorithm). However, this statistical rule-set only defines *when* a dark matter orphaned galaxy is destroyed, not how. For instance, the particle which represents the galaxy is no longer actually merging or changing its orbit due to dynamical interactions outside the normal particle-particle interactions. This would require a new rule-set.

The above description is complicated and there are numerous ways in which a semi-analytic techniques can implement dynamical events in the lifetime of a simulated

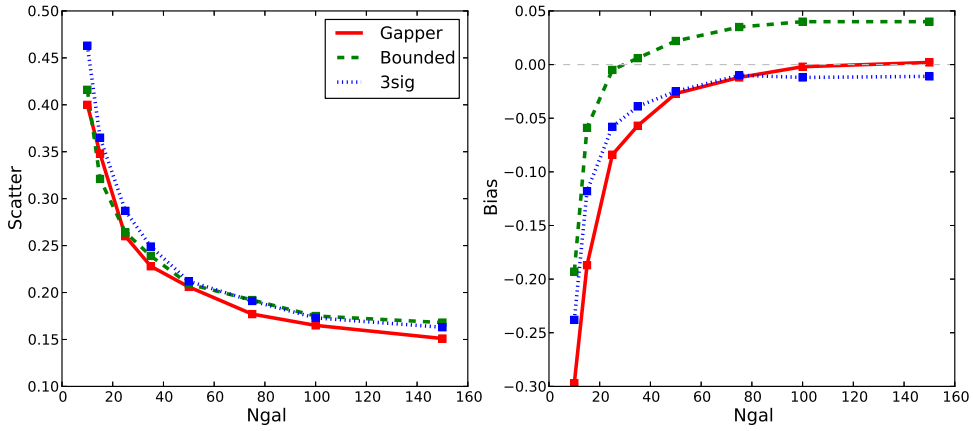

Figure 2.2: Log scatter (**Left**) and log bias (**Right**) in velocity dispersion as a function of N_{gal} with interloper removal via a bounded + gapper technique (solid-red), bounded (dashed-green), and bounded + 3σ (dotted-blue). The gapper technique both minimizes the bias and scatter of the 3 methods tested in this work for $N_{gal} > 50$.

galaxy. This is why we will investigate the effects on the caustic masses from different implementations of halo dynamics in the semi-analytic galaxy catalogs.

In this analysis we start with all of the semi-analytic galaxies within a $60h^{-1}$Mpc-length 3-dimensional box around each halo center. We then sub-select the N brightest galaxies (where N = 100, 50, 25, etc) within a projected radius in these volumes to create the halo radius/velocity phase-space diagrams along one or more lines-of-sight. These volumes place limits on the projected phase-space velocities that are $\pm$3000km/s relative to the halo velocity centroids. Since the typical escape velocities are $\sim$ 1500km/s, these volumes are large enough to incorporate realistic projection effects (see Figure 2.1). With projection, interlopers (non-member foreground/background galaxies) can play a large role in affect both the measured phase-space density as well as the line-of-sight velocity dispersion. Therefore, an effort must be made to systematically remove the interlopers from each line-of-sight projection.

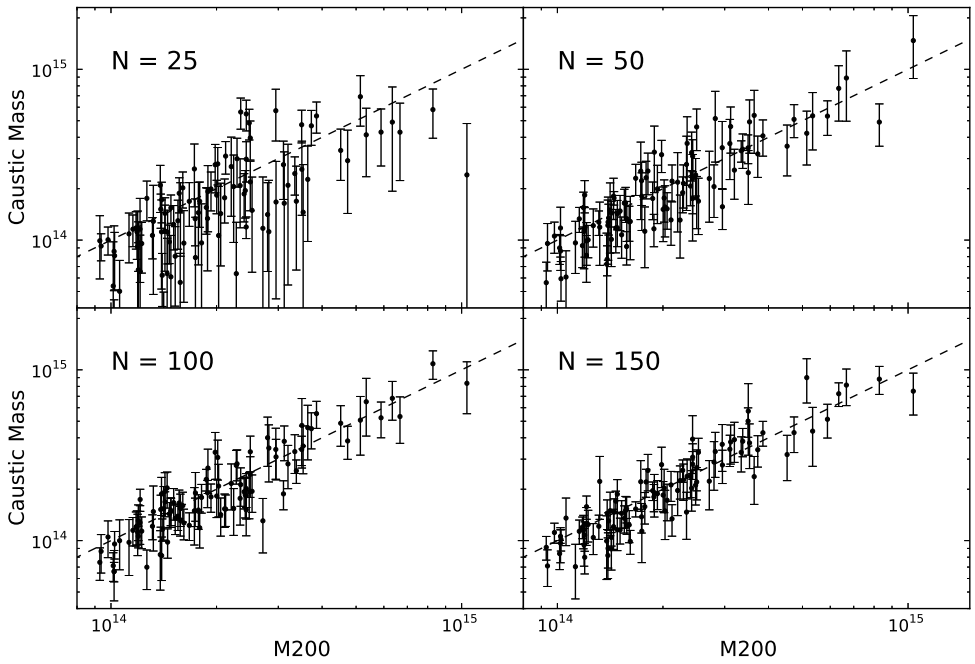

Figure 2.3: Inferred caustic mass for N_{gal} = 25,50,100, 150 in the Guo semi-analytic sample vs M_{200} for 100 halos in the Millennium Simulation. The error bars are the measured line-of-sight scatter added in quadrature with the intrinsic uncertainty in caustic mass described in §2.3.2. The dashed line is unity.

2.2.4 Interloper Identification and Removal

Many methods have been devised to identify and remove interloper galaxies from a sample around a halo. These include color-based (Miller et al., 2005), σ-clipping, gapper (Fadda et al., 1996), and phase-space selection methods (Serra & Diaferio, 2013). In this study, we do not try and optimize any particular method, but rather choose one in existence that returns a minimal bias for velocity dispersion and mass at large sampling. We limit ourselves by testing only a few basic interloper removal techniques, and compare their relative biases and resulting scatter.

In Figure 2.2 we compare three common techniques to measure velocity dispersions against the underlying dark matter. The first technique is to apply a simple upper/lower bound in velocity space ($\pm$3500 km/s). The second is to iteratively remove outliers via sigma clipping (3.5σ). The third is called a shifting-gapper, where we work in the full phase-space and identify velocity gaps as a function of radius as indicators of interloping sub-structure. This shifting-gapper technique is similar to what is applied in Wing & Blanton (2011). Galaxies are sorted into bins as a function of radius while keeping the number in each bin constant at $N_{bin} = 25$. When odd multiples of 25 are used, the last radial bin may have less than 25 galaxies. In each bin, the galaxies are sorted by their peculiar velocity and a "f-pseudosigma" (Beers et al., 1990) is calculated and used as the velocity gap to remove perceived interlopers. The calculation of f-pseudosigma is an iterative process that we stop if less than 5 galaxies remain in a bin or if f-pseudosigma < 500 km/s. In all cases, the final interloper-cleaned velocity dispersion is calculated using a robust bi-weighted estimator, which we confirm is always less biased than a simple standard deviation (Beers et al., 1990).

When applying only a simple velocity boundary, the dispersions are biased high and the scatter is large (for $N_{gal} > 25$). However, both the sigma clipping and the shifting-gapper techniques do better and equally well in recovering unbiased veloc-

ity dispersions (see also Saro et al., 2013). The shifting-gapper does a better job at reducing the scatter at all values of N_{gal}. This is because the technique utilizes the 2-dimensional phase-space data as opposed to the one-dimensional velocity distributions. As such, the shifting-gapper can identify sub-structure in the phase-space which sigma clipping cannot. Clusters with poor sampling $N_{gal} < 25$, have dispersions that are biased low. Throughout the rest of this work we apply the shifting-gapper technique to measure velocity dispersions.

2.3 Results

We measure the caustic mass M_c inside r_{200} and compare directly to the spherical halo mass M_{200}. In Figure 2.3 we show how M_c inferred from the N_{gal} brightest galaxies inside r_{200} scales with M_{200}. In each panel, we highlight the M_c inferred masses using the Guo semi-analytic galaxies (dots). The error bars are detailed in §2.3.1 & 2.3.2. We note that in this figure, M_c for each of the 100 halos is measured along a single $60h^{-1}$Mpc line-of-sight, thus representing a realistic observing scenario.

We measure the percent scatter in $\ln M_c$ at fixed $\ln M_{200}$ as well as the bias determined from the error weighted mean difference between $\ln M_c$ and $\ln M_{200}$. In order to compare to the virial masses, we also quantify the log scatter and bias of the projected line-of-sight velocity dispersion and the virial mass (equation 2.12). At small $N_{gal} = 25$, the caustic masses are biased low by $\sim 15\%$ on average, and the log-normal scatter about the fit to the data is $\sim 50\%$. At $N_{gal} > 50$, the bias disappears and the scatter reduces to $\sim 30\%$ at $N_{gal} = 150$. We show a summary of the caustic mass bias and scatter in Figures 2.5 and 2.7. These data are presented in Tables 2.1-2.5. At fixed N_{gal}, the biases of the different semi-analytics agree to within their errors and so unless otherwise noted, we focus the rest of our analyses on the Guo et al. (2011) galaxies.

2.3.1 The Observed Phase Space Density

Typical observations of galaxy clusters can detect or easily measure the spectroscopic redshifts of a handful to several hundred galaxies within the virial radius of a system. Fundamental to the caustic technique is the projection of observed galaxies into a radial and velocity phase space, within which we identify a critical iso-density transition or caustic. In §2.2, we describe how we use a multi-dimensional gaussian kernel to estimate the underlying phase space density based on an observed tracer population. Density estimates always carry some degree of uncertainty due to limited sampling. We therefore expect that small or sparsely observed clusters will exhibit a large amount of uncertainty in the density estimation process. We quantify this uncertainty and it's effect on the caustic mass estimate by using the jack-knife technique to re-sample the phase-space.

For each jack-knife re-sampling j of a cluster with N_{gal}, we re-calculate the velocity dispersion (σ_j^v) and re-calibrate the escape velocity iso-density contour according to equation 2.6 to infer a jack-knife caustic mass ($M_{c,j}$) according to equation 2.10. We show the distribution of $\ln(M_{c,j}/M_{200})$ for four randomly chosen halos in Figure 2.4 (upper Left). For each halo, we then calculate the standard deviations of these caustic masses over the j jack-knife re-samplings. We plot a histogram (red) of these standard deviations (for all 100 halos) in the lower panels of Figure 2.4 for two different values of N_{gal} (15 and 100). The means of the red histograms in the lower panels of Figure 2.4 define the *average caustic-surface induced scatter* as a function of N_{gal}.

For $N_{gal} = 100$, the distribution of the averages of the mass uncertainties is sharply peaked around a few percent. Therefore, the surface uncertainty plays a negligible role in the total caustic mass uncertainty at $N_{gal} = 100$. By $N_{gal} = 15$, the mean of the distribution shifts to 20% and the distribution becomes less sharply peaked. As a result of the lower density of sampling, the surface we estimate becomes less robust.

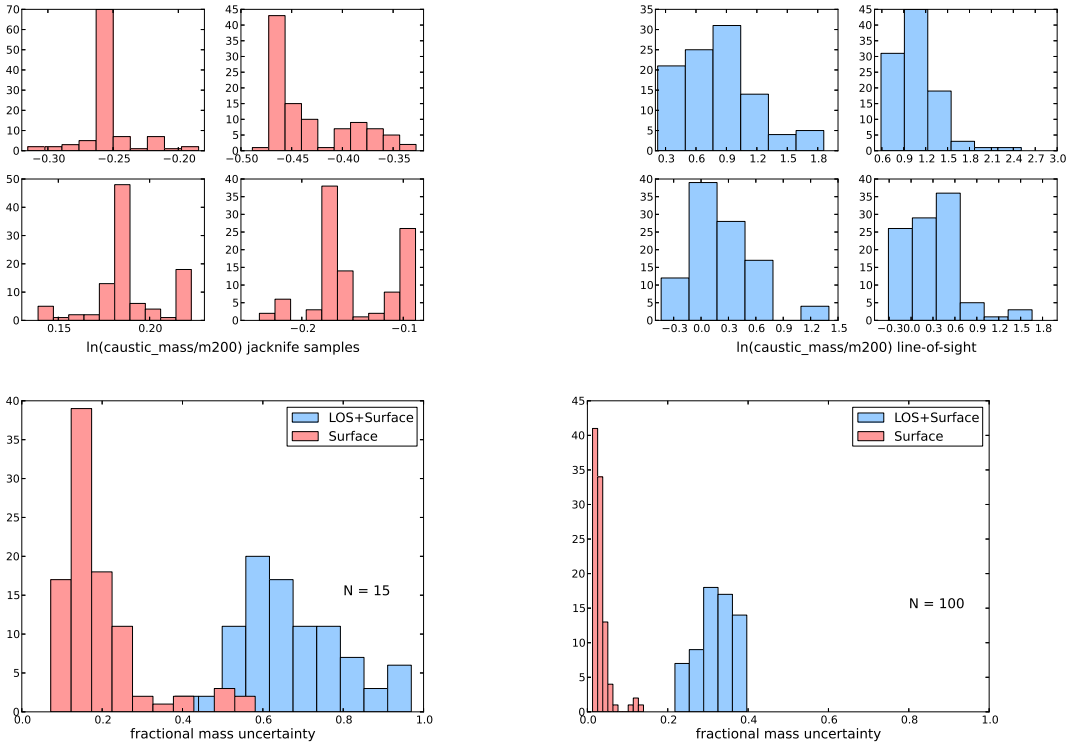

Figure 2.4: **Upper Left**: The distribution of the caustic mass compared to the true mass for four randomly chosen halos from jack-knife re-sampling of 100 galaxies along a single line-of-sight to each halo. While any given caustic mass is biased (high or low), the distributions are typically sharply peaked with small variance. This indicates that any single iso-density surface is well-defined **Upper Right**: The distributions of the caustic mass compared to the true mass over 100 lines-of-sight for four other halos. These distributions are significantly wider with larger variance compared to those in the upper left panel. **Lower Panels**: Histograms of the standard deviations of the distributions in the upper panels for all 100 halos; Left: $N_{gal} = 15$ and Right: $N_{gal} = 100$. Line-of-sight variations (blue) dominate over caustic surface uncertainties (red).

2.3.2 Line-of-Sight Projections

Observationally, we only have one line-of-sight (hereafter abbreviated as "l.o.s") to a cluster in our universe. If clusters are not spherically symmetric in either physical or velocity space, the mass we measure will be dependent on our l.o.s to the cluster. This dependence introduces a l.o.s scatter into our observations which contributes to the scatter in mass relationships. In simulations, we are not bounded to one l.o.s and can make mass measurements along many l.o.s to a single cluster.

We show the distribution of $\ln(M_{c,los}/M_{200})$ for four randomly chosen halos in Figure 2.4 (upper Right) for 100 "l.o.s". Recall that the histograms in the upper left panel of 2.4 are the 100 jack-knife re-samplings of a single line-of-sight. These l.o.s. distributions are much broader than the surface distributions. We again take the standard deviation ($\sqrt{\langle M^2_{c,los}\rangle_{los}}$) as an estimate of the l.o.s scatter for each of our 100 halos. The distribution of these *scatters* is shown in the lower panels of Figure 2.4 in the blue histograms. The means of the blue histograms in the lower panels of Figure 2.4 define the *average line-of-sight induced scatter* as a function of N_{gal}. When $N_{gal} = 100$, we can see that our clusters all exhibit l.o.s scatter between 20-40% with a mean of $\sim 30\%$. By $N_{gal} = 15$, the l.o.s scatter can be anywhere from 40-90% for a given cluster with a mean of $\sim 65\%$.

The mean of the l.o.s caustic mass scatter distributions are shown as a function of N_{gal} in the top panel of Figure 2.5 (dashed lines). Additionally, we show the mean l.o.s scatter in virial mass calculated with equation 2.12 and the mean l.o.s scatter in velocity dispersion. The l.o.s scatters decrease as we increase the N_{gal}. The scatter in l.o.s caustic mass approaches a minimum value of $\sim 30\%$ for large N_{gal} and the virial mass reaches $\sim 45\%$. The scatter in l.o.s velocity dispersion decreases to a minimum of $\sim 15\%$ at $N_{gal} = 150$ which agrees closely with Saro et al. (2013) who find a similar value using all galaxies for a large sample of halos in the De Lucia & Blaizot (2007) semi-analytic catalog.

We also calculate the observed mass scatter in the caustic and virial masses directly by measuring it from Figure 2.3, which represents the scatter we would expect from a single realization of a line-of-sight to each halo. In this case, we take 100 different realizations to determine the expectation value of the scatter, which we plot as a function of N_{gal} in the top panel of Figure 2.5 (solid lines). This scatter is larger than we predict from the statistical distributions determined from Figure 2.4 and shown as the dotted-lines in 2.5. We identify the unaccounted component as originating from an intrinsic scatter in the caustic and virial masses. For instance, Evrard et al. (2008) calculate the intrinsic scatter in the 3D particle velocity dispersion at fixed halo mass to be $\sim 5\%$. From Equation 2.12, this translates to a 15% intrinsic virial mass uncertainty. In Chapter III we calculate the intrinsic scatter for the caustic masses in 3D to be $\sim 10\%$, also using the particles.

This intrinsic (i.e., 3D) uncertainty is a systematic error which should be independent of the systematic uncertainty as a result of projection effects in each l.o.s. To confirm this fact, we perform a Spearman correlation test on $M_{c,los}/\langle M_{c,los}\rangle$ vs. $M_{c,3D}/M_{200}$, where $M_{c,los}$ are all l.o.s mass measurements of a cluster, and $M_{c,3D}$ is the caustic mass measured from the 3-dimensional positions and velocities of the galaxies. We look at 100 l.o.s and find an average correlation coefficient of 0.02 ± 0.1 for the caustic mass and 0.03 ± 0.1 for the virial masses. This confirms that the two (l.o.s. and 3D) systematic uncertainties are uncorrelated. In the bottom panel of Figure 2.5 we add the intrinsic scatter in quadrature to our statistical representations of the line-of-sight scatter (dotted lines in Figure 2.5-top). We then fully recover the observed total scatter to high precision and these are the values we present in Tables 2.1-2.5.

Equation 2.12 implies a relationship of ~ 3 between the log scatter in virial mass and log scatter in velocity dispersion; however, the relationship between scatter in caustic mass and scatter in velocity dispersion is not immediately obvious as the

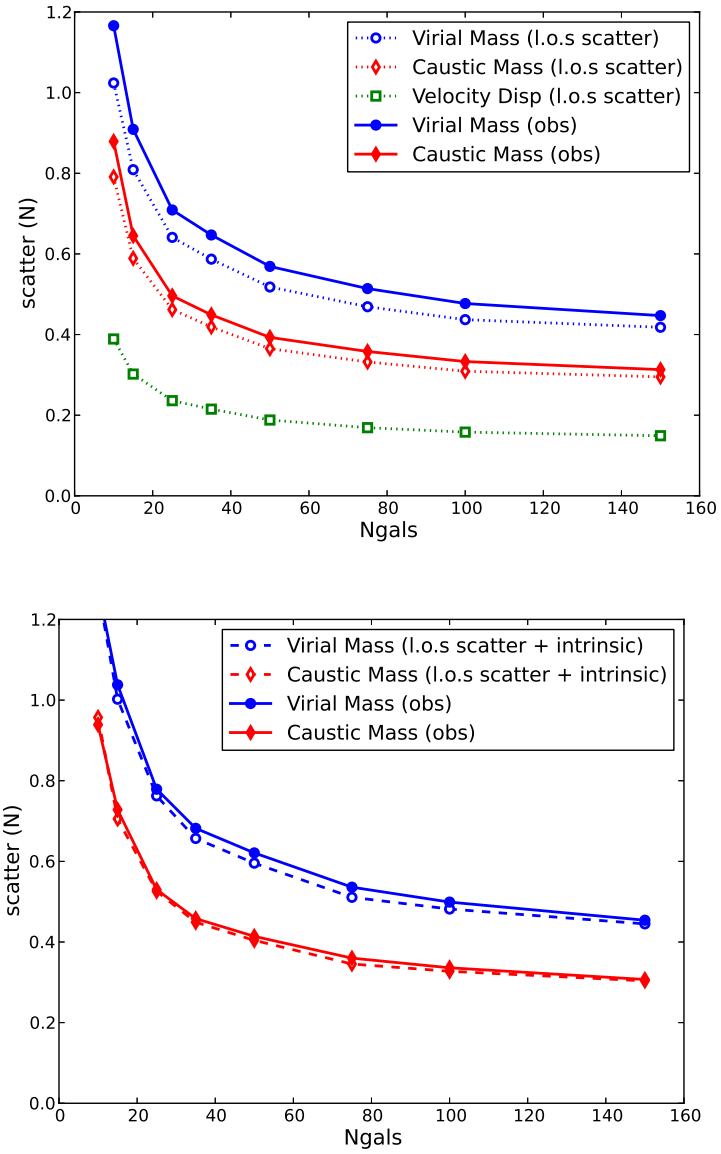

Figure 2.5: **Top**: The scatter in virial mass, caustic mass, and velocity dispersion as a function of N_{gal}. The solid lines represent the observed log scatter for a single line-of-sight to 100 halos from Figure 2.3. The dotted lines are the statistical representation of the line-of-sight scatter from Figure 2.4-bottom. **Bottom**: The solid lines are the same observed scatter (top), but are compared with the predicted mass scatters based on the summation in quadrature of the line-of-sight statistical scatters with the intrinsic 3D mass scatter.

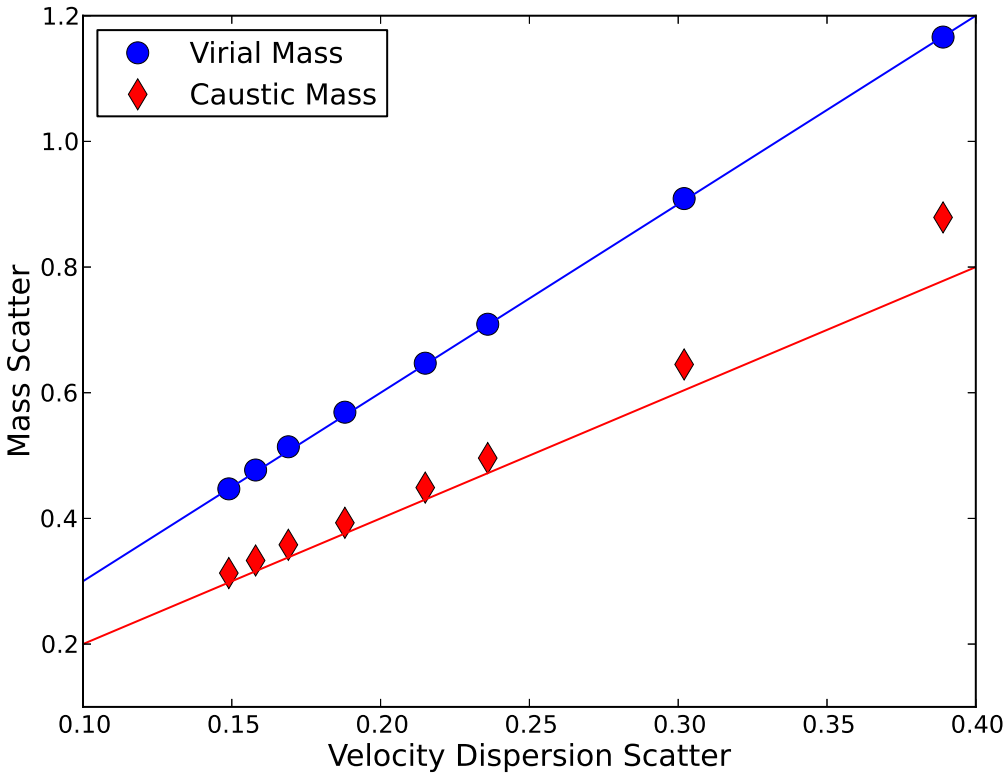

Figure 2.6: Relationship between log scatter in velocity dispersion and log scatter in mass. The blue line predicts the virial mass uncertainties and has a slope of 2.94 as listed in Evrard et al. (2008). The red line predicts the caustic mass uncertainties and has a slope of 2.

two don't have an exact analytic relationship. We do know that the escape velocity surface is calibrated by the velocity dispersion and the caustic mass is calculated by integrating the $\langle v_{esc}^2 \rangle(r)$. A naive assumption is that the scatter in velocity dispersion dominates over all other systematic scatters in the caustic technique. If so, we should find that the log scatter in caustic mass is very nearly twice that of the log scatter in velocity dispersion.

In Figure 2.6 we show that the virial mass obeys the predicted log mass-velocity dispersion scatter relation (blue line) as expected. We also show that the sensitivity of the scatter in caustic mass is well predicted by twice the scatter in velocity dispersion (red line); however the absolute value is slightly higher due to other systematic sources of uncertainty. This implies that other forms of systematic uncertainty in the technique are indeed small, and that the line-of-sight scatter in velocity dispersion dominates the uncertainty in caustic mass, albeit to a lesser degree than it does in the virial mass.

In addition to the mass scatter for a given N_{gal}, we also show how the average mass bias depends on N_{gal}. As before with the total scatter, we measure the average bias for the 100 halos as $\langle \ln(M_c/M_{200}) \rangle$ after choosing only one l.o.s to each. We repeat this measurement for 100 different l.o.s and report the average sample bias. The bias in caustic mass is shown in Figure 2.7 (Middle) for all 4 semi-analytics and the subhalos. At small N_{gal} the caustic mass can be biased very low compared with M_{200}. However, above $N_{gal} = 50$, the log bias is unbiased and all the semi-analytics agree to within the 1σ-errors. A similar trend is seen with the virial mass (Left), but when compared with the caustic mass, the virial mass exhibits a larger bias for small N_{gal}. The virial mass bias, and to a lesser degree the caustic mass bias, are dependent on the velocity dispersion bias which is shown as a function of N_{gal} in 2.7 (Right). We find that the four different semi-analytics generally agree to within the errors on the means (from the 100 l.o.s.). The Bower et al. (2006) galaxies are always

lower than the others, but not significantly. The sub-halos are biased high in velocity dispersion by 15% with high sampling which translates to a caustic mass bias of 30%. We discuss these trends in Section 2.4.1

2.3.3 Target Selection

Up to now, we have assumed that we have spectroscopic follow-up that is complete for the N brightest galaxies within the projected r_{200} of each halo. Here, we drop that constraint and allow more realistic targeting algorithms. We include selection based on galaxy magnitude, membership within the red-sequence, and projected distance from the cluster center.

In Figure 2.8 we keep N_{gal} and color constant (i.e., only the red sequence) and show the bias (Top) and scatter (Bottom) as we decrease the fraction of original brightest (in absolute magnitude) galaxies. Starting from the sorted 50 brightest galaxies, we have different options for how we replace galaxies. For instance, we could replace them randomly, or from the brightest to the dimmest, or from the dimmest to the brightest, etc. In Figure 2.8 we show two different replacement techniques starting from the *dimmest* (solid lines) or *brightest* galaxies (dashed lines). We always keep the 5 brightest galaxies in each case, and we replace galaxies with those starting from the 51^{st} brightest within r_{200}. We find that the bias does not depend on in how the replacement is done. As shown in Figure 2.8, the virial mass is more affected by target selection based on galaxy luminosity than the caustic mass. To minimize brightness-induced mass biases, the Guo et al. (2011) semi-analytics indicate that one should always strive to target the brightest galaxies. There is no change in the average scatter as dimmer galaxies are added to the sample.

In Figure 2.9, we keep N_{gal} constant and show the bias (Top) and scatter (Bottom) as a function of red galaxy fraction. We start with the $N = 50$ brightest red-sequence galaxies, and replace the dimmest fraction of those galaxies with the brightest blue

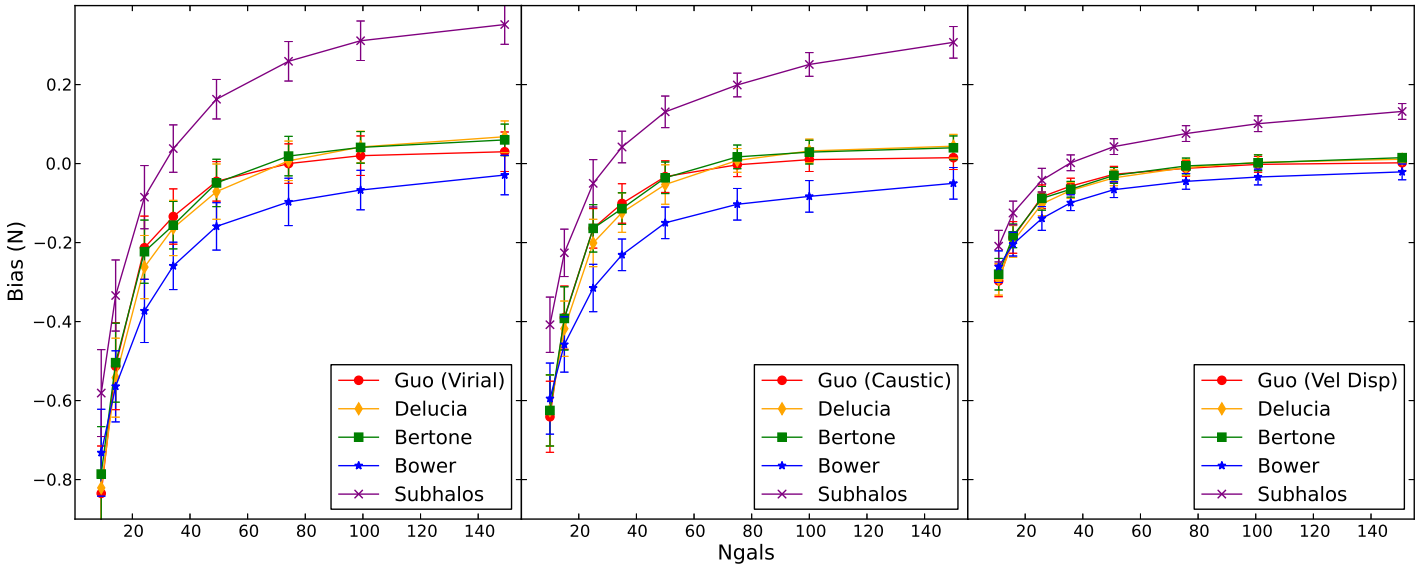

Figure 2.7: The bias in virial mass **Left**, caustic mass **Middle**, and velocity dispersion **Right** as a function of the number of galaxies (N_{gal}) used in the mass determination. The biases are shown for the Guo (red), De Lucia (orange), Bertone (green), and Bower (blue) semi-analytics as well as the subhalos (purple). N_{gal} is the dominant source of bias in the caustic mass as well as the virial mass, and the semi-analytic biases all converge to within errors at high sampling.

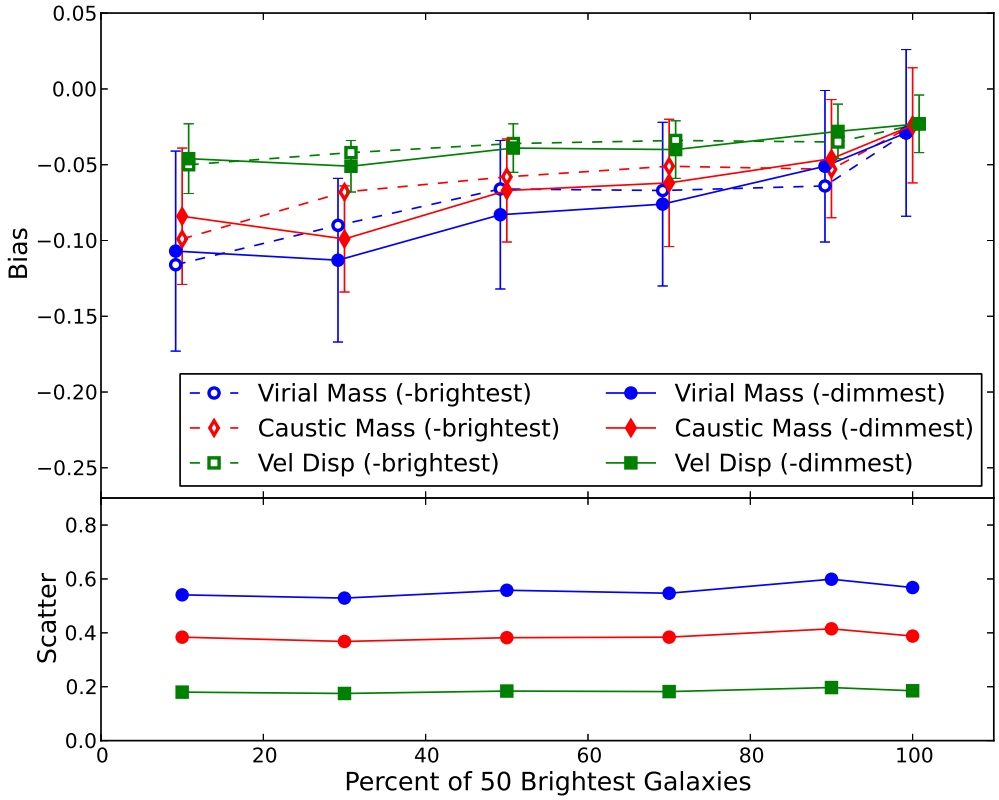

Figure 2.8: **Top**: The velocity segregation bias as a function of the fraction of the brightest galaxies within a projected r_{200} used in the caustic mass. The x-axis indicates the fraction of the 50 brightest galaxies. We keep the total number of galaxies fixed by replacing bright galaxies those dimmer than the 50^{th} brightest. We replace galaxies by starting from the dimmest (solid lines) or by starting from the brightest (dashed-see text) but always keep the 5 brightest galaxies. The errors are the uncertainties on the mean bias. **Bottom**: The log sample scatter for the brighter sample (solid lines above), however the scatter for the dimmer sample is nearly identical in all cases.

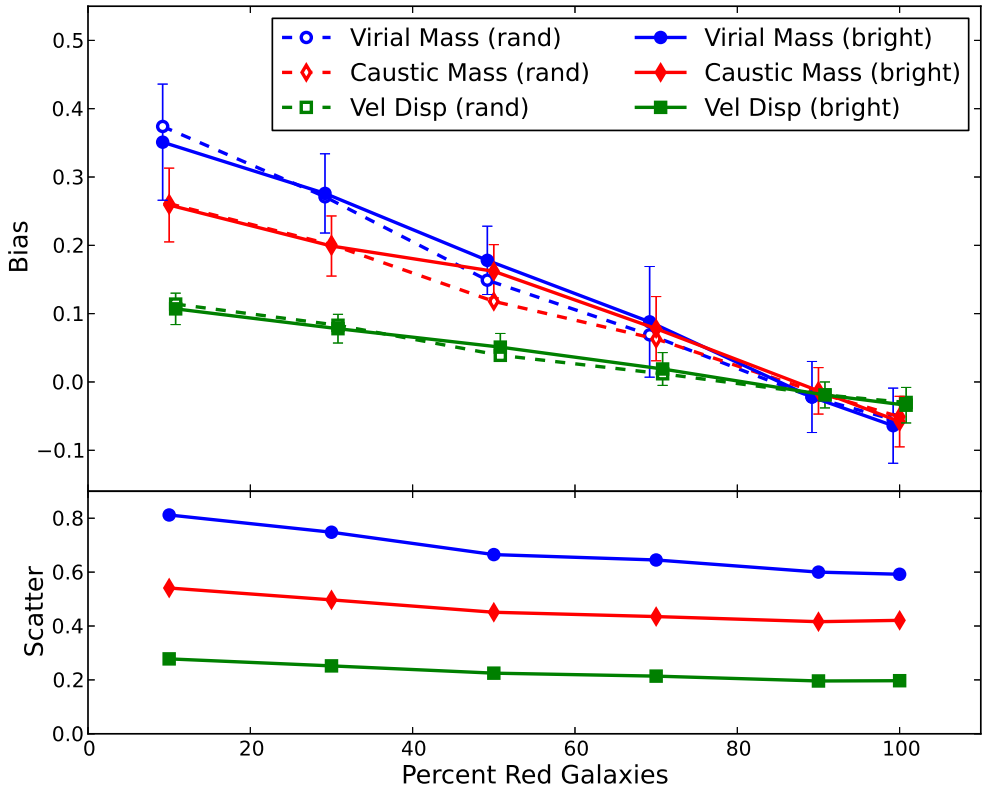

Figure 2.9: **Top**: The bias in caustic mass (red diamonds), virial mass (blue circles) and velocity dispersion (green squares) when the brightest "x" percent of red galaxies are used out of a total of 50 (solid lines) and a random "x" percent of red galaxies are used out of a total of 50 (dashed lines). The remaining percent added to keep N_{gal} constant are the brightest blue galaxies (solid lines) and a random selection of blue galaxies (dashed lines). We detect a bias from velocity segregation based on color. **Bottom**: The log sample scatter for the brighter sample (solid lines above), however the scatter for the random sample is nearly identical in all cases.

non-red-sequence galaxies within the projected r_{200}. We also conduct the test by replacing the galaxies randomly, with no noticeable difference in the results.

Color plays a bigger role in selection-induced biases and scatter when compared to brightness and again, the virial masses are more affected than the caustic masses. The velocity dispersion can be biased as much as 10% higher than the baseline bias when only 25% of the sample are bright red sequence galaxies and the rest are bright bright blue galaxies. Consequently, we see the average bias for both caustic mass and virial mass change from a slight negative bias for purely red-sequence galaxies of -5%, to a positive bias of $\sim 25\%$ and $\sim 35\%$ respectively when we use a small fraction of the original red sequence sample. This is the color-dependent velocity segregation effect noticed in real data (Carlberg et al., 1997b; Goto, 2005) and it is due to the inclusion of blue galaxies with higher infall velocities. Decreasing the fraction of bright red galaxies to bright blue galaxies can also increase the expected scatter in mass by as much as 15% in caustic mass and 20% in virial mass as compared with the sample of all red sequence galaxies. This is due to the higher velocities of the typically infalling blue galaxy population that can depend more on l.o.s to a cluster. It is very important to target the bright red galaxies in order to avoid this color-selection induced bias.

In Figure 2.10 (Top), we show the bias (Top:Upper) and scatter (Top:Lower) as a function of the core fraction. We start with the $N = 50$ brightest galaxies, and replace the dimmest galaxies whose projected locations are within 200kpc of the center with galaxies whose projected radii are greater than 700kpc from the center. This simulates survey data that under-samples the core due to fiber collisions or slit overlap in the dense inner regions of clusters and cannot extract spectra for all observable galaxies. On the other hand, it is often the case where nearby massive clusters are not well-sampled out to the virial radius and beyond. In Figure 2.10 (Bottom) we show the bias (Bottom:Upper) and scatter (Bottom:Lower) as a function of the outskirt "wing" fraction. Starting with the $N = 50$ brightest galaxies, we replace the dimmest

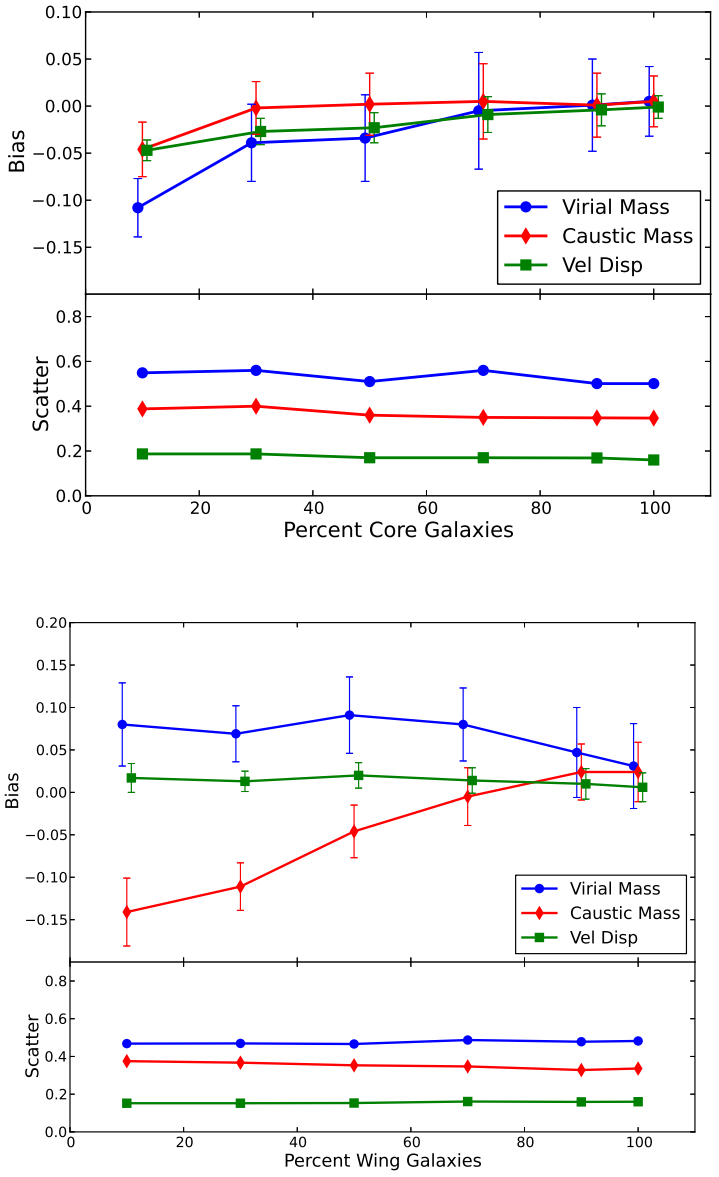

Figure 2.10: **Top**: The bias (Top:Upper) and scatter (Top:Lower) in caustic mass (red diamonds), virial mass (blue circles) and velocity dispersion (green squares) when the dimmest galaxies within the innermost projected 200kpc are replaced with galaxies with projected radii outside 700kpc from the center to simulate an under-sampled core. **Bottom**: Same as top, only now the dimmest galaxies outside a projected radius of 700kpc are replaced with galaxies within the inner-most projected 200kpc to simulate an under-sampled outskirts or "wings" region.

galaxies whose projected radii are greater than 700kpc with galaxies that are within 200kpc from the center.

In the first case, the more we under-sample the core relative to the outskirts, the more biased our estimates become of mass and velocity dispersion. This is true regardless of whether we use the virial relation or the caustic technique. No matter how much we under-sample the core, the caustic inferred masses are less biased than the virial estimates. This is due to the fact that the caustic technique does not depend as heavily on uncertainty in velocity dispersion (see Figure 2.6), and under-sampling the projected core of a cluster will lower the measured velocity dispersion. We see no effect on the mass scatter when under-sampling the core.

When we under-sample the outskirts or "wings" relative to the core, we see dramatically different responses from the caustic and virial mass estimators. Under-sampling the outskirts has the effect of raising the measured velocity dispersion. This is because the galaxies with large l.o.s velocity are preferentially projected near the cluster core while under-sampling the outskirts removes galaxies with preferentially smaller l.o.s velocities. This raises the virial mass estimate as it is directly proportional to velocity dispersion. However, the caustic inferred masses exhibit the opposite trend since we are reducing the phase-space density in the outer regions by removing these galaxies. The mass scatter is unaffected by under-sampling the outskirts. To minimize radial-selection induced biases, it is important to evenly sample the phase space.

2.4 Discussion

With the availability of large and complete spectroscopic surveys like the Sloan Digital Sky Survey (Stoughton et al., 2002, SDSS) and GAMA (GAlaxy Mass and Assembly GAMA Driver et al., 2011), highly multiplexed multi-object optical spectroscopy on 8m class telescopes (IMACS Dressler et al., 2011), VIMOS (Le Fèvre

et al., 2003), DEIMOS (Davis et al., 2003)), and the latest generation of multi-object near-infrared spectrographs (MMIRS McLeod et al., 2004), Flamingos 2 (Eikenberry et al., 2006), MOSFIRE (McLean et al., 2008), we can measure large numbers of galaxy velocities in clusters from $z \sim 0$ to $z \sim 1.5$. And just as we can use three different observables to infer the masses of clusters (see Section 2.1), we can use the galaxy velocities in three different ways to infer dynamical mass (e.g., via virial scaling, the Jean's equation, and the escape velocity). The questions then are how well do these different dynamical techniques work under realistic observing conditions and how do they compare. Here, we compare the virial relation via the velocity dispersion (Evrard et al., 2008) and the escape velocity mass inferred from the caustic technique (Diaferio & Geller, 1997).

2.4.1 Robustness of the Caustic Technique to the Galaxy Models

We examine four different semi-analytic mock galaxy catalogs, as well as the sub-halos and the particles in the Millennium Simulation. The measured scatter and bias in the inferred dynamical masses are quantified in Tables 2.1-2.5. The level of scatter and bias varies by only a few percent between most of the different semi-analytic tracers. The exception is for the Bower et al. (2006) galaxies, which sometimes differ by slightly more than the 1σ errors on the bias estimates. In one sense, this robustness is not surprising, since the majority of galaxies in the semi-analytics are attached to sub-halos, which are the same for each of the mock galaxy catalogs. However, there are a variety of rules which are applied to the "orphan" population (see Section 2.2.3). For the satellite population, these orphan galaxies are quite common at low stellar masses, while the exact fraction depends on the semi-analytic rule-set. In the semi-analytic catalogs studied here, the fraction of $N = 50$ brightest galaxies that are orphans ranges from 50% (Bower) to 25% (Guo).

Consider some of the differences in the orphan population between the Bower et al.

(2006) semi-analytics compared to De Lucia & Blaizot (2007), Bertone et al. (2007), and Guo et al. (2011): The Bower sample uses a merger tree that differed in how friend-of-friend groups were defined, how spuriously linked halos were handled, how independent halos were identified, and how descendants of halos were tracked through time; the Bower sample includes the sub-halo orbital energy and angular momentum when calculating the merging timescale of the orphans; the Guo et al. (2011) semi-analytics go one step further by modeling the orbital decay of the orphans before they are destroyed.

These algorithmic differences manifest as variations in the spatial distribution of the satellites within the halos. The De Lucia semi-analytic galaxies have much flatter density profiles within the virial radius when compared to the Bower et al. (2006) galaxies (Budzynski et al., 2012). Since the $r-v$ phase-space is different between the semi-analytics, one might expect that the caustic technique (which is based on the phase-space density) would also differ significantly. However, this is not the case and even when the orphan fraction and radial densities differ by factors of two or more, the caustic masses vary by $< 10\%$. We interpret this lack of difference between the different semi-analytic techniques as a measure of the robustness of the technique to large systematic variations in the $r-v$ velocity distribution function.

The one exception to this robustness is for the sub-halo population where we detect large biases in the velocity dispersion compared to the dark matter. Since the caustic mass is calibrated using the velocity dispersion, this bias carries through into a bias in both the virial mass and the caustic mass. We attribute this to how poorly the sub-halos trace the $r-v$ phase-space within halos in simulations with resolution similar to the Millennium Simulation (see also Budzynski et al., 2012).

One could ask whether the semi-analytic techniques have converged in their representation of the $r-v$ phase-space inside clusters, as represented by the fraction of orphan galaxies. Faltenbacher & Diemand (2006) have shown that at higher res-

olutions, galaxies are no longer orphaned from sub-halos. Instead, a new "crisis" of sub-halo over-abundance presents itself. Faltenbacher & Diemand (2006) also show that this crisis is averted through rule-sets analogous to the ones used at lower resolution. In other words, instead of following the most-bound particle of a destroyed sub-halo, one attaches semi-analytic galaxies only to those sub-halos that previously achieved some minimal mass threshold before entering the cluster. The velocity dispersion of these semi-analytic galaxies is unbiased with respect to the dark matter, which is what we already find here.

2.4.2 The Scatter and Bias of Dynamical Cluster Mass Estimates

While none of these semi-analytic prescriptions is how nature places galaxies into halos, we have established that the virial relation and the caustic technique are robust to variations in their rule-sets. This baseline allows for a comparison of the absolute levels of the inferred mass biases and scatters between the virial and the caustic techniques.

For a fixed number of tracers projected to lie within R_{200} of the clusters, the scatter in the caustic mass $\ln M_c$ at fixed $\ln M_{200}$ is about 1/3 smaller than M_{virial}. In other words, at fixed N, the caustic technique is a more precise estimate of the true halo mass compared to the virial relation. The growth of the mass scatter as N_{gal} decreases is the same for the two techniques. As with the virial relation and the velocity dispersion, the dominant component of the scatter in the caustic mass is from the line-of-sight variations in the observed velocity dispersion and phase-space density (see also White et al. (2010); Saro et al. (2013)). Uncertainties in M_c induced from the sampling of the phase space do not contribute unless $\mathrm{N}_{gal} < 25$, below which they quickly grow to be a dominant component.

In Figure 2.7 we show the strong dependence of the bias on the number of tracers used in the mass calculation. Saro et al. (2013) suggest that this was due to dynamical

friction, since we (as they) explicitly restrict the sub-samples to the brightest galaxies. However at fixed N, large variations in the brightness distribution of the galaxies has only a small affect on the observed bias. The same can be said for color selection (see Figure 2.9). Thus while velocity segregation from sub-sampling plays a role, it is minimal compared to the number of galaxies used in the mass determination. This holds for both the virial masses as well as the caustic masses. Put simply, if a targeting algorithm requires a trade-off between number and color, number wins.

Regardless of how biases are introduced into the velocity distributions (e.g., through number, brightness, or color) the caustic mass is less affected than the virial mass. The trends in the biases for the virial and caustics masses are similar. The exception is when radial selection constraints are applied. We find that the velocity dispersion is more susceptible to incompletenesses in the core sampling while the caustic technique is more susceptible to incompletenesses in the cluster outskirts. The former trend can be understood from a dynamically cold population of galaxies which dominates the dispersion measurement at low sampling. The latter is also a sampling issue, where the iso-density contour gets lost in the background for low sampling in the cluster outskirts.

2.4.3 The Calibration Factor

Finally, we note that the implementation of the caustic technique utilizes a step which calibrates to simulations (see $\mathcal{F}_\beta$ in equation 2.10). This is no different than the virial calibration (equation 2.12). Diaferio (1999) find $\langle \mathcal{F}_\beta(r) \rangle = 0.5$ and Serra et al. (2011) find $\langle \mathcal{F}_\beta(r) \rangle = 0.7$, which corresponds to a systematic uncertainty of 30% in mass. This is larger than any biases we detect from sample selection.

One explanation the difference in the value for $\mathcal{F}_\beta$ is in how Diaferio (1999) and Serra et al. (2011) define their mock galaxy catalogs: the former used only halos (with ten particles or more) while the latter used only particles to define galaxies. Since sub-

halos in N-body simulations are biased tracers of the dark matter velocity dispersions, the calibration factor and caustic masses will also be biased (see Figure 2.7 middle and right panels). We test this hypothesis by re-calibrating $\mathcal{F}_\beta$ using the Millennium Simulation sub-halos alone. The high halo velocity dispersions of the sub-halos require a lower calibration factor than from the dark matter. We find $\langle \mathcal{F}_\beta(r) \rangle = 0.5$, identical to what is used in Diaferio (1999), who note that their own halo velocity dispersions are biased with respect to the dark matter in their simulations. Serra et al. (2011) explicitly used dark matter particle positions and velocities to define their galaxies and calibrate $\mathcal{F}_\beta$. The semi-analytics we use lie in between these two extremes, which explains why we find $\langle \mathcal{F}_\beta(r) \rangle = 0.65$.

Serra et al. (2011) notes that $\mathcal{F}_\beta$ is not constant with radius in simulations and that the caustic mass profiles can over-estimate the mass within $\sim 0.3 r_{200}$, where velocity anisotropies become smaller. Likewise, Geller et al. (2013) compare caustic-derived and weak-lensing-derived mass profiles and find disagreement within $0.5 r_{200}$, as expected from the anisotropy profiles in simulations. In this work, we are not measuring mass profiles but instead the integrated masses of the clusters out to r_{200}. As shown in Serra et al. (2011), unbiased halo masses require an appropriate measure of $\langle \mathcal{F}_\beta(r) \rangle = \int_0^r \mathcal{F}_\beta(r) dx/r$ from Equation 2.10, which is what we do to achieve unbiased caustic masses for the Guo et al. (2011) semi-analytic galaxies. This is without question a tuning step which carries with it a certain level of additional systematic uncertainty.

It is very unlikely that the radius-velocity phase-space of galaxies in the Universe is represented by the sub-halo population in N-body simulations (regardless of resolution). Current observational constraints on the bias between the galaxy and dark matter velocity dispersions are measured indirectly (e.g., Rines et al. (2008)) and find it to be $< 5\%$ when a multitude of independent cosmological priors are leveraged. From the current simulation and observational work, it is not likely that

$\langle \mathcal{F}_\beta(r) \rangle = 0.5$, which corresponds to a galaxy/dark matter velocity bias of 10% in a ΛCDM simulation (see Table 2.5 sub-halos). If galaxies and dark matter have dispersions that are unbiased with respect to each other, the caustic masses (integrated to r_{200}) would be low by $\sim$20% using $\langle \mathcal{F}_\beta(r) \rangle = 0.5$ (Geller et al., 2013; Rines et al., 2013).

Ideally, the simulation calibration factor can be dropped entirely, and in Chapter III we present a revised derivation of the caustic technique that relies only on the observable parameters: the NFW density scale parameter, $\langle v^2_{esc,los} \rangle$, and $\langle \beta \rangle$ and their statistical and systematic uncertainties.

2.5 Summary

In this work, our main conclusions are as follows.

- We measure velocity dispersions, virial masses (M_{virial}), and caustic masses (M_c) for 100 halos in the Millennium Simulation with masses $10^{14} - 10^{15} M_\odot$. These halos exist at low redshift ($z < 0.15$) and are populated with galaxies via four different semi-analytic prescriptions (Guo et al., 2011; De Lucia & Blaizot, 2007; Bower et al., 2006; Bertone et al., 2007).

- The resulting scatter and bias in M_c relative to the halo mass (M_{200}) is robust and largely independent of the semi-analytic prescription used to populate cluster-size dark matter halos with galaxies. The exception is when only subhalos are observed which do not trace the dark matter velocity field and measured velocity dispersions. The velocity dispersion for the subhalos can be biased high by 10-15% resulting in a caustic mass bias of 20-30%.

- As with the M_{virial}, the dominant component of the scatter in M_c is from the line-of-sight variations in the observed velocity dispersion. However, for a fixed number of tracers (N_{gal}) projected to lie within R_{200} of the clusters, the scatter

in the caustic mass $\ln(M_c|M_{200})$ is $\sim 30\%$ at $N_{gal} > 50$ which is $\sim 1/3$ smaller than M_{virial}.

- The bias in M_c relative to M_{200} is strongly dependent on N_{gal}. While color selection, radial completeness, and magnitude can play a role in inducing bias depending on how a cluster is observed, their effect is much less than N_{gal}. Given a choice, it is better to use a full, unrestricted sample to estimate caustic masses rather than a color selected (such as red sequence) sample to achieve larger numbers.

- We find a caustic mass calibration factor $\mathcal{F}_\beta = 0.65$. This differs from the calibrations based on either just the dark matter particles ($\mathcal{F}_\beta = 0.7$) or just the subhalos ($\mathcal{F}_\beta = 0.5$). While galaxy/DM velocity bias affects the caustic mass less than the dynamical mass, it is an important component of the total systematic uncertainty.

Guo

Velocity Dispersion and Caustic Mass bias/scatter

	σ_N^v		Virial Mass		Caustic Mass		Orphans
N	Bias	Scatter	Bias	Scatter	Bias	Scatter	Fraction
	$\langle \ln(\sigma^v/\sigma_{dm}) \rangle$	$\langle \ln(\sigma^v/\sigma_{dm})^2 \rangle^{1/2}$	$\langle \ln(M_v/M_{200}) \rangle$	$\langle \ln(M_v/M_{200})^2 \rangle^{1/2}$	$\langle \ln(M_c/M_{200}) \rangle$	$\langle \ln(M_c/M_{200})^2 \rangle^{1/2}$	
150	0.00±0.02	0.15	0.03±0.05	0.45	0.01±0.03	0.31	0.40
100	0.00±0.02	0.17	0.02±0.05	0.50	0.01±0.03	0.33	0.34
75	-0.01±0.02	0.18	0.00±0.05	0.54	0.00±0.03	0.36	0.30
50	-0.03±0.02	0.21	-0.05±0.05	0.62	-0.03±0.04	0.41	0.26
35	-0.06±0.02	0.23	-0.13±0.07	0.68	-0.10±0.05	0.46	0.25
25	-0.08±0.03	0.26	-0.21±0.08	0.78	-0.16±0.05	0.53	0.23
15	-0.19±0.04	0.35	-0.51±0.11	1.04	-0.39±0.08	0.73	0.21
10	-0.30±0.04	0.40	-0.84±0.12	1.28	-0.64±0.09	0.94	0.21

Table 2.1: Guo Semi-analytic results.

De Lucia
Velocity Dispersion and Caustic Mass bias/scatter

	σ_N^v		Virial Mass		Caustic Mass		Orphans
N	Bias	Scatter	Bias	Scatter	Bias	Scatter	Fraction
	$\langle \ln(\sigma^v/\sigma_{dm}) \rangle$	$\langle \ln(\sigma^v/\sigma_{dm})^2 \rangle^{1/2}$	$\langle \ln(M_v/M_{200}) \rangle$	$\langle \ln(M_v/M_{200})^2 \rangle^{1/2}$	$\langle \ln(M_c/M_{200}) \rangle$	$\langle \ln(M_c/M_{200})^2 \rangle^{1/2}$	
150	0.01±0.01	0.15	0.06±0.04	0.45	0.04±0.03	0.31	0.36
100	0.00±0.02	0.16	0.04±0.04	0.49	0.03±0.03	0.33	0.32
75	-0.01±0.02	0.18	0.01±0.05	0.54	0.01±0.03	0.36	0.30
50	-0.04±0.02	0.21	-0.07±0.07	0.62	-0.05±0.05	0.42	0.28
35	-0.07±0.02	0.23	-0.16±0.07	0.68	-0.12±0.05	0.46	0.28
25	-0.10±0.03	0.26	-0.26±0.08	0.80	-0.20±0.06	0.54	0.26
15	-0.20±0.04	0.35	-0.54±0.10	1.03	-0.42±0.07	0.73	0.25
10	-0.29±0.04	0.43	-0.82±0.13	1.29	-0.63±0.09	0.96	0.23

Table 2.2: De Lucia Semi-analytic results.

Bertone

Velocity Dispersion and Caustic Mass bias/scatter

	σ_N^v		Virial Mass		Caustic Mass		Orphans
N	Bias $\langle \ln(\sigma^v/\sigma_{dm}) \rangle$	Scatter $\langle \ln(\sigma^v/\sigma_{dm})^2 \rangle^{1/2}$	Bias $\langle \ln(M_v/M_{200}) \rangle$	Scatter $\langle \ln(M_v/M_{200})^2 \rangle^{1/2}$	Bias $\langle \ln(M_c/M_{200}) \rangle$	Scatter $\langle \ln(M_c/M_{200})^2 \rangle^{1/2}$	Fraction
150	0.02±0.01	0.15	0.06±0.04	0.44	0.04±0.03	0.29	0.39
100	0.00±0.02	0.16	0.04±0.04	0.48	0.03±0.03	0.32	0.34
75	-0.01±0.02	0.18	0.02±0.05	0.54	0.02±0.03	0.36	0.31
50	-0.03±0.02	0.21	-0.05±0.06	0.62	-0.04±0.04	0.41	0.27
35	-0.07±0.02	0.23	-0.16±0.06	0.68	-0.11±0.04	0.46	0.26
25	-0.09±0.03	0.27	-0.22±0.08	0.80	-0.16±0.06	0.54	0.25
15	-0.18±0.03	0.34	-0.50±0.10	1.02	-0.39±0.08	0.72	0.25
10	-0.28±0.04	0.42	-0.79±0.12	1.27	-0.63±0.09	0.95	0.25

Table 2.3: Bertone Semi-analytic results.

Bower

Velocity Dispersion and Caustic Mass bias/scatter

	σ_N^v		Virial Mass		Caustic Mass		Orphans
N	Bias $\langle \ln(\sigma^v/\sigma_{dm}) \rangle$	Scatter $\langle \ln(\sigma^v/\sigma_{dm})^2 \rangle^{1/2}$	Bias $\langle \ln(M_v/M_{200}) \rangle$	Scatter $\langle \ln(M_v/M_{200})^2 \rangle^{1/2}$	Bias $\langle \ln(M_c/M_{200}) \rangle$	Scatter $\langle \ln(M_c/M_{200})^2 \rangle^{1/2}$	Fraction
150	-0.02±0.02	0.15	-0.03±0.05	0.48	-0.05±0.04	0.33	0.55
100	-0.03±0.02	0.16	-0.06±0.05	0.51	-0.08±0.04	0.36	0.52
75	-0.04±0.02	0.18	-0.09±0.05	0.55	-0.11±0.04	0.39	0.51
50	-0.06±0.02	0.21	-0.14±0.06	0.63	-0.14±0.04	0.43	0.49
35	-0.09±0.02	0.22	-0.24±0.05	0.67	-0.21±0.04	0.49	0.48
25	-0.13±0.02	0.26	-0.36±0.07	0.78	-0.30±0.05	0.55	0.46
15	-0.21±0.03	0.32	-0.58±0.09	0.96	-0.48±0.07	0.71	0.43
10	-0.27±0.04	0.41	-0.74±0.12	1.21	-0.59±0.09	0.93	0.39

Table 2.4: Bower Semi-analytic results.

Subhalos
Velocity Dispersion and Caustic Mass bias/scatter

	σ_N^v		Virial Mass		Caustic Mass	
N	Bias	Scatter	Bias	Scatter	Bias	Scatter
	$\langle \ln(\sigma^v/\sigma_{dm}) \rangle$	$\langle \ln(\sigma^v/\sigma_{dm})^2 \rangle^{1/2}$	$\langle \ln(M_v/M_{200}) \rangle$	$\langle \ln(M_v/M_{200})^2 \rangle^{1/2}$	$\langle \ln(M_c/M_{200}) \rangle$	$\langle \ln(M_c/M_{200})^2 \rangle^{1/2}$
150	0.13±0.02	0.21	0.35±0.05	0.63	0.31±0.04	0.41
100	0.10±0.02	0.21	0.31±0.05	0.64	0.25±0.04	0.39
75	0.08±0.02	0.21	0.26±0.05	0.63	0.20±0.04	0.40
50	0.04±0.02	0.21	0.16±0.05	0.65	0.13±0.04	0.43
35	0.00±0.02	0.23	0.04±0.06	0.69	0.04±0.04	0.47
25	-0.04±0.03	0.27	-0.09±0.08	0.81	-0.05±0.06	0.54
15	-0.13±0.03	0.33	-0.33±0.09	1.01	-0.23±0.06	0.69
10	-0.21±0.04	0.41	-0.58±0.11	1.23	-0.41±0.07	0.83

Table 2.5: Subhalos results.

CHAPTER III

The Theory of Mass Estimation Using Observed Cluster Potentials

3.1 Introduction

Under Newtonian dynamics, the escape velocity is related to the gravitational potential of the system,

$$v_{esc}^2(r) = -2\Phi(r). \tag{3.1}$$

If the dynamics of the system are controlled by the gravitational potential, tracers which cannot escape the potential exist in a well-defined region of radius/velocity $(r - v)$ phase space. The extrema of the velocities in this phase space define a surface, the escape velocity profile, $v_{esc}(r)$, which can be observed in projected sky coordinates. Given the observed $v_{esc}(r)$, this "caustic" technique allows one to infer the mass profile of a cluster to well beyond the virial radius (Diaferio & Geller, 1997).

With the latest deployments of wide-field ground-based multi-object spectrographs like VIMOS on the VLT (Le Fèvre et al., 2003); IMACS on Magellan (Dressler et al., 2011); HECTOSpec[1] on the MMT we are beginning to see large spectroscopic follow-up datasets of galaxy clusters. As a consequence, the caustic technique has become more widely adopted.

[1] http://www.cfa.harvard.edu/mmti/hectospec

Geller et al. (2013) compare caustic to weak lensing mass profiles and find agreement to within 30% around a virial radius. Lemze et al. (2009) perform a dynamical study of the cluster A1689 and find good agreement between the caustic mass profiles and both the weak lensing and X-ray inferred mass profiles. Rines et al. (2013) measure the caustic mass profiles to large radii to estimate the ultimate halo mass in clusters, which includes all mass bound to halos in a future ΛCDM universe. Andreon & Hurn (2010) utilize caustic masses to help calibrate the M_{200}-richness relation alongside mass estimates from velocity dispersion scaling relations. New deep imaging surveys like CLASH on the Hubble Space Telescope have been awarded a significant amount of Very Large Telescope (VLT) time to collect spectroscopy, in part to study the dynamical and caustic masses of clusters (Postman et al., 2012). And of course there are a variety of planned large-scale spectroscopy programs both from the ground (BigBoss[2]) and space (EUCLID[3]). These future efforts could enable caustic masses to be measured for many thousands of galaxy clusters.

In Chapter II we use the Millennium Simulation (Springel et al., 2005) to show that cluster-sized caustic masses within a projected r_{200} (the radius which contains 200 times the critical density) are more precise and more accurate than virial masses measured from their projected velocity dispersions. However, the implementation of the escape velocity technique employs a number of steps which result in masses that are calibrated to the N-body simulation. Cluster masses based on the traditional caustic technique vary by 30% depending on which calibration is used (Diaferio & Geller, 1997; Diaferio, 1999; Serra et al., 2011). In this chapter, we clarify where these calibrations are incorporated into the theory and we assess their validity and impact on the inferred masses. We also present a variation on the original escape velocity caustic technique which eliminates the calibration.

[2]http://bigboss.lbl.gov/
[3]http://sci.esa.int/euclid

3.2 Tracers of the Escape Velocity Profile

An important question is whether the caustic edge defined by the particles in $r-v$ phase-space varies based on the dynamical tracers being considered. For instance, while we expect that sub-halos will exhibit a different phase-space distribution than particles based on astrophysical interactions, the edge should be equivalently defined since the escape velocity is a limiting property. To test this, we use resolved sub-halos defined for the Millennium simulation (Springel et al., 2005) by the SUBFIND algorithm (Springel et al., 2001) along with the dark matter particles in the simulation. As an example, the sub-halos for two clusters are shown as the orange circles in Figure 3.1 and the particles are shown as black dots. There are two important issues with the sub-halos that are evident in this figure. First, the sub-halos decrease in density towards the core while the particles increase in density. Second, the sub-halos do not track the phase-space near $\Delta v = 0$ within r_{200}. Both of these effects are the result of sub-halo destruction through gravitational interactions with the density field: galaxies would not be destroyed so easily. However, by using only the sub-halos which have survived mergers as a tracer of the particle phase-space, one is weighting the velocity distribution in an unfair way with respect to both the dark matter particles as well as any realistic galaxy populations.

Wu et al. (2013) review the current consensus on velocity bias in simulated halos. As measured by the velocity dispersion, Wu et al. (2013) find that sub-halos typically show 10-15% positive biases (see also Lau et al., 2010). This is a manifestation of how the radius/velocity phase-space is sampled by the resolved sub-halos. One can draw from the phase-space in any number of ways, any of which may show positive or negative biases compared to the full representation of the phase-space by the particles. In the case of sub-halos, they can easily be destroyed through interactions causing a paucity of tracers with low velocities. The end result is a sub-halo velocity dispersion that is biased with respect to the particles. Therefore, we must test whether the edge

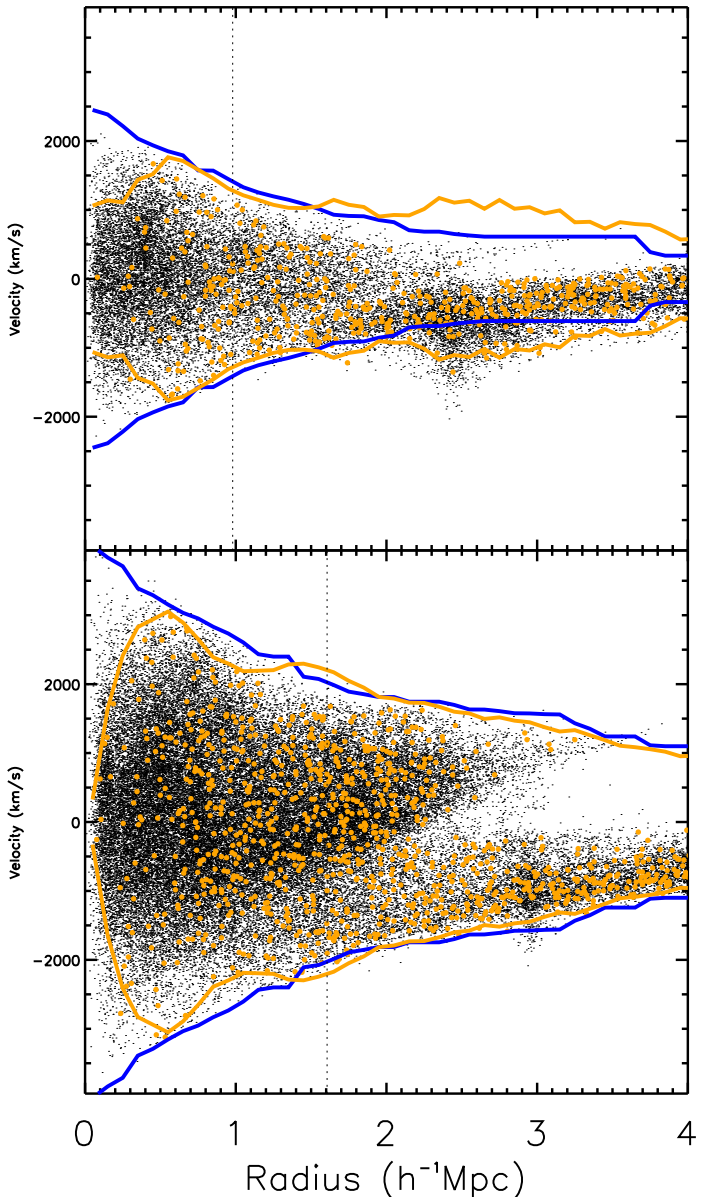

Figure 3.1: The radius-velocity phase spaces of a low mass (top- $2.4 \times 10^{14} M_{\odot}$) and high mass (bottom- $1.0 \times 10^{15} M_{\odot}$) cluster in the Millennium simulation. The dots are particle radial positions and radial velocities. The orange circles are sub-halo radial positions and radial velocities. The lines are the measured escape edges for the particles (blue) or the sub-halos (orange). Notice the increasing statistical bias in the sub-halo edges compared to the dark matter edges towards the core where the sampling is low. The dotted vertical bar is the location of r_{200}.

is prone to velocity bias by measuring the surface directly rather than identifying it based on velocity dispersion calibration techniques (Diaferio, 1999; Serra et al., 2011).

First, we need to separate systematic velocity biases (i.e., along the vertical axis of the phase-space diagrams) from statistical sampling biases (i.e., along the horizontal axis). While most of our halos have thousands of particles in each radial bin of the phase-space, there are only tens of sub-halos in any bin. This can cause a sampling bias as a function of radius due to the small number of objects per bin. This bias is purely statistical and is visible in Figure 3.1. We can determine the level of this bias by sub-sampling from the particles to match the number of sub-halos. We use 100 uniformly random sub-samples of the particles per bin per cluster. We then calculate the difference between the sub-sampled edge and the full particle edge. Not surprisingly, we find a statistical sampling bias that gets worse as we move into the core of the clusters and the sub-halo density relative to the particle density decreases. We calculate the radial difference between the full and sub-sampled edges with respect to the particle edge as determined beyond $r_{200} = 3h^{-1}$Mpc, well beyond the radius where sub-halo interactions are common. We then apply this statistical sampling correction to the measured sub-halo escape edges. We note that the sampling bias results in an escape edge that is biased low and in the opposite direction of the halo bias reported in Lau et al. (2010), Wu et al. (2013), and what we find in Chapter II.

In Figure 3.2, we show the sampling corrected sub-halo velocity dispersion and edge bias determined as the fractional difference from the particles. To ensure a fair comparison to the velocity dispersion, we apply the same sampling correction procedure as we did for the escape edges. Notice that the velocity dispersion profile shows positive biases $\sim 15\%$, identical to what is presented in Chapter II. However, the escape-edge based on the sub-halos is unbiased beyond ~ 0.4 h^{-1}Mpc to at least $\sim 2\times r_{200}$.

The fact that the sub-halo edge is unbiased is an important result. The edge is

a well-defined and sharp feature of the phase-spaces of halos in simulations and so long as the sampling is high enough, the edge will be detected regardless of how the sampling is done. Gravity insists that there can be no population of tracers which exist above the escape edge. We note that there can be sub-halos which momentarily live above the edge while they are escaping (see the top panel of Figure 3.1), but these are rare and fleeting and do not systematically bias the edges for all halos over all radii.

3.3 Caustic Theory

Consider a mass distribution described by an NFW profile such that the mass density ρ and the potential Φ radial profiles are:

$$\begin{aligned} \rho(r) &= \frac{\rho_0}{(r/r_0)(1+r/r_0)^2} \\ \Phi(r) &= -\frac{4\pi G\rho_0 (r_0)^2 \ln(1+r/r_0)}{r/r_0} \end{aligned} \tag{3.2}$$

where ρ_0 is the normalization and r_0 is the NFW scale radius. This is an example of a density - potential *pair* which share the same values for the shape parameters ρ_0 and r_0 and are related via the Poisson equation, $\nabla^2\Phi(r) = 4\pi G\rho(r)$. We can write the NFW-inferred spherical mass differential as:

$$\begin{aligned} \frac{dm}{dr} &= 4\pi\rho(r)r^2 \\ G\frac{dm}{dr} &= -\Phi(r)\left(\frac{(r/r_0)^2}{(1+r/r_0)^2\ln(1+r/r_0)}\right) \end{aligned} \tag{3.3}$$

where the unknowns are the gravitational potential $\Phi(r)$ and the scale r_0. This is a key step in our escape velocity technique, where we have equated the parameter ρ_0 in equations 3.2. The NFW parameter ρ_0 sets the absolute scale for the mass density. The other NFW parameter r_0 defines the scale radius and is observable in projected

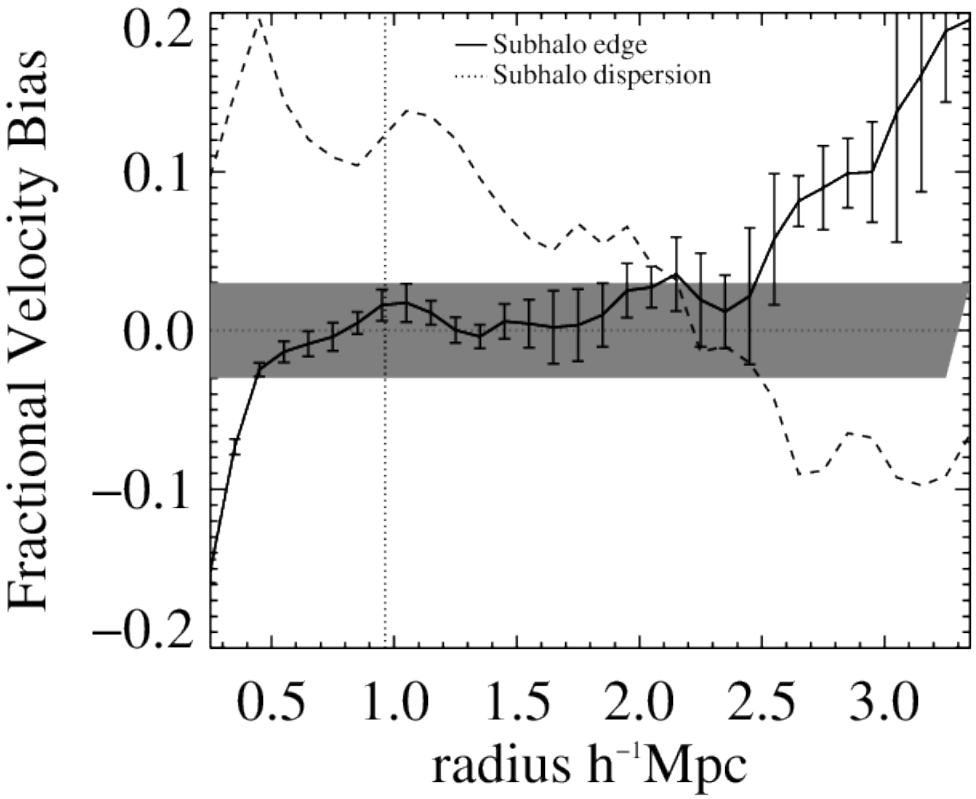

Figure 3.2: The fractional sub-halo velocity bias profile with respect to the particles for the velocity dispersion and the edge. In both cases, we remove the statistical bias with results from the low sampling of the sub-halo population. While the sub-halos have a biased velocity dispersion with respect to the dark matter particles, the escape edge is well-constrained by the sub-halos. The vertical line is the average r_{200} for the sample. The gray band represents the $\pm 3\%$ scatter on how well the density-inferred potential predicts the measured escape edge from the particles (see §1.3.2.

data.

We use equation 3.1 to re-write equation 3.3 as:

$$GM(< R) = \int_0^R \hat{\mathcal{F}}(r) v_{esc}^2(r) dr \tag{3.4}$$

where

$$\hat{\mathcal{F}}(r) = \frac{(r/r_0)^2}{(1 + r/r_0)^2 \ln(1 + r/r_0)} \tag{3.5}$$

where the unknowns are the scale radius r_0 and the escape velocity $v_{esc}^2(r)$, which is measured from the extrema in the radius and velocity $(r - v)$ phase-space data.

More precisely, our estimate $\hat{\mathcal{F}}(r)$ should actually be:

$$\mathcal{F}(r) = -2\pi G \frac{\rho(r) r^2}{\Phi(r)} \tag{3.6}$$

where $\rho(r)$ and $\Phi(r)$ are the spherically averaged density and potential profiles (see Diaferio & Geller (1997) or Chapter II). The difference between $\mathcal{F}(r)$ and $\hat{\mathcal{F}}(r)$ is that the former uses an exact profile for the densities and the potentials, while the latter assumes that only the density profile can be measured and that the potential has the same NFW shape parameters (i.e., concentration and scale) as the density. We discuss whether or not this NFW-shape assumption holds in Section 3.4.1.

In projected data, we measure the velocities along the line-of-sight (l.o.s.), and so

$$\langle v_{esc,los}^2 \rangle(r) = \frac{(1 - \beta(r))}{(3 - 2\beta(r))} \langle v_{esc}^2 \rangle(r) = (g(\beta(r)))^{-1} \langle v_{esc}^2 \rangle(r) \tag{3.7}$$

where the β is the standard velocity anisotropy parameter.

In the classical implementation of the caustic technique, the average $\mathcal{F}_\beta = \langle g(\beta(r)) \mathcal{F}(r) \rangle$ is measured within N-body simulations, and then applied to real data (Rines et al., 2013; Geller et al., 2013). In the literature, $0.5 < \mathcal{F}_\beta < 0.7$ (Diaferio & Geller, 1997;

Diaferio, 1999; Serra et al., 2011; Svensmark et al., 2015). Since $\mathcal{F}_\beta$ enters into the equation as being directly proportional to the mass, we must know it to high accuracy if escape velocity masses are to be used in cosmological analyses.

A goal of this chapter is to drop the requirement that $\mathcal{F}_\beta$ be calibrated from simulations. We assume that clusters are NFW density-potential *pairs* and apply equation 3.4 directly. The unknowns, r_0 and $\langle v^2_{esc,los}\rangle$ and β are constrained from observed data (Lin et al., 2004; Carlberg et al., 1997a; Wojtak & Łokas, 2010; Budzynski et al., 2012; Diaferio & Geller, 1997; Geller et al., 2013; Rines et al., 2013; Lemze et al., 2009; Biviano & Poggianti, 2009; Host et al., 2009).

A final calibration in standard escape-velocity technique is that of the iso-density surface in $r-v$ space which defines the average escape velocity, $\langle v^2_{esc}\rangle(r)$. The density-weighted average escape velocity inside radius R is:

$$\langle v^2_{esc}(<R)\rangle = \frac{\int_0^R d^3\mathbf{x}\rho(\mathbf{x})v^2_{esc}(\mathbf{x})}{\int_0^R d^3\mathbf{x}\rho(\mathbf{x})} = -2\frac{\int_0^R d^3\mathbf{x}\rho(\mathbf{x})\Phi(\mathbf{x})}{M(<R)} \tag{3.8}$$

where we have used equation 3.1. The integral in the numerator on the right-hand side of equation 3.8 is twice the total potential energy of the system or $2W$ (Binney & Tremaine, 1987), which leads to:

$$\langle v^2_{esc}\rangle = -\frac{4W(<R)}{M(<R)} \tag{3.9}$$

where W and M are the total potential energy and mass of the system within the radius R.

One often defines the following relation between the fraction of the total kinetic over the potential energy to that expected from a virialized halo:

$$b = 1 + \frac{2\mathrm{T}}{\mathrm{W}} \tag{3.10}$$

where T is the total kinetic energy. If we express the total kinetic energy of the system as $T = 1/2M\langle v^2 \rangle$ equation 3.9 becomes:

$$\langle v^2_{esc}(< R)\rangle = -\frac{4\langle v^2(< R)\rangle}{b-1} \tag{3.11}$$

where the average quantities are measured within the same radius, R. The standard calibration assumes that $\langle b \rangle = 0$ in a virialized and isolated halo such that $2T = -W$. Thus $\langle v^2_{esc} \rangle = 4\langle v^2 \rangle$, such that the escape velocity phase-space surface is calibrated through a measurement of the velocity dispersion.

In this section, we have clarified where the calibration steps enter into the standard caustic analysis. The calibration includes the term $\mathcal{F}_\beta$, which is directly proportional to the estimate of the mass. This term comprises two parts: $\mathcal{F}(r)$ in Equation 3.6 and $g(\beta(r))$ in Equation 3.7. The other calibration step occurs from $\langle b \rangle$ in Equation 3.11, which decides the iso-density contour in the $r - v$ phase-space that defines the escape velocity. We have also presented a derivation of the caustic technique which does not require a calibration of $\mathcal{F}_\beta$, but which assumes an NFW density-potential pair and uses the observables in Equation 3.4.

3.4 Testing the Theory

We apply the caustic technique to 100 Millennium halos with masses $M_{200} > 1\times10^{14}\mathrm{M}_\odot\mathrm{h}^{-1}$ and $z < 0.1$ where $h = H_0/100\,\mathrm{km\,s^{-1}Mpc^{-1}}$. In 3D we use the particle postions and velocities. In the projected analyses we use the Guo et al. (2011) semi-analytic galaxies within $30\mathrm{h}^{-1}$Mpc of the halo centers projected along a random line-of-sight. These volumes are large enough to incorporate realistic projection effects. The limits on the projected phase-space velocities are $\pm$3000km/s relative to the halo velocity centroids, whereas the typical escape velocities are $\sim$ 1500km/s.

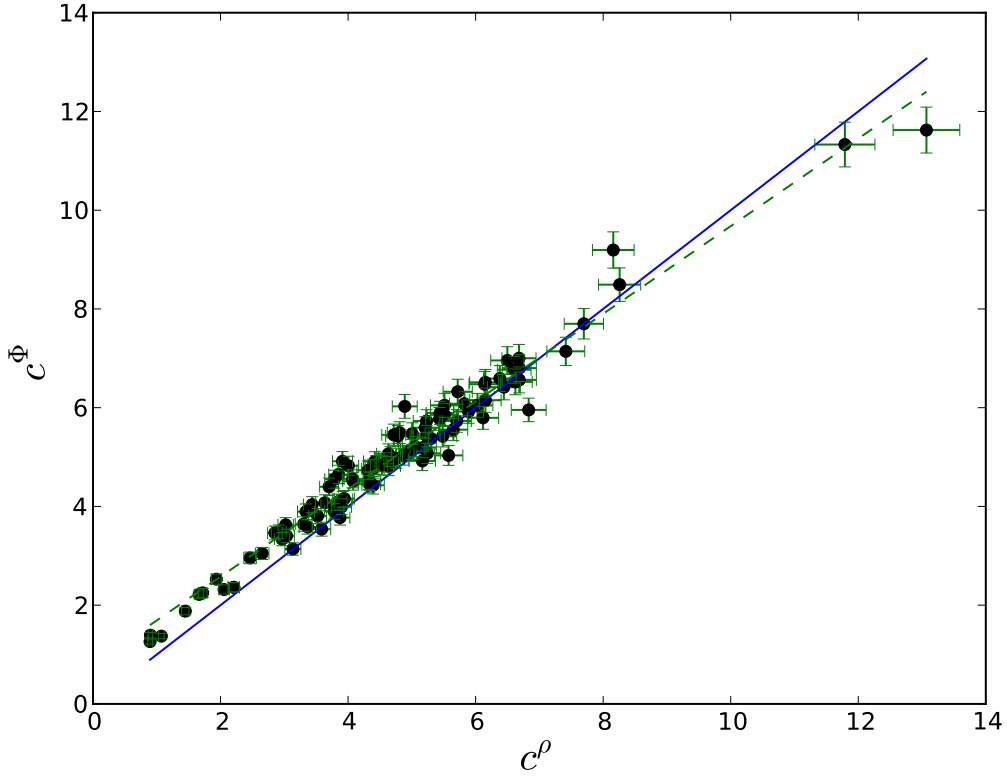

Figure 3.3: A comparison of the concentration measured via the density profile with $c^{\rho} = r_{200}/r_0^{\rho}$ and the concentration measured via the potential profile with $c^{\Phi} = r_{200}/r_0^{\Phi}$. The blue line is unity and the green dashed line is the fit to the relationship with a slope = 0.89 intercept = 0.80.

3.4.1 The NFW shapes

In order to drop the N-body calibration of $\mathcal{F}_\beta$, we assume that the NFW densities and potentials have the same parameters. This is expected if the matter distribution is concentric with the iso-potential surfaces (e.g., as in spherical symmetry; see also the classical potential solutions for homogeneous density distributions in Chandrasekhar (1969) and Binney & Tremaine (1987)). However, Conway (2000) provide exact closed-form Newtonian potential solutions to an infinite family of heterogeneous spheroids and find that the densities are generally not constant on the iso-potential bounding surfaces. In other words, while both the potential and density distribution could have the same general functional form like an NFW, they need not have identical shape parameters.

We compare the NFW density/potential shapes by first fitting the NFW density profile and determining ρ_0 and r_0 for each halo. The gravitational potentials are measured exactly through summation of $\frac{Gm_i}{\mathbf{r_i}}$ and then fit with an NFW using ρ_0 measured from the density, but allowing the potential scale parameter r_0 to be a free parameter.

In Figure 3.3, we compare the NFW concentrations $c^{\rho,\Phi} = r_{200}/r_0^{\rho,\Phi}$, where r_{200} is the radius which contains a density corresponding to 200$\times$ the critical density. We find that the potentials have slightly higher concentrations than the densities. This difference suggests that our systems are not density-potential pairs which are simply related via spherical solutions to the Poisson equation. Because of this, we expect that using equation 3.4 will return an incorrect mass estimate due to its assumption of shape similarity in the density and potential profiles.

In Figure 3.4 we compare the 3D escape velocity masses with halo masses within r_{200} (M_{200}). In the top left panel, we use the exact densities and potentials as measured using the particles (e.g., Equation 3.6). These caustic mass estimates are nearly unbiased with a scatter of 13%. In the top right panel of Figure 3.4 we utilize equa-

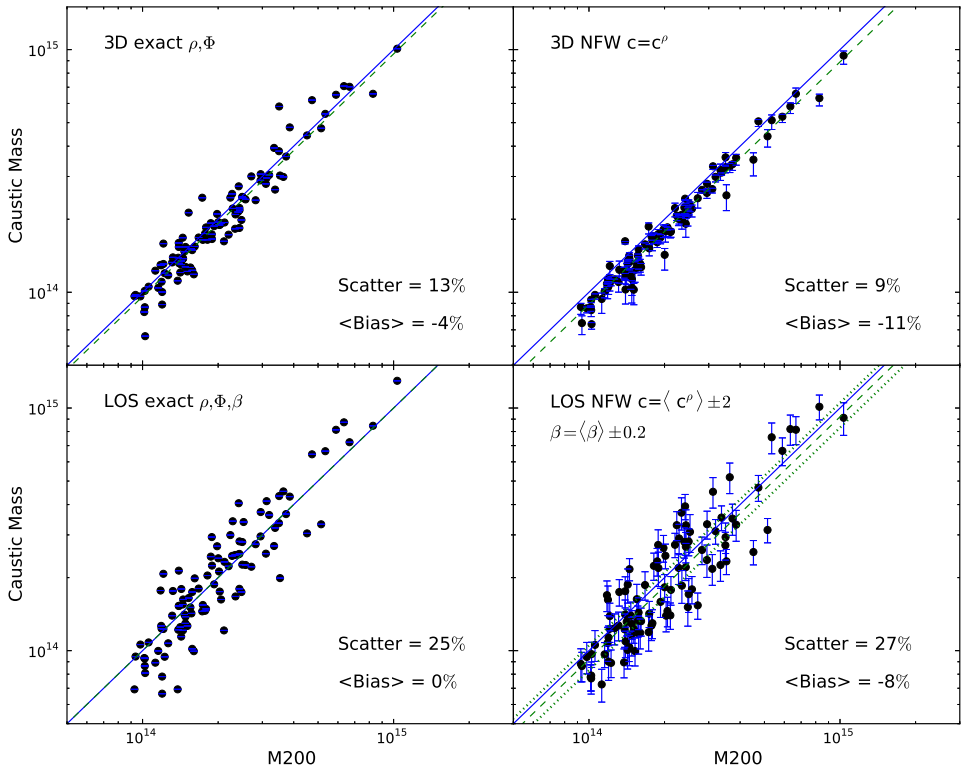

Figure 3.4: **Top Left:** M_{200} vs the 3D caustic mass estimated inside r_{200} calculated using the exact potential and density profiles (see equation 3.6). **Top Right:** Caustic masses using NFW fits to the 3D density profiles (equation 3.4). The induced bias is expected from Figure 3.3. In all panels the solid blue line is unity and the green dashed line represents the average bias of the sample with slope unity. **Bottom Left:** M_{200} vs the line-of-sight caustic mass estimated inside a projected r_{200}. As in the top panel, we use the particle potential and density profiles, but now include the particle anisotropy profiles as well. The increased scatter is due to the line-of-sight projections which induce scatter into the velocity dispersions. **Bottom Right:** Projected caustic masses based on an NFW density profile with a single sample concentration of $\langle c \rangle = 5 \pm 2$ and a single sample $\langle \beta \rangle = 0.2 \pm 0.2$. These large uncertainties do not add appeciably to the scatter induced by the line-of-sight projection effects. Mass biases induced by systematic errors in β are shown by the two dotted lines $\langle \beta \rangle = 0.0$ (lower) or $\langle \beta \rangle = 0.4$ (upper).

tion 3.4, where only the density profile is used to fit the 3D NFW concentrations and their errors. As expected from Figure 3.3 the NFW-inferred 3D caustic masses are biased low by $\sim 10\%$. The scatter is 8%. The errors on this panel use a conservative uncertainty in $c = 50\%$. A large uncertainty in the concentration has little effect on the scatter of the actual caustic mass estimate. This will become important when we discuss realistic observational biases and scatters in section 3.3.

3.4.2 Virialization

It has been shown that the virial relation $2T = -W$ is often not met in simulated halos (Shaw et al., 2006; Bett et al., 2007; Neto et al., 2007; Davis et al., 2011). This does not mean that the system is not virialized, but simply that more terms from the tensor virial equation are required, usually in a surface pressure kinetic term. So the question then is at what radius do we begin to see a bias expected from equation 3.11 when $\langle b \rangle \neq 0$?

To test this, we measure the exact (unbiased) caustic masses using $\mathcal{F}(r)$ at 1, 0.9, 0.7, and 0.5 $\times$ the virial radius. We detect no appreciable bias until we reach half a virial radius where the masses become biased low by 10%. We calculate $\langle b \rangle = 0.1$ for particles within this radius. We then apply $\langle b \rangle = 0.1$ during the virial calibration stage of the caustic technique and find no mass bias. Serra et al. (2011) conduct a similar test, but against various fractions of their membership radius R_{Tree}, as opposed to an intrinsic cluster property like R_{200}. They find that there is a preferred radius of of $0.7\times\mathrm{R}_{Tree}$. We come to a slightly different conclusion: that the choice of radius does not matter, so long as the correct $\langle b \rangle$ is used. We also find that there is no bias when caustic masses are calibrated using data within $0.7 \leq R \leq 1 r_{200}$.

3.4.3 Velocity Anisotropy

When the data are projected along the line-of-sight, velocity anisotropies in the orbits of the galaxies must be taken into account (Diaferio & Geller, 1997). In the bottom left panel of Figure 3.4, we use $\mathcal{F}_\beta(r)$ which is the exact $\mathcal{F}(r)$ profile multiplied by the exact $\beta(r)$ profile. The increase in the scatter from the 3D ($\sim 10\%$) case to the line-of-sight ($\sim 25\%$) case is identical to what we measure in Chapter II using the classical caustic technique and a constant $\mathcal{F}_\beta$. Therefore, for any given cluster, there is no gain in accuracy or precision in the estimated caustic masses by measuring a $\beta(r)$ profile for each cluster. The scatter is dominated by line-of-sight variations in the projected velocity dispersion (see Chapter II).

We show our most realistic comparison of the caustic masses to M_{200} in the bottom-right panel of Figure 3.4. Here we drop explicit knowledge of the concentrations and apply the ensemble average $\langle c \rangle = 5 \pm 2$ for every halo in $\hat{\mathcal{F}}(r)$ (see Figure 3.3). We also drop explicit knowledge of the anisotropy profile and instead use $\langle \beta \rangle = 0.2 \pm 0.2$ which is the average β for these halos. Using these estimates, we find that the scatter is only slightly higher than in Figure 3.4 (bottom left). Large uncertainties in the average anisotropy and concentrations do not appreciably add scatter to what is already there from the line-of-sight projection. The bias in Figure 3.4 bottom-right is caused by the faulty assumption that the halos have the same NFW density and potential concentrations (see Figure 3.3).

Systematic errors in the observable ensemble averages for the concentrations and the velocity anisotropies do impart mass biases. When we impose $\langle \beta \rangle = 0.0 \pm 0.2$ the average bias changes from -10% to -18% while $\langle \beta \rangle = 0.4 \pm 0.2$ results in an average mass bias of +5%. When we impose $\langle c \rangle = 3 \pm 0.1$ the bias changes from -8% to -13% while $\langle c \rangle = 6 \pm 2$ results in a mass bias of -7%. These average concentration values cover the full range of observational estimates in the literature (Carlberg et al., 1997a; Lin et al., 2004; Wojtak & Łokas, 2010; Budzynski et al., 2012).

3.5 Conclusions

One goal for this work was to test the fundamental statistical and systematic precision of the escape velocity (or caustic) technique to measure masses of cluster-sized halos in N-body simulations. Given the 3D data, caustic masses are unbiased with 10-15% precision (similar or better to the virial scaling relation of Evrard et al. 2008). The scatter increases to 25% as a result of line-of-sight projections.

Our second goal was to re-frame the theory in terms of observable quantities and remove calibrations to N-body simulations. We utilized the weak assumption that the observed density and potential profiles can be described by an NFW with the same shape parameters, specifically the scale parameter r_0. We find that this latter assumption does not hold in the Millennium Simulation data, and the inferred cluster masses are biased low by $\sim 10\%$. The virial calibration can also contribute to biases in the caustic masses when the velocity dispersion is averaged over a radius where the total binding energy is not represented by virial expectations. We show that large uncertainties in the ensemble average of the velocity anisotropies and concentrations do not contribute significantly to the intrinsic line-of-sight scatter in projected caustic masses. However, large (e.g. 100%) systematic errors in the average velocity anisotropies and concentrations can lead to additional 5-10% biases in the caustic masses.

CHAPTER IV

Correcting Statistical Biases in Mass Estimation Through Stacking Techniques

4.1 Introduction

Galaxy clusters continue to play a prominent role in our desire for precision cosmological measurements. Clusters inform us about cosmology through their abundance and spatial clustering, both of which are sensitive probes of the universe's matter density and the growth of structure due to gravity. Precision cosmological inference using clusters is only possible when we measure their characteristics as a function of mass (Vikhlinin et al., 2009; Rozo et al., 2010).

Cluster mass cannot be directly measured, but its presence is visible through the gravitational potential, which can be quantified using the lensing of background galaxies (weak or strong), via the surface brightness and temperature of the intracluster medium to infer gas mass in hydrostatic equilibrium, through the maximum escape velocity surface traced by phase-spaces of the cluster galaxies, as well as through the Jean's equation (Diaferio & Geller, 1997; Meneghetti et al., 2010b; Carlberg et al., 1997a; Hoekstra et al., 2015). There are also indirect cluster mass estimation techniques, such as the X-ray gas temperature or luminosity, the SZ decrement from the scattering of the background CMB photons, the velocity dispersion, and cluster

richnesses (Evrard et al., 2008; Andreon & Hurn, 2010; Planck Collaboration, 2011).

There is ongoing research to understand and control statistical and systematic uncertainties in the techniques of cluster mass inference using direct measures of the potential. Direct measurement of cluster potentials often requires a significant amount of data per cluster, whether it is the number of background galaxies for weak lensing shear profiles, X-ray photons for gas mass profiles, or spectroscopic galaxies for radius-velocity phase-space analyses. There are numerous studies which utilize simulations of idealized data sets to characterize statistical and systematic errors in direct potential measurements of individual clusters (Becker & Kravtsov, 2011; Gruen et al., 2015; Rasia et al., 2006; Meneghetti et al., 2010b; Serra et al., 2011; Geller et al., 2013; Hoekstra et al., 2015). Another way to constrain uncertainties is to compare two different measures of the potential (*e.g.,* Geller et al., 2013; Hoekstra et al., 2015).

In reality, the quantity and quality of data quickly becomes prohibitively expensive for large samples of clusters or for faint and small clusters (e.g., low mass and/or distant). To counter the lack of data, stacking is often employed as a way to raise the signal-to-noise for an ensemble of clusters. Stacking also has the benefit of homogenizing the projected shapes in order to reduce the bias from spherically-fit profiles to non-spherical systems.

However, stacking can just as easily induce new systematic biases. For example, Biesiadzinski et al. (2012) showed how the stacked SZ signal can have significant systematic biases if the optical cluster sample selection is not correctly characterized. Becker et al. (2007) used the pairwise velocity dispersion (a form of stacking) to quantify the scatter in the dispersion at fixed richness for clusters in the Sloan Digital Sky Survey data and in simulations. They recognize that the resulting stacked dispersion must be treated as non-gaussian to avoid biases in the result. Other recent studies examine how accurately stacked ensembles can infer the potential through the

Jean's equation, as well as the presence of cluster shape-induced biases using both phase-space and weak lensing observables (Svensmark et al., 2015; Dietrich et al., 2014)

Here, we study how to conduct a stacked analysis using cluster projected phase-spaces and the caustic technique to infer the escape velocity masses (Diaferio & Geller, 1997; Diaferio, 1999). Merging individual phase-spaces into an ensemble cluster increases the signal-to-noise of the caustic feature used to estimate the mass profile. This work extends upon Svensmark et al. (2015), who used particle data in simulations to constrain the minimum and maximum caustic mass biases caused by line-of-sight projections of the cluster phase-spaces. The Svensmark et al. (2015) result is related to what was found by Dietrich et al. (2014), who used weak lensing stacking and incorporated realistic cluster selection on galaxy catalogs. In both cases, cluster shape is shown to play an important role in cluster mass estimation. What have yet to be fully investigated are the baseline accuracy of the caustic technique on stacked phase spaces, how to build ensemble clusters, and the effects of mass scatter in the binning process.

The caustic technique has been applied to stacked systems in observations before. Biviano & Girardi (2003) stacked 43 poorly sampled clusters with galaxies out to $2r_{\rm vir}$ and used both the caustic technique as well as a Jeans analysis to recover an average mass profile and found good agreement between the two methods. Rines et al. (2003) created an ensemble cluster based on nine clusters in the CAIRNS survey. Unlike other studies, each of the included systems was sampled well enough to obtain individual measurement of velocity dispersion and M_{200}. They chose to scale their velocities by each system's velocity dispersion before stacking, and doing so, found agreement to within 1σ of the theoretical expectation of $M_{200} = 3\sigma^2 r_{200}/G$.

Our focus in this paper is to test the caustic technique's ability to recover the average stacked ensemble mass and the average ensemble uncertainty for different

stacking strategies. We pay particular attention to the stacking algorithms, and we use realistic simulated galaxy data with projection effects that mimic what is seen in the local universe ($z \sim 0.1$). We test whether the process of stacking induces an intrinsic bias by developing a new self-stacking technique (§4.4.1). Once the algorithm is verified, we build ensemble clusters to study how sampling rates affect the accuracy and precision of the stacked cluster masses (§4.4.2). Finally, we use a mass-observable relation to incorporate correlated scatter into our ensemble clusters and we measure the resultant biases from mass mixing across the bin boundaries (§4.4.3).

4.2 Simulation and Semi-Analytic Catalog

In this study, we utilize the Guo et al. (2011) semi-analytic galaxy catalog and the Millennium Simulation (Springel et al., 2005). Semi-analytic galaxy catalogs are built using a set of "rules" for evolving galaxies inside identified subhalos in an N-body simulation. Subhalos are defined and located using algorithms such as SUBFIND (Springel et al., 2001) which have been shown to work well to identify all of the sub-structure in N-body simulations (see also Knebe et al., 2011). The semi-analytic model captures the history of position, velocity, size, and merger history of these subhalos and applies its rule set to transform these properties into galaxy mass, circular velocity, accretion rate, and other physical parameters that can, in theory, be observed. Semi-analytic galaxy catalogs can be compared with observed luminosity functions of galaxies to judge their success.

The Millennium Database contains four different semi-analytic catalogs. One way the catalogs differ is in the way they treat "orphan" galaxies, or semi-analytic galaxies whose host subhalo was destroyed in the simulation. Orphan galaxy treatment is necessary since subhalos are too easily destroyed in N-body simulations due to limited resolution. To combat this, once a subhalo is destroyed, the semi-analytic galaxy lives on for a time following the most bound particle of the destroyed subhalo. Dynamical

friction arguments are applied to determine the time the orphan galaxy exists in the simulation. In Chapter II, we study these semi-analytic catalogs and find the cluster velocity dispersion and mass estimates in the Guo catalog to be near the average of the catalogs and unbiased using a set of assumptions for mass estimation.

In sections 4.4.1 and 4.4.1.1 our sample contains 20 clusters from the Guo semi-analytic catalog at redshift = 0 for which we have 3-dimensional position and velocity information. These clusters are located within the central $50 \times 50 \times 50h^{-1}$ Mpc of the $500h^{-1}$ Mpc per side simulation box. This allows for long lines-of-sight to each system of at least $200h^{-1}$ Mpc. Long lines-of-sight are necessary to build phase spaces with similar projected interloper properties of clusters at low redshift.

The remaining sections utilize the Henriques all-sky light cone (Henriques et al., 2012; Guo et al., 2011) to study stacking independent clusters. This sample consists of 6100 clusters that span a mass range of $7.2 \times 10^{13} - 2.1 \times 10^{15} h^{-1} M_{\odot}$. The redshift range is selected to be between $0.0 - 0.15$ to mimic shallow-wide surveys. This large sample allows us to test for systematics over a large cluster mass range. In all our analyses, we assume a flat ΛCDM cosmology matching the Millennium values with $\Omega_{\rm M} = 0.25$, $\Omega_{\Lambda} = 0.75$, and $H = 100h$ km s^{-1} Mpc^{-1}.

4.3 The Caustic Technique

Under Newtonian dynamics, the escape velocity of a spherically symmetric cluster relates to its gravitational potential by

$$v_{esc}^2(R) = -2\Phi(R), \tag{4.1}$$

where R is the 3-dimensional measured distance to the center of the cluster. If the dynamics of the system are controlled by the gravitational potential, galaxies which cannot escape the potential exist in a well-defined region of radius/velocity $(R - v)$

phase space. The extrema of the velocities in this phase space define an edge, the escape velocity profile $v_{esc}(R)$, which can also be observed directly with 3 dimensional position and velocity information, or estimated using projected sky coordinates and line-of-sight velocities as $v_{esc}(r)$. Given the observed $v_{esc}(r)$, the escape velocity or "caustic" technique allows one to infer the mass profile of a cluster to well beyond the virial radius (Diaferio & Geller, 1997). Once the escape velocity surface is identified, the equation

$$GM(<r) = \mathcal{F}_\beta \int_0^r v_{esc}^2(r')dr' \tag{4.2}$$

calculates the mass within the radius r where $v_{esc}^2(r)$ is the observed (projected) escape velocity profile and $\mathcal{F}_\beta$ is a function which depends on the density, the potential, and the projected anisotropy profile. It is usually approximated as a constant and calibrated through simulations.

4.3.1 Calibrating the Caustic Masses

In Chapter II we quantify how well the average calibration constant, $\mathcal{F}_\beta$, can be determined for individual systems. These calibrations involve choosing the correct "surface" to prescribe as tracing the projected escape velocity and in defining a value for $\mathcal{F}_\beta$. As discussed in detail in Diaferio (1999), the constant $\mathcal{F}_\beta$ is derived as a function of the dark matter density and potential profiles, as well as the galaxies' velocity anisotropy profile $\beta(r) = 1 - (v_\theta^2 + v_\phi^2)/v_r^2$. Analytically, $\mathcal{F}_\beta(r)$ is expressed as:

$$\mathcal{F}_\beta(r) = \frac{-2\pi G\rho(r)r^2}{\Phi(r)} \frac{3 - 2\beta(r)}{1 - \beta(r)}. \tag{4.3}$$

Considering that the density profiles of halos and clusters are known to follow the functional form defined by Navarro et al. (1997), we can reduce equation 4.3 to

$$\mathcal{F}_\beta(r) = \frac{c^2 s^2}{2\ln(1+cs)(1+cs)^2} \frac{3 - 2\beta(r)}{1 - \beta(r)}, \tag{4.4}$$

where $s = r/r_{200}$ and $c = r_{200}/r_s$ such that r_s is the NFW scale radius. Diaferio (1999) and Serra et al. (2011) approximate this function as a constant out to 2-3$\times$r$_{200}$, noting that its value varies slowly with radius. When defined as a constant over some range in radius, $\mathcal{F}_\beta$ acts as a caustic mass calibrator, which depends weakly on variations in concentration and the radially averaged velocity anisotropy β.

There is some debate in the literature about the value of $\mathcal{F}_\beta$, with values ranging from 0.5 - 0.7 (Diaferio, 1999; Serra et al., 2011; Svensmark et al., 2015). As shown in Chapter III and Diaferio (1999), large variations in concentration and β lead to small variations in the $\mathcal{F}_\beta$ and caustic masses, so these are not the source of the wide range in accepted $\mathcal{F}_\beta$ values. Instead, in Chapter II we show that the differences can mostly be attributed to the use of different dynamical tracers (i.e., velocity bias), which enters into the technique when the surface is determined, i.e., equation 4.2, which is derived by requiring equation 4.1.

All caustic analyses on clusters utilize a surface calibration based on Binney & Tremaine (1987), who show that

$$\langle v_{esc}^2 \rangle = \frac{-4W}{M} \tag{4.5}$$

where M and W are the total mass and potential energy of the system respectively. If the system is in virial equilibrium, $-W = 2K$, where the total kinetic energy $K = 1/2M\langle v^2 \rangle$, then we can identify the escape velocity profile by choosing the iso-density contour in phase-space that satisfies the equation

$$\langle v_{esc}^2 \rangle - 4\langle v^2 \rangle = 0. \tag{4.6}$$

If $\langle v^2 \rangle$ is calculated using biased dynamical tracers, the inferred $v_{esc}(r)$ will also be biased. This can be compensated for by calibrating $\mathcal{F}_\beta$ to recover unbiased masses.

It is not necessary that $\mathcal{F}_\beta$ be treated as a free-parameter to calibrate unbiased

cluster masses against simulations (Alpaslan et al., 2012; Svensmark et al., 2015). Given a mass-concentration relation and assuming some value for the radially averaged anisotropy parameter β, one can calculate $\mathcal{F}_\beta$ from equation 4.3 or 4.4 directly. We do this and find a median value of $\mathcal{F}_\beta = 0.62 \pm 0.05$ within r_{200}. If instead we assume a Gamma distribution (Dehnen, 1993) we find a median value of $\mathcal{F}_\beta = 0.63 \pm 0.05$.

Serra et al. (2011) utilize numerically evaluated potentials, which they show are $\sim 10\%$ lower than the potentials expected from the NFW density profile via the Poisson equation. The challenge in this approach is to carefully match the potential in equations 4.3 or 4.4 to the escape surface. This is because equation 4.6 requires that the density and potential profiles be Poisson pairs (Binney & Tremaine, 1987). The $\sim 10\%$ difference between our value of $\mathcal{F}_\beta = 0.62$ and the value in Serra et al. (2011) of $\mathcal{F}_\beta = 0.7$ is explained through our use of a Poisson potential (with potential relative to infinity) and Serra et al. (2011) use of a numerical potential (with potential relative to 10Mpc), given that the average densities are the same. We have explored other possibilities such as radial and mass dependencies of $\mathcal{F}_\beta$ and find they account for differences of a few percent.

Taking all of these issues into account, we conclude that the literature values of $\mathcal{F}_\beta$ are quite consistent ($0.6 \leq \mathcal{F}_\beta \leq 0.65$) between techniques which utilize equations 4.3 or 4.4 (*e.g.,* Diaferio, 1999; Serra et al., 2011), and techniques which calibrate it to individual systems using ΛCDM simulations (*e.g.,* Svensmark et al., 2015).

In this work, we are creating stacked ensemble clusters and so we cannot calibrate $\mathcal{F}_\beta$ against individual clusters. We instead utilize equation 4.4. We use M_{200} and r_{200}, a concentration-mass relation from Merten et al. (2015), and we model the anisotropy as a constant inside r_{200} with $\beta = 0.30 \pm 0.15$ (Lemze et al., 2012; Mamon et al., 2013). Marginalizing over all uncertainties in c (Merten et al., 2015) and β results in a suite of $\mathcal{F}_\beta(r)$ profiles that can be radially averaged into the constant $\mathcal{F}_\beta = \int_0^r \mathcal{F}_\beta(x)dx/r$

per cluster. Our value of $\mathcal{F}_\beta = 0.62$ is close to the value estimated in both Chapter II and Svensmark et al. (2015), and agrees with Serra et al. (2011) when correcting their potentials by the 10% offset discussed above.

Another challenge when using stacked ensemble clusters and the caustic technique is in the surface calibration (e.g., equation 4.6.) As shown in Becker et al. (2007) and as we highlight below, the velocity dispersion of a stacked phase-space is a biased representation of the mean of the underlying velocity dispersion. Therefore in §4.3.2, we develop a new technique to calibrate the escape-velocity surface which leverages the high sampling of the stacked phase-spaces.

4.3.2 Estimating the Caustic Profile

The caustic technique is an estimate of the projected escape velocity profile such that the caustic profile $v_{esc}(r)$ and the potential profile $\Phi(r)$ (in the definition of $\mathcal{F}_\beta$) must be equal. As the name suggests, the caustic should be a sharp density drop-off in the cluster projected phase-space; however, with a sampling of even 100 galaxies inside the virial radius it is difficult to identify this edge by eye, let alone algorithmically.

This challenge has been overcome by identifying cluster members, measuring the cluster velocity dispersion, and using a virialization condition to calibrate the caustic surface based on a series of measured iso-density contours (Diaferio, 1999). This step makes caustic mass estimates of individual clusters possible without the need to visually identify a sharp edge in projection. The downside to the use of equation 4.6 is that we add an additional assumption to our methodology: that the cluster is in virial equilibrium inside the radius used to make the calibration.

There is a more fundamental reason why we should not use the velocity dispersion and an equilibrium assumption to calibrate the escape velocity profile when stacking. In velocity space, stacking is analogous to mixing semi-randomly sampled gaussians if

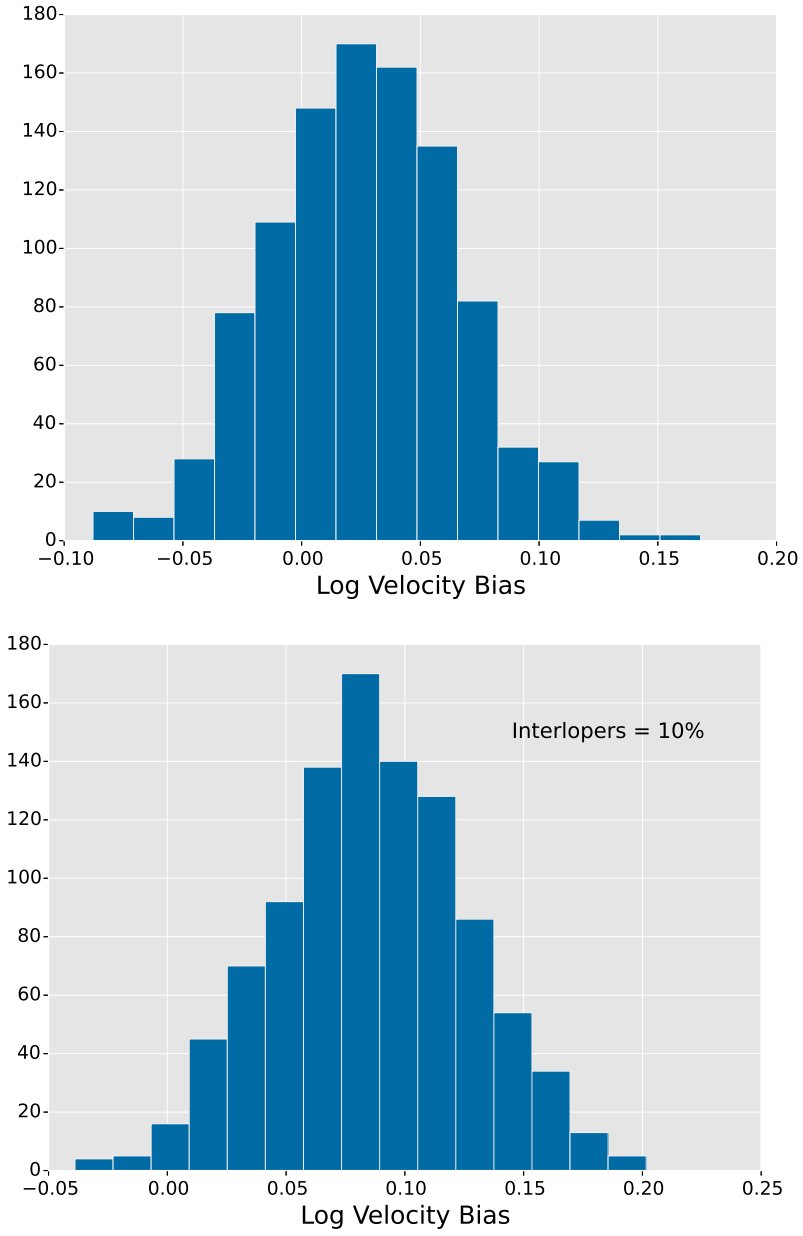

Figure 4.1: The expected log bias in velocity dispersion simulating 15 draws from 50 gaussians which themselves are randomly sampled from a log-normal distribution with a scatter of 20%. (Top) The resulting velocity bias compared with the median dispersion of the 50 input gaussians is $\sim 3-5\%$. (Bottom) If we assume 10% of the galaxies are instead drawn from a uniform distribution representing interlopers, the bias increases to $\sim 10\%$.

each cluster's velocity dispersion is approximately normal. On average, the resulting stacked distribution will have a velocity dispersion that is larger than the mean of the individual dispersions, or $\sigma_{\rm stack} > \langle\sigma_i\rangle$. We show this by simulating draws from mixed gaussian distributions and reporting the log difference between the dispersion of the sample and the average dispersion of the input gaussian population.

In Figure 4.1, we simulate the expected bias for typical observational values of 20% scatter in σ_i, 15 random samples per Gaussian, and 50 Gaussians per stack in 1000 experiments. The result is an expected velocity dispersion bias of 3-5% (top figure). This does not include a potential background interloper population uniformly distributed in velocity space that would work to increase this bias. Biviano et al. (2006) find an interloper fraction of 18-25% when using sigma-clipping techniques on randomly chosen dark matter particles; however, we expect our values to be lower given our more complex shifting-gapper approach which also utilizes magnitude information in Chapter II.

We re-quantify the velocity dispersion bias when 10% of the galaxies are drawn from a uniform background population in velocity space. We find that the bias increases to $\sim 10\%$. The translation from velocity bias to mass bias in the caustic technique is complicated and discussed further in §4.4.2.

Given the expected velocity bias in our ensemble clusters and our goal to remove the virial condition from the technique, we wish to eliminate the use of equation 4.6 altogether. We can do this through a direct identification of the caustic surface in highly sampled phase-spaces. Stacking allows us to overcome the lack of signal in the cluster projected phase-spaces and identify a caustic edge, despite projection blurring effects.

Using the radius/velocity phase-space, we identify iso-density surfaces based on medians of velocity percentiles in the radially binned velocity distributions using a mirrored phase-space. Interloper rejection is done in two phases. First, a shifting-

gapper algorithm is run to eliminate obvious outliers in the phase-spaces. However, because our phase-spaces are densely populated, we also make cuts in velocity based on smoothed phase-space density. In each radial bin, we make a cut in absolute velocity where the smoothed density reaches the estimated background density which differs from stack-to-stack. This usually occurs between 2-3$\times$ the velocity dispersion in each radial bin. Once we have removed potential interlopers, instead of using equation 4.6 we use the analytically calculated NFW potential profiles to identify the correct iso-density contour selected by velocity percentile. We find that the iso-density contour matched to the median of galaxies with velocities above the 90th percentile (within radial bins $< \langle r_{200} \rangle$ of the ensemble) recovers the mean NFW potential profile for each ensemble. This new surface calibration technique is independent of mass and sampling, at least for the systems in our data set. Most importantly, this algorithm ensures that our caustic surface matches the analytic potential, as required in equation 4.2.

In Figure 4.2, we show a stacked cluster projected phase-space from our simulations. The stack is built by sampling the top 50 brightest galaxies from the most massive 100 clusters in the sample. The red line shows the caustic edge selected using line-of-sight velocities above the 90th percentile of observed velocities across 6 radial bins within the $\langle r_{200} \rangle$ of this ensemble. This is compared with the analytically calculated $-2\Phi_{NFW}(r)$ (black line) using the average properties of the system. The blue band encompasses the 68% distribution of the individual caustic profiles estimated for each input cluster to the stack using the velocity dispersion to calibrate each caustic surface. Because these massive clusters have high sampling, the individual surfaces agree with the stacked surface within the scatter.

In §4.4, we test the ability of stacking to recover the average cluster mass in stacked ensemble phase-spaces by adjusting the number of galaxies per cluster and the number of clusters used in stacking. We will also study how the cluster binning

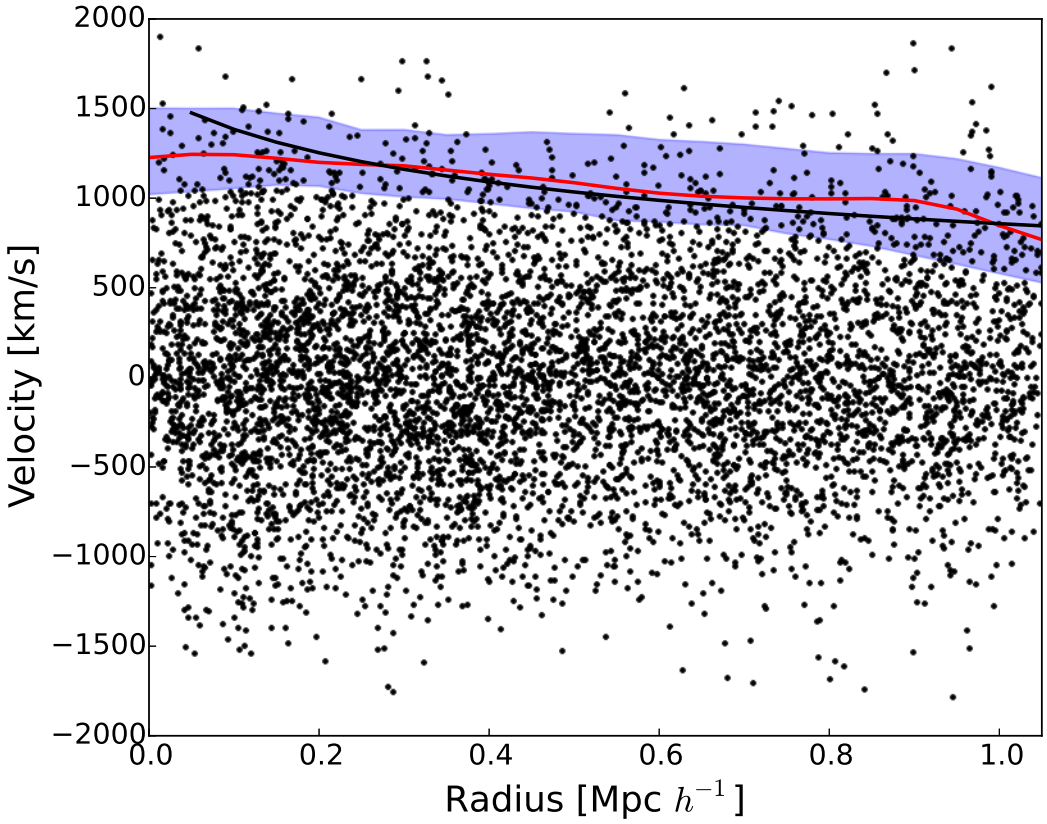

Figure 4.2: A stacked cluster projected phase-space of the top 50 brightest galaxies from the most massive 100 clusters in the sample. The black line is the analytical $-2\Phi_{NFW}$ using the average properties of the stack. The red line is the inferred caustic surface determined by matching the iso-density contour to the median of the radially binned line-of-sight velocities for those above the 90th percentile of galaxy velocities over 6 radial bins inside $\langle r_{200} \rangle$. The blue band contains 68% of the caustic surfaces estimated by each individual cluster in the stack.

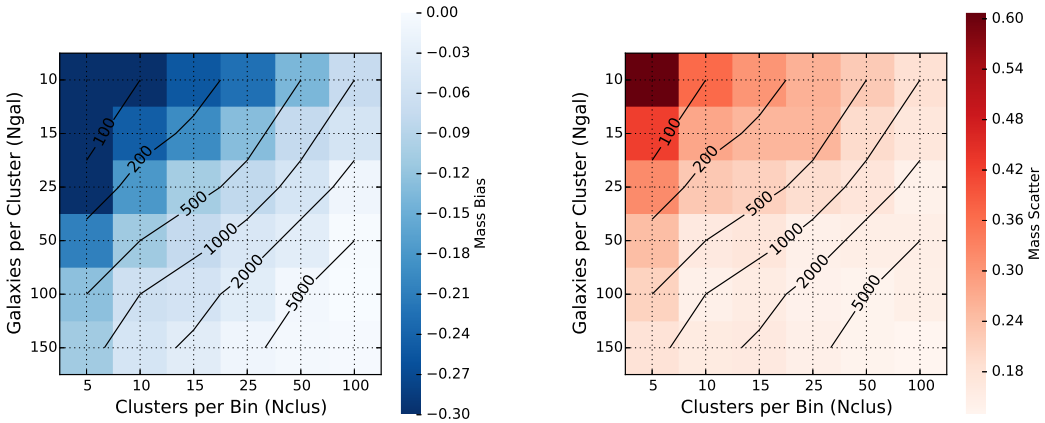

Figure 4.3: Left: We show caustic mass bias for self-stacked ensembles as a function of the number of random lines-of-sight to each cluster and the number of galaxies sampled from each line-of-sight. The labeled diagonal lines are contours of constant stacked phase-space richness N_{ens}. Right: The caustic mass scatter for self-stacked ensembles as a function of the number of random lines-of-sight to each cluster and the number of galaxies sampled from each line-of-sight.

procedure affects the stacked mass estimates.

4.4 Stacking Methods and Results

In sub-sections 4.4.1, 4.4.2, and 4.4.3 we investigate and quantify the overall systematic uncertainties when using stacking cluster projected phase-spaces and our revised caustic technique to estimate average masses. In §4.4.1 we introduce a way to stack single clusters in order to test the fundamental basis of our algorithm. We then introduce a small amount of mass-mixing to our stacking procedure in §4.4.2 by creating ensembles of clusters through binning directly on mass. Finally in §4.4.3, we build cluster ensembles using a mass proxy: the projected richness estimates of each cluster which has realistic scatter.

4.4.1 Self-stacking

Stacking cluster phase-spaces first requires a decision on how to "bin" or stack on cluster properties. Ideally, we first stack clusters of identical mass (and concentration) in order to eliminate the overall mass mixing in each bin. This allows us to test for any potential systematic biases in the technique itself. However, this task is difficult. Ideally, one needs multiple realizations (or re-simulations) of the same cosmology in order to achieve enough statistics without binning.

To solve this problem for our sample of clusters based in the Millennium Simulation, we devise a technique that stacks cluster projected phase-spaces with mass bins of infinitesimal width. This is achieved by stacking multiple lines-of-sight to one cluster in order to build a stacked phase-space. We term this technique self-stacking. The inferred stacked masses are then compared to a single well defined mass to identify biases in the technique.

4.4.1.1 Self-stacking Methods

Technically, self-stacking mimics stacking different individual systems. We treat each line-of-sight projection to a single cluster as a unique observation which, when stacked with N_{los} random projections, produces an ensemble phase-space that we use to identify the caustic profile. The exact steps are as follows:

1. N_{los} random lines-of-sight to a cluster are chosen, the galaxies are projected to create N_{los} radius-velocity projected phase-spaces.

2. N_{gal} galaxies are chosen randomly from the top N_{bright} brightest galaxies projected within the virial radius of the cluster in each phase-space. The N_{gal} brightest galaxies are chosen randomly to avoid artificial structure in the projected phase-space due to using the same cluster.

3. The stacked phase-space will contain the combined projected positions and velocities of $N_{ens} = N_{los} \times N_{gal}$ galaxies.

4. The caustic profile is identified and mass estimated for each stacked system.

How we choose N_{gal} from the top N_{bright} galaxies is carefully considered. There are several ways to achieve a desired sampling. First, along each line-of-sight to a cluster, galaxies can be rank ordered by a chosen magnitude (e.g. SDSS r-band) and the brightest galaxies are selected only from the top of the list ($N_{gal} = N_{bright}$). This method's advantage lies in its closeness to realistic spectroscopic follow-up. Usually, the brightest galaxies in any given field are given preference in spectroscopic surveys for practical purposes in observation and reduction.

The problem with sampling the same bright galaxies during the self-stacking process in simulations is the repeated measurements along different lines-of-sight. Due to the simple projection geometry, a single galaxy's projected distance from the cluster center changes very slowly as the observer's line-of-sight to the cluster shifts. If the observer plots the cluster projected phase-space position of a single galaxy for many different random lines-of-sight, the phase space will show strong vertical structure bounded by a maximum in projected distance equal to the 3D distance from the galaxy to the cluster center. When sampling many galaxies per line-of-sight, this artificial structure can heavily influence the phase space density, and consequently, the iso-density contour that defines the caustic profile. Ultimately, this leads to non-physical phase-spaces.

Another method of selecting galaxies along different lines-of-sight also requires sorting the galaxies brighter than some magnitude limit to create a list N_{bright}. However, instead of always taking the N_{gal} brightest galaxies from each line-of-sight, a fraction of the sorted list is selected in a random fashion. For example, if we wish to select 10 galaxies along each line-of-sight to a cluster to be stacked into the final ensemble, we could randomly choose these galaxies from a list of the 100 brightest

galaxies. This does not ensure complete uniqueness of galaxies in the final ensemble, but the frequency of repeated draws will become very low as $N_{gal} \ll N_{bright}$. Choosing the fractional difference between N_{gal} and N_{bright} using this method requires us to strike a balance. If we impose that the fraction be large ($N_{gal} \approx N_{bright}$), then there will be more artificial structure due to the repeated selection of galaxies like in the previous method. If instead we impose that the fraction be small ($N_{gal} \ll N_{bright}$), then galaxies will be randomly selected from a very large and therefore increasingly faint set of galaxies that may not be realistic for typical observed clusters. This can also increase the interloper-to-member ratio of galaxies in the phase-space which works to further blur the caustic edge in projection and increase the uncertainty in its position.

The third possible way of selecting galaxies is to assure that no galaxy appears in more than one line-of-sight phase space in the self-stacking analysis. While realistic in mimicking stacking unique systems, it results in individual line-of-sight (pre-stacked) phase-spaces that are populated with nearly all faint galaxies. While no artificial structure exists in the stacked phase-space, we do not pursue this method. We decide to use the second method to select galaxies due to its lack of artificial sub-structure with a fraction of 1/10.

4.4.1.2 Self-stacking Results

The results of self-stacking represent an ideal scenario where the expectation mass equals the mass of the cluster being self-stacked. It is now possible to test whether the act of stacking multiple phase-space projections results in any biases. As we point out in section 4.3, the stacked systems are close to spherically symmetric, and any observed biases are not due to cluster shape.

We test the self-stacking performance by varying either the number of lines-of-sight N_{los} stacked in phase-space or the number of bright galaxies N_{gal} we sample from each

line-of-sight. For example, to achieve a similar stacked richness of $N_{ens} = 500$, we can either stack $N_{los} = 10$ each with $N_{gal} = 50$ or $N_{los} = 50$ each with $N_{gal} = 10$. In Figure 4.3, we vary N_{gal} along the vertical direction and the N_{los} in the horizontal direction. The color map represents the degree of bias (left) and scatter (right) in the recovered masses as compared with M_{200} in the simulation. Contours of constant N_{ens} are displayed and labeled as diagonal lines in the figure.

Of primary concern is the average degree of self-stacked mass bias relative to the mass of each halo as a function of N_{los} and N_{gal}. We find the measured bias depends almost purely on N_{ens} and asymptotically approaches the input cluster mass when N_{ens} is large (lower right of Figure 4.3 left). On average, the stacks are unbiased to within 5% of the input cluster mass when $N_{ens} > 1000$. This holds even when the sampling per cluster is low ($\sim$ 10-15 galaxies) and we expect a significant low bias on individual systems as shown in Chapter II. We draw the conclusion that stacking multiple-phase spaces with individually unique velocity dispersions does not bias the mass inferred by the caustic technique.

Figure 4.3 right shows how the self-stacked mass scatter depends on N_{ens}. When $N_{gal} = 100$, the scatter decreases from $21 - 14\%$ as we increase the number of lines-of-sight included in each stack. This is approximately a factor of 2 less than the individual cluster mass scatter seen in Chapter II. We conclude that the scatter in stacked mass primarily depends on the total stacked richness which increases along an upper-left to lower-right diagonal in the parameter space.

The ensemble scatters are slightly higher than predicted in Chapter II which is due to the new surface calibration algorithm. Moving to direct caustic detection over velocity dispersion calibration of the escape velocity surface requires more heavily sampled phase-spaces to achieve similar levels of scatter. We accept this trade-off to remove any potential velocity dispersion biases either from velocity bias of the tracers or through Gaussian mixing in the stacking process (see §4.3.2).

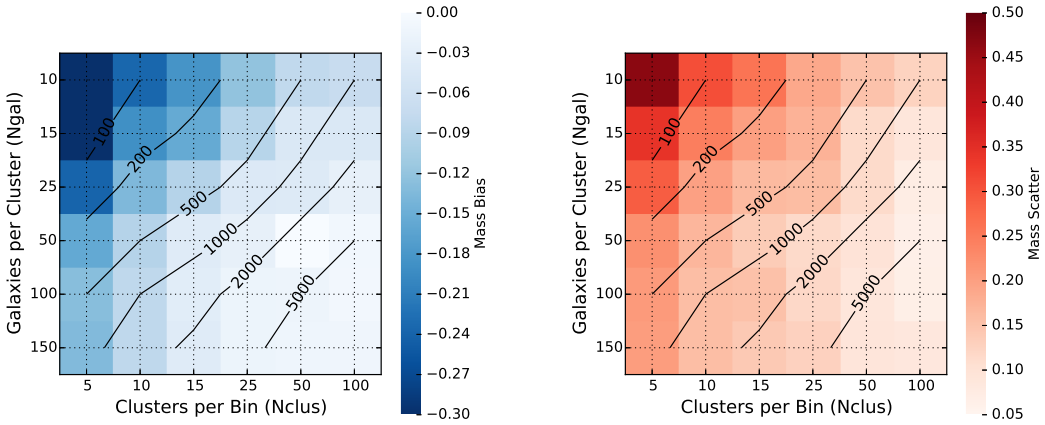

Figure 4.4: Left: We show caustic mass bias for mass-stacked ensembles as a function of the number of random lines-of-sight to each cluster and the number of galaxies sampled from each line-of-sight. The labeled diagonal lines are contours of constant stacked phase-space richness N_{ens}. Right: The caustic mass scatter for mass-stacked ensembles as a function of the number of random lines-of-sight to each cluster and the number of galaxies sampled from each line-of-sight.

4.4.2 Mass Stacking

In the previous section, we show that stacking projected phase-spaces from clusters of exactly the same mass does not result in a biased measurement of mass when the caustic edge is identified directly. However, this assumes the bins chosen to stack within are of infinitely small width in mass which is unphysical when stacking different clusters in simulations or observations. In an ideal scenario, we would bin clusters on an observable that has negligible scatter with mass. This would be functionally equivalent to binning on mass itself. Analytically, the expectation mass of each bin would then be

$$\langle M \rangle = \frac{\int M dn/dM \; dV/dz \; \psi(M) dM}{\int dn/dM \; dV/dz \; \psi(M) dM}, \tag{4.7}$$

where dn/dM is the halo mass function, and $\psi(M) = 1$ when $M \in [M_{200}^{min}, M_{200}^{max}]$ acting as a window function for each mass bin.

We define our bins by sorting our clusters in mass, and require that each mass

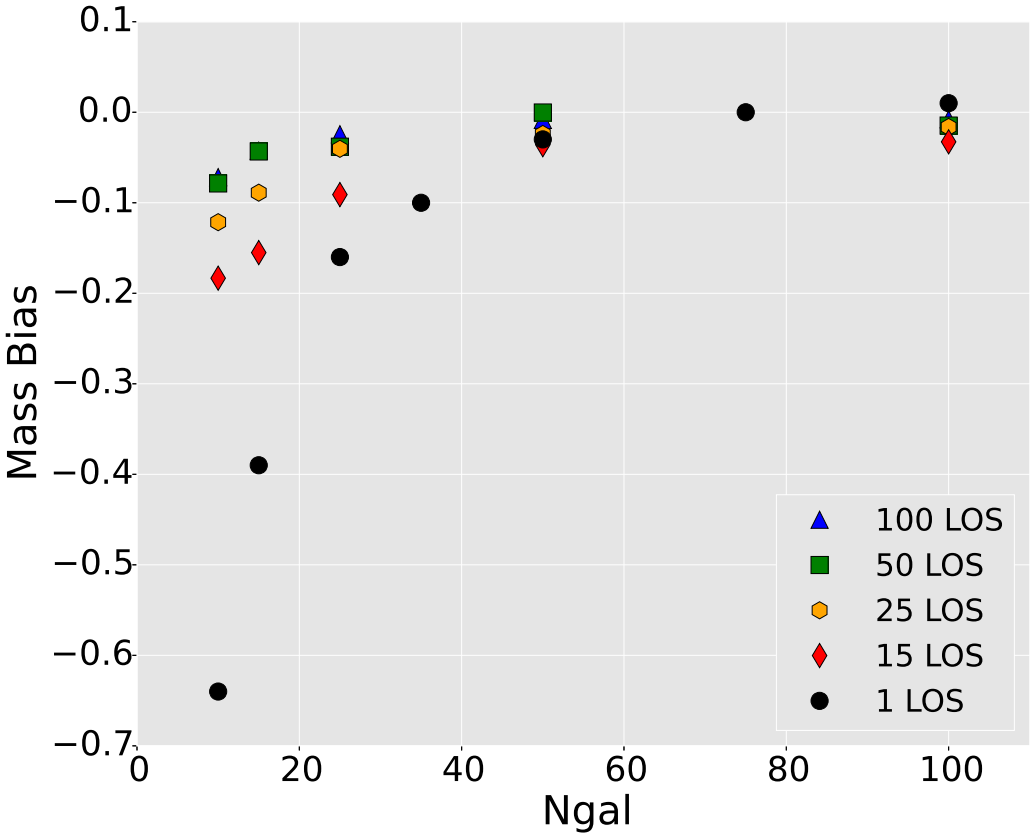

Figure 4.5: The bias between the measured stacked mass and the average cluster mass per stacked ensemble. The different points show the bias as a function of phase-space sampling. We compare with the result from Chapter II that measured the average caustic mass bias for individual systems (equivalent to 1 L.O.S) as a function of phase-space sampling. Stacking works to remove the sampling bias which cannot be achieved by averaging.

bin contain an equal number of clusters (N_{clus}). We can then vary N_{clus} to study the effects of including more clusters in a stack. This is formally equivalent to varying N_{los} in the self-stacking test described in section 4.4.1. Following this procedure, the width of our mass bins are related to our simulated cluster sample size and is not motivated by any observational or physical reason. As a consequence of keeping N_{clus} constant across all mass bins, the width of each mass bin will not be constant and adapt to the mass function of our sample. Because we have many more low than high mass clusters, the low mass bins will be far narrower than the high mass bins.

When stacking different clusters in a mass bin, we can select the top N_{gal} brightest galaxies from each cluster that are projected within r_{200} and are $< \pm 4000$km/s away from the cluster. This is similar to spectroscopic follow-up in practice where bright galaxies are usually observed with higher priority given a magnitude limited cluster survey. In observations, the number of bright galaxies will vary depending on both cluster size and redshift, but in this analysis we are able to set N_{gal} and test how mass scatter and bias depend on this trait.

Figure 4.4 is similar to Figure 4.3 which shows the degree of bias (left) and scatter (right) for the mass stacking technique as compared with the average cluster mass in each ensemble. We measure these properties as a function of both N_{gal} and N_{clus} and find the trend follows total ensemble sampling (N_{ens}) that is nearly identical to the self-stacked experiment. The scatter decreases as a function of richness to $< 10\%$ when the $N_{ens} > 2000$. By $N_{ens} = 1000$, we see the stacked mass estimates become unbiased which is in agreement with the self-stacking results.

Seen another way, Figure 4.5 shows the mass bias as a function of each ensemble's individual cluster sampling N_{gal} compared with results from Chapter II. Binning on 15, 25, 50, and 100 clusters (LOS) are shown as red diamonds, orange hexagons, green squares, and blue triangles respectively. The black circles represent the results from Chapter II using 100 clusters in the same Millennium simulation and measured

the average bias for individual systems in using the Guo et al. (2011) semi-analytic galaxy catalog. We find that stacking works to remove the bias observed in individual systems. Even when we only sample the brightest 15 galaxies per cluster, stacking 50 or more of these phase-spaces and measuring an ensemble caustic mass recovers the average mass to within 5% as compared with the original bias of -65%. The effects of low sampling can be seen when fewer clusters are stacked with $N_{gal} < 25$ as the method fails to identify the escape velocity edge.

It is important to emphasize that the reduction in statistical bias for the poorly sampled ensemble clusters cannot be replicated by averaging alone. "Ensembles" based on averaging individual cluster caustic masses will reduce scatter, but will fail to remove the known sampling biases. Stacked ensembles produce the high phase-space sampling required for accurate caustic masses and can work even when the individual per cluster sampling is low, or when the cluster is poor, i.e, there are not many galaxies to observe.

In §4.3.2, we mention that the stacked estimate of the velocity dispersion is expected to be biased relative to the average of the true cluster velocity dispersions in each stack due to mixing Gaussians. We test how these velocity dispersion biases translate to mass biases when using the stacked velocity dispersion to calibrate the stacked caustic surface. In our example in §4.3.2, we found average velocity dispersion biases of 3-10% depending on the interloper fraction of the stacked ensemble. We find this translates to an average stacked mass bias of $\sim 3\%$ when $N_{gal} = 15$ and $N_{clus} = 50$ to directly compare with our velocity dispersion example. If we increase the sampling per cluster to $N_{gal} = 50$, the stacked mass bias increases slightly to $\sim 6\%$. This confirms our hypothesis that using a biased velocity dispersion to calibrate our stacked caustic surface will return biased stacked masses compared with the average mass in each stack. We note that this level of uncertainty is similar to our uncertainty in $\mathcal{F}_\beta$ (see §4.3.1.)

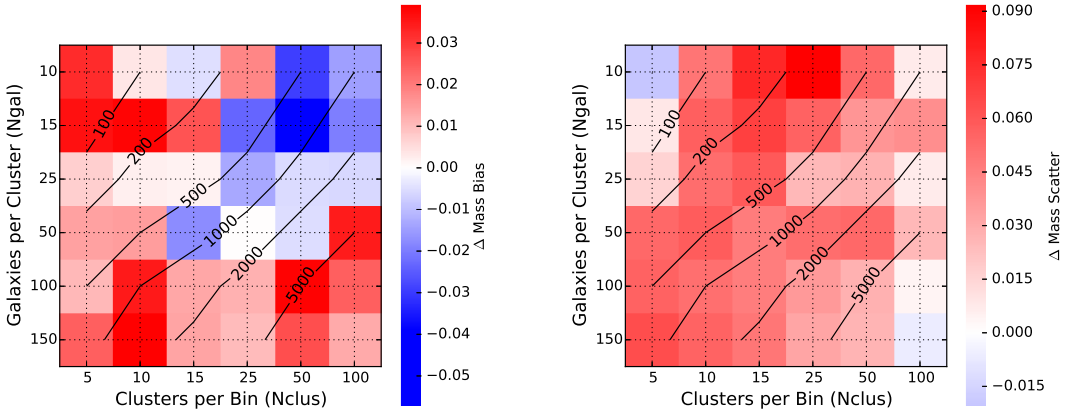

Figure 4.6: Left: The difference between the proxy-stacked and mass-stacked mass bias as a function of N_{gal} and N_{clus}. The absolute difference is $< 5\%$ when $N_{ens} > 1000$ Right: The cdifference between proxy-stacked and mass-stacked mass scatter as a function of N_{gal} per cluster and N_{clus} per stack. On average, the scatter increases by 4% when binning on richness.

4.4.3 Observable Stacking

In observations of real clusters, we must bin on cluster properties that correlate with mass. For optical surveys, examples of observables that act as mass proxies may include velocity dispersion, richness, or total luminosity. These observables often scale with mass through power law relationships that also include a degree of scatter. The relationship can be calibrated either in simulations or self-consistently in real observations, however, doing so requires an understanding of the scatter and uncertainty in the mass proxy measurement.

Scatter in mass-observable scaling relations are most commonly due to intrinsic variability and projection line-of-sight effects like non-spherical symmetry or contamination from interlopers and large scale structure. An example of intrinsic variability is two clusters of identical mass containing different richnesses of bright galaxies within their virial radii. This is a statistical scatter that will dominate if projection effects are minimal and represents an upper limit to the relationship's precision. However, scat-

ter between mass and observables are mostly limited by line-of-sight effects. Velocity dispersion is an excellent observable proxy of mass. In 3D, the velocity dispersion at fixed mass exhibits a minimal scatter of 5% and is independent of cosmology (Evrard et al., 2008). In projection, the scatter with mass can be as low as 15% for highly sampled systems or as high as 40% for systems with only a handful of spectroscopic members (Saro et al., 2013).

Scatter negatively affects our attempt to bin clusters based on these observable properties with the goal of closely binning on mass. Clusters with a given mass are randomly scattered between observable bins as a result of scatter in the mass-observable relationship. Because the mass function falls off sharply with mass, the up-scatter can particularly impact the high-mass bins by artificially increasing the number of clusters in those bins (Lima & Hu, 2005). This contamination between mass bins may affect the caustic mass estimates for each ensemble and bias the resulting stacked mass relative to the true observable-mass relation expectation. As described in Rozo et al. (2010), the average mass in a richness bin is modeled as

$$\langle M \rangle = \frac{\int M dn/dM \; dV/dz \; \langle \psi | M \rangle dM}{\int dn/dM \; dV/dz \; \langle \psi | M \rangle dM}, \tag{4.8}$$

where dn/dM is the halo mass function and

$$\langle \psi | M \rangle = \int P(N_{200}|M) \psi(N_{200}) dN_{200}. \tag{4.9}$$

Here, $\psi(N_{200}) = 1$ when $N_{200} \in [N_{200}^{min}, N_{200}^{max}]$ per bin, and $P(N_{200}|M)$ is the probability a cluster with mass M has a richness N_{200}. $\langle \psi | M \rangle$ then equals the probability that a cluster of mass M is observed within the richness bin controlled by ψ.

Observable-mass relations with extremely tight scatter that limit the effects listed above do exist as tested in high-resolution Nbody and gas dynamics simulations. Kravtsov et al. (2006) found that the product of the gas mass and temperature ob-

servables (Y_X) show a remarkably low scatter of $< 10\%$ with M_{500}. Unfortunately, these observables are often not available for the majority of optically identified clusters. Instead, we focus on optical observables such as cluster richness which is known to correlate tightly with mass. Rozo et al. (2009) used SDSS clusters to estimate the scatter on their matched-filter richness estimator (λ) and found $< 25\%$ log-scatter with M_{200} for clusters with $N = 40$. In our simulations, we utilize a simple richness estimator for a background subtracted galaxy count within a projected aperture on the sky equal to r_{200}. We estimate the background counts by sampling an area of sky 5x the cluster aperture, normalize by area, and take the difference from the cluster counts to measure N_{200}. Using the true values of M_{200} in the simulation and comparing with our estimated values of N_{200}, we measure a log-scatter in $P(N_{200}|M)$ equal to 20%, which is realistic when compared to Rozo et al. (2009).

We apply our estimates of N_{200} to our stacking framework in a similar systematic fashion as §4.4.2. The two variables of interest are the number of galaxies we sample from each cluster (N_{gal})and the number of clusters we stack per bin (N_{clus}). However, now instead of building our stacks based on cluster mass, we do so based on our optical richness observable. In Figure 4.6 (left) we present how the sampling and mass-scatter affect the stacked caustic mass bias for different types of sampling and binning relative to the results in Figure 4.4. We observe that, when binning on an observable with realistic scatter, the stacked caustic mass recovers the average mass of the stack with the same accuracy as our perfectly binned sample to within $\pm 3\%$. This result indicates that modest scatter in the mass-observable relationship does not impact the stacked caustic technique's ability to recover average masses in each observable bin. The scatter between the ensemble mass estimates and the average mass per bin is also minimally affected. In Figure 4.6 (right), we quantify the increase in scatter due to the increase in mass mixing in each observable bin. Across the range of galaxy and cluster sampling per bin, we see an increase in the scatter by $\sim 5\%$

when there exists scatter between the true mass and observational mass-proxy used to bin. Overall, the mass scatter for observable stacked ensembles is $10 - 15\%$.

In Figure 4.7, we show one-to-one plots of average cluster mass vs the stacked mass per bin with $N_{clus} = 50$ in both panels. The left panel stacks are built by sampling $N_{gal} = 15$ per cluster, and the right panel stacks by sampling $N_{gal} = 50$ per cluster. Unlike averaging, it is possible for stacked estimates to fail and return erroneous values; however, even when sampling only 15 galaxies per cluster, it happens rarely. With a modest degree of mass-mixing due to observable-mass scatter, only a few percent of our stacked estimates are classified as "failed stacks". These outliers are in the low mass end where our interloper rejection fails. Based on the low level of bias and scatter, combined with the lack of outliers in the stacked estimates, we can conclude that the stacking technique is robust to binning on a mass-proxy such as richness.

4.5 Discussion and Conclusions

Measuring dynamical cluster masses when $N_{gal} < 25$ can result in statistical (White et al., 2010) and systematic (Wu et al., 2013) biases that make it impossible to self-calibrate mass-observable scaling relations through averaging. Stacking works to eliminate any statistical biases present in individual cluster observations by building an ensemble system with sufficient sampling to measure average properties of the stacked system. However, using stacking methods to infer the average properties of clusters can be a messy process that depends on prior decisions of how to bin, which observable to bin on, the cluster finder and survey used, etc.

We have used halos in an all-sky light cone built on the Millennium Simulation (Guo et al., 2011; Henriques et al., 2012) to define a complete and pure, low redshift ($z \leq 0.15$) cluster sample. We then develop and characterize a caustic stacking technique to infer ensemble cluster masses. We find that the surface calibration in

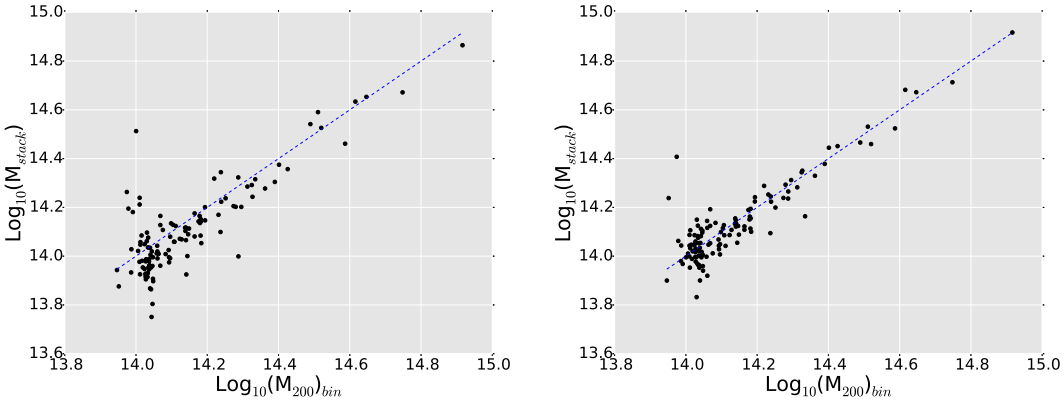

Figure 4.7: A comparison of the average mass in each observable bin compared with the respective stacked mass estimates using the caustic technique with direct surface detection. Each dot is an ensemble cluster and is constructed by binning on our richness observable. We use 50 clusters to build each ensemble and draw $N_{gal} = 15$ per cluster (left) and $N_{gal} = 50$ per cluster (right). The dotted line is the one-to-one line. Note that the low richness ensembles are biased $\sim 5\%$ low, consistent with Figure 4.6.

the caustic technique needs to be modified to avoid velocity biases. We define and test a new calibration of the caustic surface which leverages the well-populated ensemble phase-spaces. Our surface detection algorithm replaces the need for virial equilibrium and also eliminates where velocity dispersion bias can enter into the analysis. We note that since we have not tested our new surface calibration on other cosmologies, it may have a cosmological dependence that we have not yet characterized. On the other hand, the standard virial-based surface calibration imparts only a 6% statistical mass bias into the ensemble masses, which is similar to the the uncertainty on the caustic calibration term, $\mathcal{F}_\beta$.

We evaluate our new stacking procedure in terms of bias and scatter for three scenarios: (1) an ideal situation where the mass of an ensemble cluster is perfectly known and defined by a single cluster (self-stacking); (2) when the mass of the clusters are known but the ensemble contains a distribution of cluster masses; (3) when the mass of the clusters is inferred through a proxy with scatter and the ensemble is defined based on this proxy. This study should be viewed as a baseline ability of

the stacked caustic technique to recover average cluster masses. The completeness, purity, and mis-centering of cluster finding methods may well influence the results presented here (Miller et al., 2005; Rozo et al., 2009).

When creating the ensemble clusters, we vary the number of galaxies sampled per cluster and the number of clusters per bin. We find that the agreement between the stacked caustic estimate and the average true mass of the bin depends on the total sampling in the stacked cluster projected phase-space. Once we achieve a level of sampling of ~ 1000 of the stacked phase-space, our estimates are unbiased to within 5%. The bias follows the iso-sampling contours very closely, implying that achieving precise stacked estimates depends solely on phase-space sampling.

Finally, we test our stacking technique by stacking/binning clusters on an observable mass proxy. We use a simple richness estimator to demonstrate the effects of adding uncertainty to the binning process. When binning on richness, we find the ensemble mass is still able to recover the average mass to within $\sim 5\%$, matching the scenario where we assume no scatter between observable and mass. These encouraging results suggest that when stacking, scatter in the mass-observable relationship does not play a large role in recovering average masses making calibration of the the mass-observable relationship possible. Not only do the results converge to be unbiased, the accuracy is independent of cluster mass regardless of binning procedure.

Our tests also reveal that stacking results in very low mass scatter relative to the average cluster mass per bin. When we stack on both mass and our mass proxy richness, the stacked mass scatter is $\lesssim 10\%$ when our phase-space sampling is high ($N_{ens} > 5000$). For lower sampling ($N_{ens} < 2000$), we see that stacking on an observable like richness introduces $\sim 5\%$ to the average mass scatter. We find slightly higher values of mass scatter in our initial tests with self-stacking, but this is due to variance in our galaxy selection methods (see §4.4.1.1).

Stacking, using our updated caustic technique, works to both remove statistical

bias and lower scatter from ensemble mass estimates. Combined, we have a powerful conclusion that these methods can be used to self-calibrate observable-mass scaling relations in observations without relying on statistical bias corrections calculated in any simulation. These simulation efforts coincide with current surveys like the Dark Energy Survey (Flaugher et al., 2015), the Baryon Acoustic Oscillation Survey and its extension eBOSS (extendedBOSS is part of a proposed program of post-2014 surveys on the Sloan telescope), the South Pole Telescope survey (Chang et al., 2009), the XMM Cluster Survey (Sahlén et al., 2009), as well as future surveys like the Large Synoptic Survey Telescope (LSST Science Collaboration, 2009), the Dark Energy Spectroscopic Instrument Levi et al. (2013), S4 (Albrecht et al., 2006), and eRosita (Merloni et al., 2012). Each of these surveys is providing (or will provide) a wealth of new photometric, spectroscopic, Sunyaev-Zeldovich (SZ), and X-ray data for clusters over a wide range of mass and redshift. Utilizing stacking techniques such as the one outlined in this study can work to leverage the survey observables by self-calibrating the mass-observable relationships. Such relations are instrumental to using clusters as probes to understand cosmology.

CHAPTER V

The C4 Cluster Mass Function

5.1 Introduction

Due to hierarchical structure formation, the number of dark matter halos as a function of mass and redshift can be described by the halo mass function. In theory, the abundance of galaxy cluster sized halos depends exponentially on the rms value of density perturbations on 8Mpc scales (σ_8). In addition, the matter density (Ω_M) and the nature and evolution of dark energy (Ω_Λ,w) influence the theoretical mass function and can be constrained through observations. Following initial theoretical characterization (Press & Schechter, 1974; Sheth & Tormen, 2002), the mass function has been carefully calibrated in simulations with various cosmologies that closely match their respective abundance functions (Jenkins et al., 2001; Warren et al., 2006; Tinker et al., 2008; Angulo et al., 2012). The growth of large cosmological simulations used to theoretically predict abundance functions has only worked to highlight the difficulties faced observationally.

The major source of difficulty in using the theoretical predictions is that they describe the abundance function as a function of dark matter halo mass. As this is an unobservable property, one must use cluster observables in either a physical way or as mass proxies to estimate the underlying halo mass. Physical mass estimators include measuring the galaxy dynamics and assuming virial equilibrium (Carlberg

et al., 1996), measuring the escape velocity (Diaferio, 1999; Serra et al., 2011), or modeling the cluster projected phase-space (Wojtak & Łokas, 2010; Mamon et al., 2013), the temperature of the hot x-ray gas at the center of clusters and assuming hydrostatic equilibrium, or the lensing shear from the line-of-sight mass distribution (Becker & Kravtsov, 2011; Hoekstra et al., 2015). Mass proxies now include cluster richness (Rozo et al., 2009; Andreon & Hurn, 2010), SZ signal (Saliwanchik et al., 2013; Bocquet et al., 2015; Saro et al., 2015), X-ray observables (Mantz et al., 2010a), and velocity dispersion (Evrard et al., 2008). Using both physical and mass proxies in cosmological analyses introduce significant systematic uncertainties that are often the dominant source of error. This error has resulted in a range of estimated values for σ_8 that is larger than the expected error on any given study (Evrard et al., 2002; Rines et al., 2007; Henry et al., 2009; Vikhlinin et al., 2009; Rozo et al., 2010). While cosmological parameter estimates are beginning to converge, the recent perceived tension between cluster inferred cosmology and cosmic microwave background cosmology (Planck Collaboration et al., 2014b) works to highlight the importance of understanding systematics in cluster mass estimation.

In this work, we use dynamical masses inferred from the caustic technique to measure the C4 mass abundance function in the local universe. The caustic technique has been shown to agree well with other independent mass estimates (Diaferio et al., 2005; Sharon et al., 2015) and can recover cluster masses to 30% in well sampled systems. The masses are measured on a cluster-by-cluster basis and potential biases are checked against a mock cluster catalog in the Millennium Simulation. Our Bayesian approach to the likelihood function avoids binning on mass and inherently models uncertainties in the estimated masses and accounts for the the sample purity and completeness (Cash, 1979; Mantz et al., 2010b; Hasselfield et al., 2013). We assume $H_0 = 100h$ km $s^{-1}Mpc^{-1}$, and a flat cosmology with $\Omega_\Lambda = 1 - \Omega_M$ throughout.

5.2 Data

5.2.1 Henriques Semi-analytic Galaxies

In order to better understand the C4 completeness function, purity, mass estimate accuracy, and test our likelihood models, we utilize the Guo et al. (2011) semi-analytic galaxy catalog and the Millennium Simulation (Springel et al., 2005). Semi-analytic galaxy catalogs are built on top of identified subhalos in an N-body simulation through a set of analytic prescriptions based on astrophysical conditions that occur both below and above the resolution limit of the simulation. Subhalos are defined and located using algorithms such as SUBFIND (Springel et al., 2001) which have been shown to work well to identify all of the sub-structure in N-body simulations (see also Knebe et al., 2011). The semi-analytic model applies its rule set to transform properties such as subhalo mass and position into galaxy mass, circular velocity, accretion rate, and other physical parameters that can, in theory, be observed. The Millennium simulation was run with a flat cosmology of $\Omega_M = 0.25$, $\Omega_\Lambda = 0.75$, $\Omega_b = 0.045$, $\sigma_8 = 0.9$, $h = 0.73$, and $n_s = 1.0$.

An all-sky light cone was built using this semi-analytic population (Henriques et al., 2012). The C4 algorithm (see §5.2.2) is run on the original data set to produce a cluster catalog that mimics the true C4-survey, albeit with larger sky coverage. The resulting mock catalog contains 250 clusters with redshifts $0.03 < z < 0.12$, most of which have more than 20 galaxies in their phase-space, on one quarter of the sky. We limit our cluster redshift range to be between $0.0 - 0.12$ in one quarter of the sky to mimic the portion of the C4-survey we use in this analysis. We also make a cut on estimated caustic mass at $1.0 \times 10^{14} M_\odot$ below which the majority of clusters have phase-space richness is less than 20 galaxies and the uncertainty in the caustic mass estimates climbs above 60% (see Chapter II). This sample allows us to place constraints on model parameters and test for systematics in our likelihood model.

5.2.2 The C4 algorithm and Cluster Catalog

The SDSS-C4 cluster finding algorithm was presented in Miller et al. (2005). The foundation of the algorithm is to use the five filters of the Sloan Digital Sky Survey (SDSS; York et al., 2000) to identify galaxies which are clustered spatially as well as in a four-dimensional color-space. The premise is that galaxies within clusters evolved similarly, and thus galaxy clusters contain subsets of galaxies that have similar spectral energy distributions (SEDs). Note that the C4 algorithm is not a red-sequence finder and it does not require any parameterization of the color-magnitude relation in clusters. Once identified, these color-clustered "C4 galaxies" represent a small percentage of the total galaxy population. They are then used to identify the locations of clusters. We apply the C4 algorithm to the latest SDSS DR12 data (Eisenstein et al., 2011; Alam et al., 2015). We use all galaxies with spectroscopic measurements which also have clean photometry to identify the clustered galaxies.

In the original C4 algorithm, a circular-over-density algorithm (i.e., the projection of a spherical over-density) is used to identify the clusters from the C4 galaxies. However, this algorithm works best when clusters are spherical (or projected circles), which is rarely the case. We have modified the C4 algorithm to use a Mean Shift clustering algorithm as described in Vanderplas et al. (2012). Mean shift clustering is a non-parametric method to discover clusters in a smooth density of sampled point-wise data. It is a centroid-based algorithm, which works by updating candidates for centroids to be the mean of the points within a given region. We also apply a new de-blending technique to the originally identified clusters by fitting a 3-component Gaussian mixture model to the Mean Shift clusters. We find that $\sim 30\%$ of the clusters identified by the Mean Shift algorithm are composed of two or three clusters, identified in the Gaussian Mixture Model.

Once the cluster locations are identified, we post-process them using all of the available SDSS galaxy data with spectroscopy and all clean photometry (i.e., not

just the spectroscopic data set). In this post-processing, we identify the Brightest Cluster Galaxies (BCG) as the brightest galaxy within 2σ of the best-linear fit to the color-magnitude relation (i.e., the E/S0 ridgeline, using the g and r bands). We measure the redshift of the cluster using a bi-weight robust median of all galaxy redshifts within a projected megaparsec aperture. We estimate a velocity dispersion with respect to the cluster redshift and also within a fixed megaparsec aperture. We infer the physical radius at which the surface density of galaxies reaches $200\times$ the average mean density of galaxies as expected from the SDSS galaxy luminosity function (Blanton et al., 2003). We then estimate cluster richnesses using all galaxies within 2σ of the E/S0 ridgeline, within twice the velocity dispersion, and out to the estimate of r_{200}. These quantities serve as input to the cluster mass estimation and abundance measurements as described below.

5.2.3 OSMOS Data

The SDSS uses a fiber-fed spectrograph to collect spectra to measure redshifts. One challenge in any spectroscopic observing program of galaxy clusters is dealing with the high spatial density of targets on the sky. In fiber-fed systems, the fibers are limited in how closely they can be packed based on their diameter. Because of the high spatial density of galaxies in clusters, SDSS shows completeness in clusters that can be as low as 50-70%. In Chapter II we look at how the caustic technique depends on radial incompleteness in simulated clusters and find the mass estimates to be biased on the 5-10% level when serious incompleteness is present.

To rectify this known systematic in our cluster catalog, we identified some 45 clusters in the C4 catalog to follow up spectroscopically with the OSMOS (Ohio State Multi-Object Spectrograph) instrument on the MDM 2.4m Hiltner Telescope. Clusters were selected for the possibility of follow-up if they had large ($> 5e14 M_{\odot}$) initial virial and caustic mass estimates, but contained less than the 50 galaxies

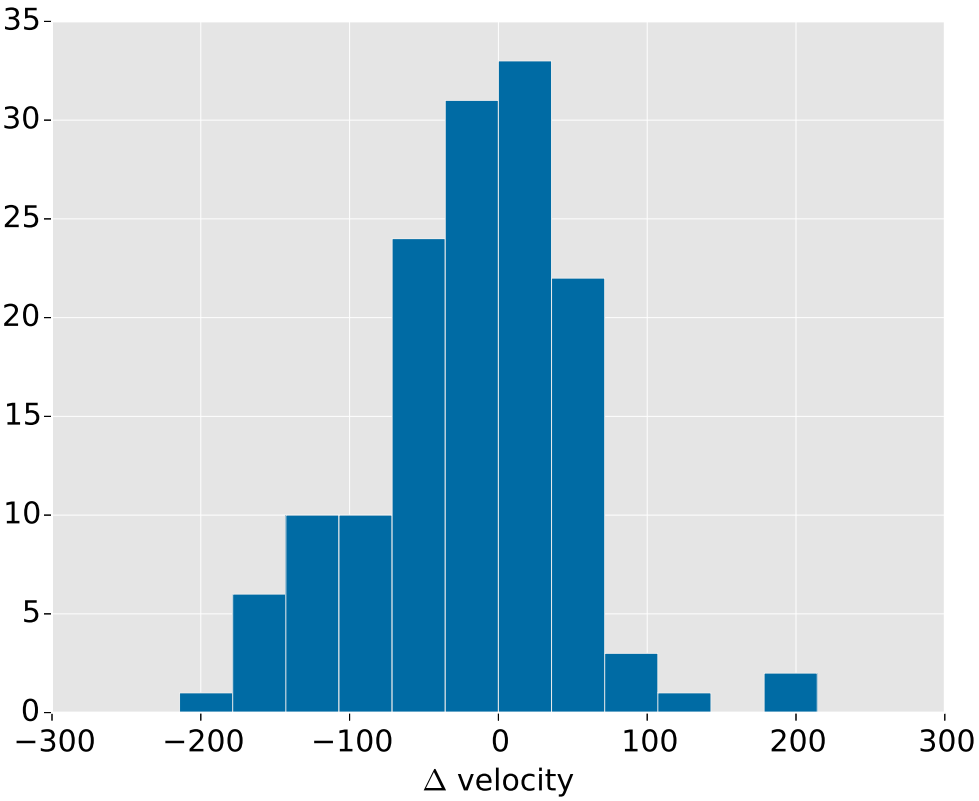

Figure 5.1: A histogram showing the distribution of velocity differences calculated for galaxies with spectra taken at MDM with the OSMOS spectrograph (reduced using OSMOSReduce) and SDSS measurements. The width of the distribution of Δv is about 60 km/s which matches the uncertainties on redshifts estimated by SDSS.

needed to achieve accurate mass estimates (see Chapter II) due to incompleteness. The OSMOS instrument uses slit masks with room for roughly 20-40 individual slits depending on the number and density of objects in the roughly 20' field of view. Each cluster in our follow-up must also have enough galaxies with unmeasured redshifts to fix the measured incompleteness.

We reduce the multi-slit spectra and estimate redshifts with a new reduction pipeline created by the authors which is shared as open source code under the name OSMOSReduce. This package performs basic and advanced image and spectra reduction including distortion correction, object recognition, in-slit sky subtraction,

6th order polynomial wavelength calibration fitting, and automatic as well as user controlled redshift estimation through galaxy template cross-correlation. When possible in our observations, we re-measured redshifts for SDSS spectroscopic galaxies to verify the accuracy of our redshift estimates. In Figure 5.1 we show that our redshift inferred peculiar velocities agree with the SDSS redshifts/velocities within 60km/s. This is near the quoted uncertainties of SDSS redshifts, so we are confident that our reduction pipeline produces quality redshifts. In total we measure 110 new redshifts.

5.2.4 Mass Estimates

Under Newtonian dynamics, the escape velocity of a spherically symmetric cluster relates to its gravitational potential by

$$v_{esc}^2(r) = -2\Phi(r), \tag{5.1}$$

where r is the 3-dimensional measured distance to the center of the cluster. If the dynamics of the system are controlled by the gravitational potential, galaxies which cannot escape the potential exist in a well-defined region of radius/velocity $(r - v)$ phase space. The extrema of the velocities in this phase space define an edge, the escape velocity profile $v_{esc}(r)$, which can be measured directly with 3 dimensional position and velocity information, or estimated using projected sky coordinates and line-of-sight velocities in observations. Given the measured $v_{esc}(r)$, the escape velocity or "caustic" technique allows one to infer the mass profile of a cluster to well beyond the virial radius (Diaferio & Geller, 1997). The equation

$$GM(< R) = \mathcal{F}_\beta \int_0^{r_{200}} v_{esc}^2(r) dr \tag{5.2}$$

calculates the mass within the critical radius r_{200} where $v^2_{esc}(r)$ is the measured (projected) escape velocity profile and $\mathcal{F}_\beta$ is a function which depends on the density, the potential, and the projected anisotropy profile. It is usually approximated as a constant and calibrated through simulations. We use a value of $\mathcal{F}_\beta = 0.65 \pm 0.02$ matching our findings in Chapter II. Our caustic algorithm has been tested extensively with respect to M_{200c} where $200c$ is $200\times$ the critical density of the universe. However, the mass function is usually defined relative to the mean density. We do have the ability to simply estimate M_{200} relative to the mean density from our mass profiles, but that requires integrating to larger radii as the mean mass is always greater than the critical mass. With well sampled systems this is not a problem, but we find through tests in the Millennium Simulation, we can recover M_{200} mean more accurately and with less scatter by estimating M_{200c} and multiplying by the constant 1.45. The constant is an empirical quantity that depends on the extrapolation of the cluster profile to larger radii and is not the same for all clusters. This induces some scatter in M_{200} mean, but less so than directly estimating the value from the caustic profiles. Hereafter, references to M_{200} refer to the over-density relative to the mean background density.

5.2.5 C4 Systematics

In Chapter II, the bias and scatter in estimated caustic and virial mass was quantified for clusters over a range of masses that did not include incompleteness, purity, and off-centering. All these must be considered carefully when using survey data to estimate masses and constrain cosmology. Measuring the cluster center as offset from the Brightest Cluster Galaxy (BCG) in the simulation can cause both over and underestimates in caustic masses, thereby inducing scatter into the estimates. Incompleteness and purity work to raise and lower the expected number of halos we observed within a cosmological volume, and influences the best fit model to the observed data. With the Henriques-C4 catalog, we have the opportunity to test these

factors independently and see if they vary with mass.

We measure the expected caustic mass bias and scatter by sampling the clusters in the Henriques-C4 that are within a projected virial radius and suitable redshift range as a halo in the simulation catalog. With these matches, we can then estimate the caustic mass bias and scatter in a straightforward manner. Like in Chapter II, we measure the bias and scatter in $\ln(\widehat{M}/M_{200})$. We find that the average cluster sample is unbiased to within 5% of the matched halo masses. When we measure the average bias for clusters with less than 30 phase-space members, we also see unbiased results (with much higher scatter) to within 5%. This is different than the findings in Chapter II that expect statistical biases due to sampling of $< -10\%$ when the number of member galaxies drops below 30. This could be due to slight amounts of off-centering of the cluster finder, but is more likely due to uncertainties in r_{200} which were not tested in Chapter II. For scatter, we measure $\sqrt{\langle \ln(\widehat{M}/M_{200})^2 \rangle} = 0.60$. This value is higher by roughly 10% from what we predict with known r_{200} values in the same simulation. We discuss this more in section 5.3.2.

The C4-algorithm attempts to maximize completeness and purity of the sample through the methods described in §5.2.2. Completeness is defined as the fraction of true halos that we successfully find in our catalog. Completeness of the survey can be quantified as a function of true halo mass and also redshift. This is ideal since we apply the halo completeness function to the product of the halo mass function and partial volume $dn/dm \cdot dV/dz$. We measure completeness by matching Henriques-C4 clusters to simulation halos through the method described when estimating mass scatter and bias. To do so, we measure the total fraction of halos we find in logarithmically spaced mass bins as well as bins in redshift to find a completeness function shown in Figure 5.2. Despite the completeness rapidly falling off as a function of mass and redshift, within our mass range of interest ($10^{14} - 10^{15} M_{\odot}$), we can model each curve with either a single linear or broken-linear fit between $0 - 100\%$ completeness. However,

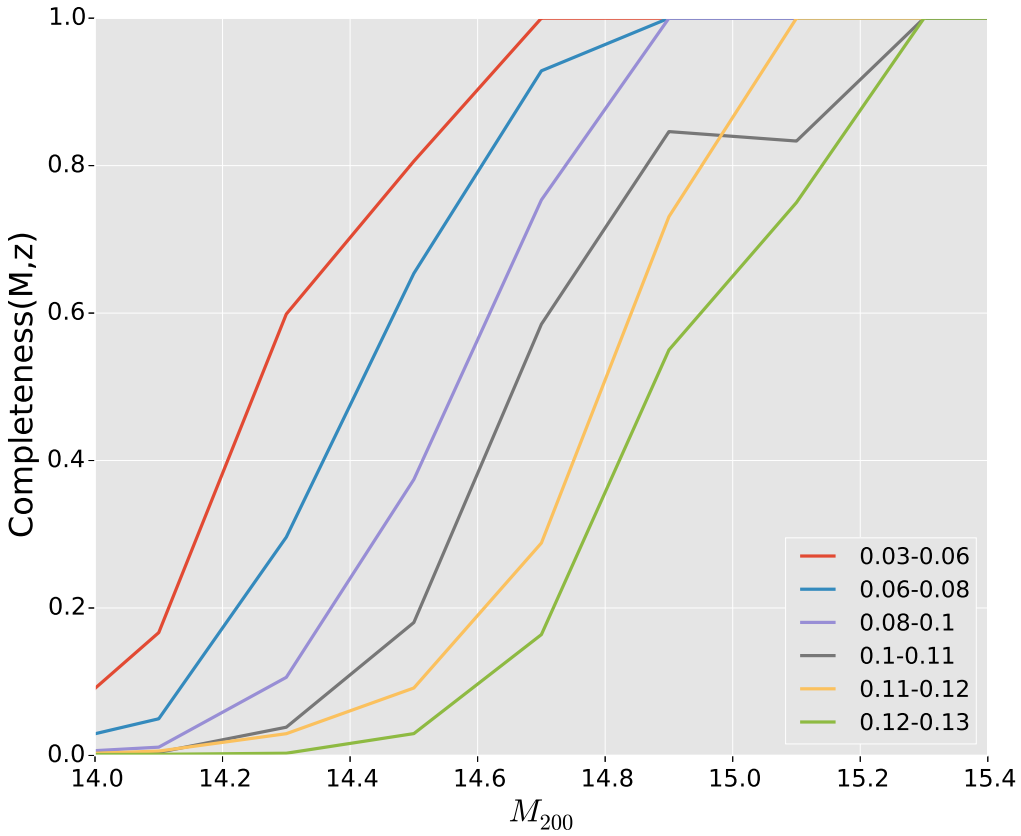

Figure 5.2: The measured completeness function in our Henriques-C4 sample of galaxy clusters. We measure completeness both as a function of mass and redshift out to $z = 0.12$. At large halo mass $\sim 10^{15} M_{\odot}$, we see statistical jumps in completeness that are due to low number statistics.

these curves do contain uncertainty. Due to a limited number of clusters, there will be variation in the fraction of halos we successfully identify akin to statistical sampling uncertainty. To test for this variation, we measure the completeness in four distinct quadrants of the Henriques light-cone and find a variation of $\pm 10\%$ for relative to the average value for all mass bins that are incomplete. We account for this uncertainty in our model described in sections 5.3.1 and 5.3.2.

We cannot measure the purity of our sample as a function of halo mass since purity is based instead on a cluster observable. Purity is defined as the fraction of

clusters that we find in our catalog that are real halos and not false detections due to challenges like projection effects or deblending of systems. When we look at how the purity scales with caustic mass (which scales linearly with M_{200}), we find no dependence on the overall impure fraction with mass and a value of $80 \pm 5\%$. When we do the same thing as a function of redshift, we find almost no dependence with the fraction holding constant for $z < 0.12$. We therefore adopt a constant purity of $80 \pm 5\%$ through the rest of the analysis.

We make cuts to the SDSS-C4 data as well as the Henriques-C4 catalog on C4 richness and estimated caustic mass. After making cuts between $1.0 \times 10^{14} - 2.0 \times 10^{15} M_{\odot}$ in mass, more than 15 identified C4 members (the phase-space will contain more than this number), and $z < 0.12$ as our estimated completeness function drops very low and becomes very noisy at higher redshift, we are left with ≈ 220 systems. To-date, the largest sample used in a caustic mass function analysis was performed by Rines et al. (2007) who estimated virial and caustic masses for 72 clusters. Our larger sample reduces statistical uncertainties and variation due to cosmic variance on small volumes.

5.3 Analysis

5.3.1 Likelihood models

Here we describe the Bayesian likelihood function of cosmological and mass parameters given our cluster sample with mass and redshift information. Typically, the predicted theoretical cluster abundance function is fit to an observed sample by binning on estimated mass (Rines et al., 2007) or cluster observable such as richness or luminosity and self-consistently constraining scaling relations (Rozo et al., 2010; Mantz et al., 2010b; Hasselfield et al., 2013). A binned analysis is required if masses are calculated for ensemble clusters stacked on a cluster observable. With

accurate individual mass estimates, we utilize the derivation presented in Cash (1979) for unbinned data based on the application of Poisson statistics. This approach has been used in previous studies to obtain cosmological constraints as well as calibrating common mass-observable scaling relations (Vikhlinin et al., 2009; Mantz et al., 2010b; Hasselfield et al., 2013). In this analysis, we have direct dynamical mass estimates that do not originate from a scaling relation with uncertain calibration.

Each cluster in our analysis has an unknown and unobserved true mass M. Given a cosmological model $\boldsymbol{\theta} = (e.g.\ \Omega_M, \sigma_8, h)$ and observable parameters $\boldsymbol{\xi} = (\mathcal{F}_\beta, \mathcal{C}_{M,z}, \widehat{\kappa})$ where $\mathcal{C}_{M,z}$ is the completeness/purity function and $\widehat{\kappa}$ is the sample scatter, we make use of the Tinker et al. (2008) mass function $dn/d\ln M$ to predict the probability of a cluster with a given mass and redshift existing in our sample. The theoretical mass functions are calculated using the Python code HMF which is the backend to the online mass function calculator HMFcalc (Murray et al., 2013).

The probability density distribution of a measured caustic mass $\widehat{M}$ is given by the convolution of the distribution of true masses M and the scatter, $\widehat{\kappa}$, between $\ln\widehat{M}$ and $\ln M$. The scatter contains both intrinsic as well as systematic uncertainties, but we do not attempt to distinguish between them in this analysis. The convolution and predicted number density in our model parameter subspace can be written as

$$\begin{aligned} n(\widehat{M}, z|\boldsymbol{\theta}, \boldsymbol{\xi}) = & \frac{1}{\widehat{M}} \frac{1}{\sqrt{2\pi}\widehat{\kappa}} \int_{-\infty}^{\infty} \mathcal{C}_{M,z} \frac{dn}{d\ln M} \frac{dV}{dz} \\ & \times e^{-\frac{(\ln\widehat{M} - \ln M)^2}{2\widehat{\kappa}^2}} d\ln M. \end{aligned} \tag{5.3}$$

Cash (1979) states that if we bin very finely in the space of our observables (bins indexed by μ with bin volume V_μ), we expect the total predicted counts in each bin to be $V_\mu n(\widehat{M}_\mu, z_\mu|\boldsymbol{\theta}, \boldsymbol{\xi})$, and the number of observed clusters in each bin either be 0 or 1. The binary nature of each bin is denoted with p_μ. If we assume Poisson statistics

in each bin, the probability of the data given the model parameters is defined as

$$\begin{aligned} P(\widehat{M}, z|\boldsymbol{\theta}, \boldsymbol{\xi}) &= \prod_{\mu} e^{-n_\mu(\widehat{M}, z|\boldsymbol{\theta}, \boldsymbol{\xi})} n_\mu(\widehat{M}, z|\boldsymbol{\theta}, \boldsymbol{\xi})^{p_\mu} \\ &= e^{-N(\boldsymbol{\theta}, \boldsymbol{\xi})} \prod_{i} n(\widehat{M}_i, z_i|\boldsymbol{\theta}, \boldsymbol{\xi}) \end{aligned} \tag{5.4}$$

where i is the index over each of our clusters, and

$$\begin{aligned} N(\boldsymbol{\theta}, \boldsymbol{\xi}) &= \int n(\widehat{M}, z|\boldsymbol{\theta}, \boldsymbol{\xi}) d\ln\widehat{M} dz \\ &= \int_{z_{\min}}^{z_{\max}} dz \int_{-\infty}^{\infty} d\ln M \mathcal{C}_{M,z} \frac{dn}{d\ln M} \\ &\times \frac{dV}{dz} \int_{\ln M_{\min}}^{\ln M_{\max}} \frac{1}{\sqrt{2\pi}\widehat{\kappa}} \\ &\times \exp\left(-\frac{(\ln\widehat{M} - \ln M)^2}{2\widehat{\kappa}^2}\right) d\ln\widehat{M}. \end{aligned} \tag{5.5}$$

which is the expected total number of clusters based on our model parameters.

The final integral over the estimated masses $d\ln\widehat{M}$ is actually the integral of the standard normal distribution, called the cumulative distribution $\Phi(x)$, which can be numerically calculated using the complimentary error function

$$\Phi\left(\frac{(\ln M_{\min} - \ln M)}{\sqrt{2}\widehat{\kappa}}, \frac{(\ln M_{\max} - \ln M)}{\sqrt{2}\widehat{\kappa}}\right) \tag{5.6}$$

where

$$\Phi(x_1, x_2) = \frac{1}{2}\mathrm{erfc}(x/\sqrt{2}). \tag{5.7}$$

$$\mathrm{erfc}(x/\sqrt{2}) = 1 + \frac{1}{\sqrt{2\pi}} \int_{-x}^{x} e^{-t^2/2} dt. \tag{5.8}$$

Because our uncertainties on the cluster masses are heteroschedastic, we use the average sample scatter of $\widehat{\kappa}$.

Computationally, we sample the posterior probability distribution using an Affine-Invarient Ensemble Sampler in the Python package emcee (Foreman-Mackey et al., 2013). This allows us to run multiple MCMC chains simultaneously in parallel to effectively and efficiently sample the posterior. The final log-likelihood of the data given our model is

$$\ln L \propto \sum_i \Big(\ln n(\widehat{M}_i, z_i | \boldsymbol{\theta}, \boldsymbol{\xi}) \Big) - N(\boldsymbol{\theta}, \boldsymbol{\xi}) \tag{5.9}$$

5.3.2 Model Parameters and Priors

Here we describe our prior assumptions about each of the parameters entering our model. The primary goal of our analysis is to place constraints on cosmological parameters σ_8 and Ω_m, however, several other parameters exhibit uncertainty and can be modeled within our likelihood function. Throughout our analysis, we assume a flat ΛCDM cosmology. In our likelihood analysis, the Hubble constant and power spectrum tilt are held fixed. Clusters are especially efficient at constraining σ_8 and Ω_m, and therefore, these parameters are treated with the least restrictive priors in our model. The priors on σ_8 and Ω_m are flat and nonrestrictive. The bounds on these $0.4 < \sigma_8 < 1.2$ and $0.10 < \Omega_M < 0.9$.

As described in §5.3, we assume our measured masses $\widehat{M}$ exhibit log-normal scatter κ relative to the true M_{200} masses of our clusters. In Chapter II, we quantify the expected average log scatter as a function of phase-space sampling N_{gal} which we use here to estimate the caustic mass uncertainty. In Chapter II we tested discrete cases, so we fit a function to interpolate scatter estimates to all values of sampling. We find the scatter scales with phase-space sampling as

$$\ln \kappa = \frac{4.85}{\ln N_{gal}} - 2.14. \tag{5.10}$$

These values of $\kappa(N_{gal})$ were measured in the Millennium Simulation with known halo positions. We retest this with a cluster catalog generated by the C4 cluster finder on the Henriques lightcone, the details of which are specified in §5.2.1. Comparing our caustic estimates for clusters with matching halos in the simulation, we find the scatter to be approximately 10% higher than the predictions from equation 5.10. We therefore define the uncertainty on each individual cluster i to be $\widehat{\kappa}_i = \kappa_i + 0.10$. In our likelihood model, we place a normal prior on the average scatter of

$$P(\widehat{\kappa}) = \mathcal{N}\left(0.6, 0.1\right). \tag{5.11}$$

Caustic masses for our clusters are measured using equation 5.2. The value of the constant $\mathcal{F}_\beta$ is a source debate and uncertainty in returning unbiased masses for our cluster sample (Diaferio, 1999; Serra et al., 2011; Svensmark et al., 2015). Recently, studies have converged on a value of $\mathcal{F}_\beta \approx 0.6 - 0.65$ (Svensmark et al., 2015). Here, we calculate our masses assuming a Gaussian prior on $\mathcal{F}_\beta$ as,

$$P(\mathcal{F}_\beta) = \mathcal{N}\left(0.65, 0.02\right) \tag{5.12}$$

where the uncertainty $\sigma_{\mathcal{F}\beta} = 0.02$ in $\mathcal{F}_\beta$ is based on the results in Chapter II which is the spread in $\mathcal{F}_\beta$ values that return unbiased mass estimates for the four semi-analytics in the Millennium Simulation. In addition, we can also assume an NFW functional form for $\mathcal{F}_\beta$ as presented in equation 3.5, using the concentration for each cluster based on a mass-concentration relation (Merten et al., 2015) and its uncertainties, calculating the average value of $\mathcal{F}_\beta$ for each cluster inside r_{200} based on $\widehat{M}$, and finally averaging those individual estimates (see section 4.3.1). This results in an uncertainty $\sigma_{\mathcal{F}\beta} = 0.05$. We test how both of these uncertainties affect our cosmological model inferences in section 5.4.

As described in section 5.2.5, the completeness function we measure in the simu-

lations carries some uncertainty when applied to a different data set. Using different volumes in the Henriques light-cone with similar sizes to our SDSS observed volume, we find at most a 20% variation with respect to the completeness of a given true mass at all redshifts in our sample. To allow for variation at different redshifts, we add four nuisance parameters (c_1-c_4) to our model that act as fractional multipliers to the completeness function in four redshift bins (0 - 0.06 - 0.08 - 0.1 - 0.12). These parameters have priors that are normal which we define as,

$$P(c_{1-4}) = \mathcal{N}(1.0, 0.1)\,, \tag{5.13}$$

but we also restrict their values to be $0.8 < c_i < 1.2$. Our last parameter, the purity of the C4 sample, we measure in the simulations to be 80 ± 0.05 and is treated as a flat prior within the uncertainty in our model.

5.4 Results

5.4.1 Henriques-C4 Millennium Simulation Mass Function

In order to check the validity of our parameter choices and model setup, we first test our likelihood function on the Henriques-C4 catalog. Given that we know the cosmology the catalog has been generated from, we expect to recover the underlying simulation cosmology within our errors. This check also allows us to test the convergence time for our MCMC sampler. The priors we assume are specified in section 5.3.2. For this test we use the more restrictive prior on $\mathcal{F}_\beta = 0.65 \pm 0.02$. In Figure 5.3, we plot the 2-parameter marginalized posterior for Ω_M and σ_8. Both the 68% and 95% contours are shown, and we see excellent agreement with the underlying Millennium cosmology as shown in the solid lines and their intersection that fall well within the inner contour. This test includes the full likelihood model with estimated caustic masses that contain scatter in addition to C4 catalog systematics

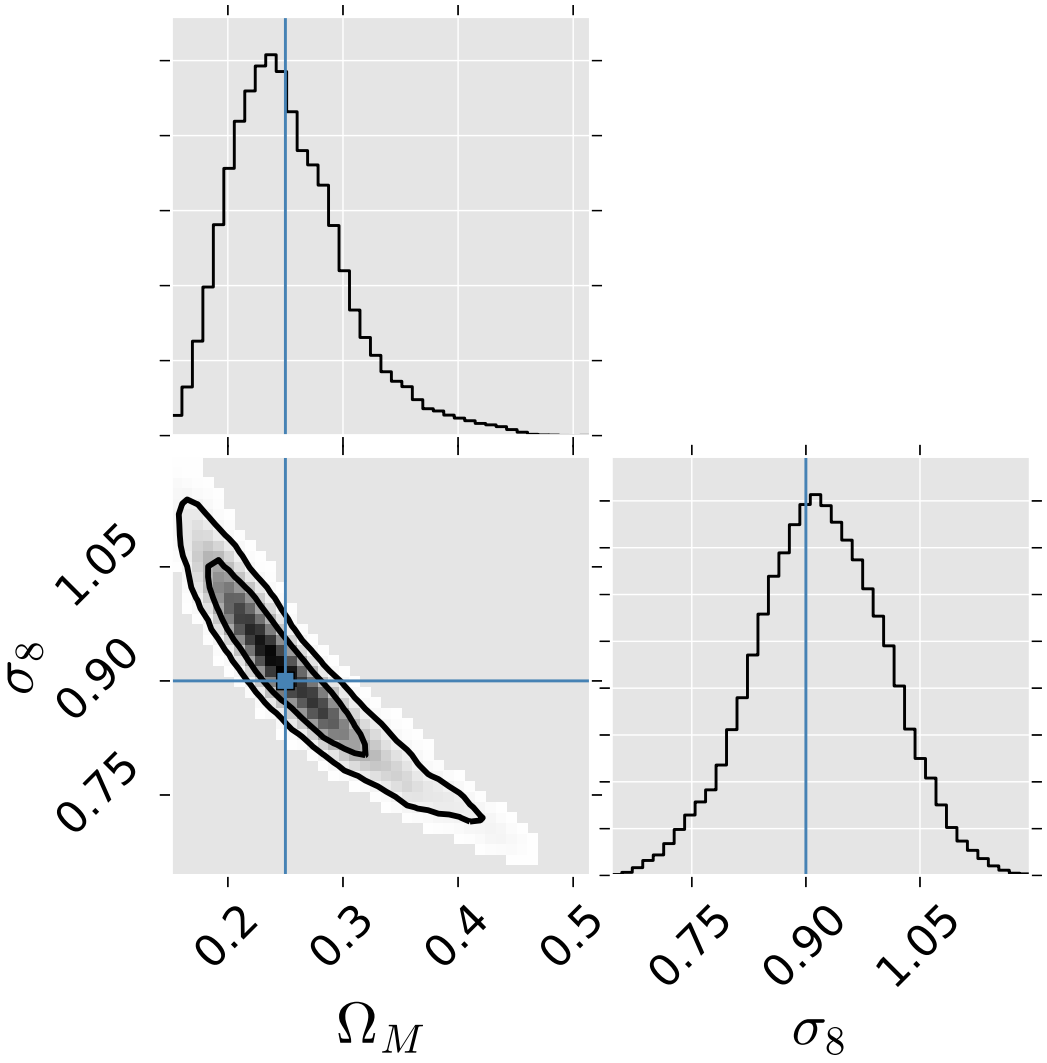

Figure 5.3: The inner and outer contours represent the 68% and 95% confidence regions for Ω_M and σ_8 when a mass scatter value of $60 \pm 10\%$ and $\mathcal{F}_\beta = 0.65 \pm 0.02$ is assumed. The histograms show the marginalized posterior distributions for each parameter. The vertical and horizontal lines show the cosmological conditions in the Millennium Simulation which our model should recover.

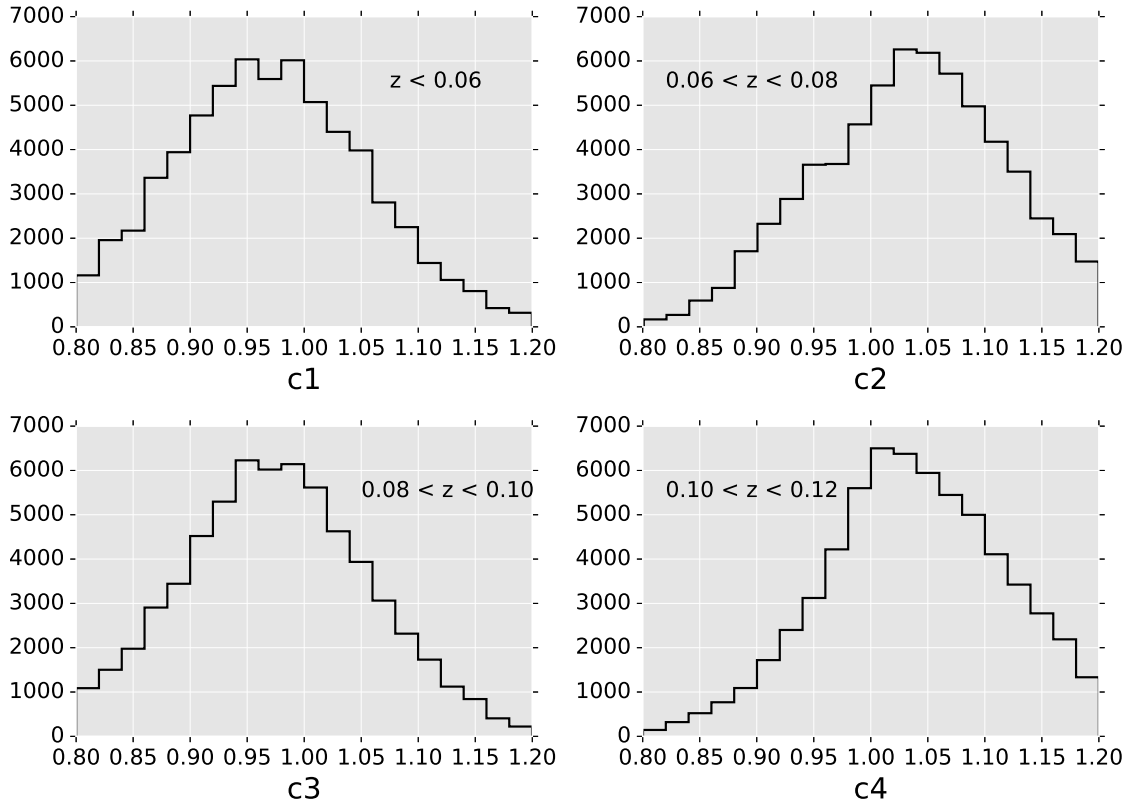

Figure 5.4: The marginalized posterior distributions for the completeness multipliers in our model that account for the statistical uncertainty in the completeness. The four parameters cover four redshift bins and are very close to 1.0 which we expect since we measure the completeness function directly in the simulation.

like purity and completeness. Based on this result, we see that there is some freedom in the parameters in our analysis that still allows the Millennium cosmology to fall within our confidence regions. In section 5.4.2 we investigate how changing our prior assumptions affects the cosmological results.

In addition to our four main parameters shown in figure 5.3, we can also inspect the marginalized posteriors for our nuisance parameters that act as multipliers with uncertainty on our completeness and purity functions discussed in section 5.3.2. We show the distributions for the four completeness multipliers in figure 5.4. The distributions for each parameter are very well constrained and narrower than the input

prior indicating the restrictive prior placed on these parameters does not play a major role. The values are also very close to 1.0 as we expect since we know the completeness function in the simulations. The posterior for the purity parameter recovers the flat input prior (not shown).

5.4.2 SDSS-C4 Mass Function

Based on the successful recovery of the Millennium simulation cosmology running our likelihood function on the Henriques-C4 catalog, we now run the same model on the SDSS-C4 catalog. The priors on $\mathcal{F}_\beta$, scatter, completeness, and purity are the same as described in section 5.3.2. In Figure 5.5, we present the 68% and 95% confidence contours and posterior distributions for 4 of the parameters in our model. The histograms show the marginalized posterior probabilities of each parameter. For the two cosmological parameters, we find the best fit to be $\Omega_M = 0.275$, $\sigma_8 = 0.83$. In Figure 5.6, we plot the best fit cosmology with respect to our cluster number counts as a function of estimated mass.

First, we investigate how our estimates in Ω_M and σ_8 compare with other studies. In Figure 5.7, we look at how our our confidence intervals look overplotted with Cosmic Microwave Background experiments Planck and WMAP confidence intervals. We find agreement to within our 68% contours with both the WMAP and Planck experiments. Our 68% constraints are barely consistent with the Planck estimates of Ω_M and σ_8. Based on our results, we cannot definitively rule in favor of a lower WMAP-like or higher Planck-like value of Ω_M.

We also compare our estimates with two other cluster mass function analysis (Vikhlinin et al., 2009; Rozo et al., 2010). Vikhlinin et al. (2009) used x-ray mass estimates for 86 clusters split between low and high redshift bins. Rozo et al. (2010) used the maxBCG catalog (Koester et al., 2007) and co-constrained a mass-richness relationship from the data. Seen in Figure 5.8, we find both studies overlap with

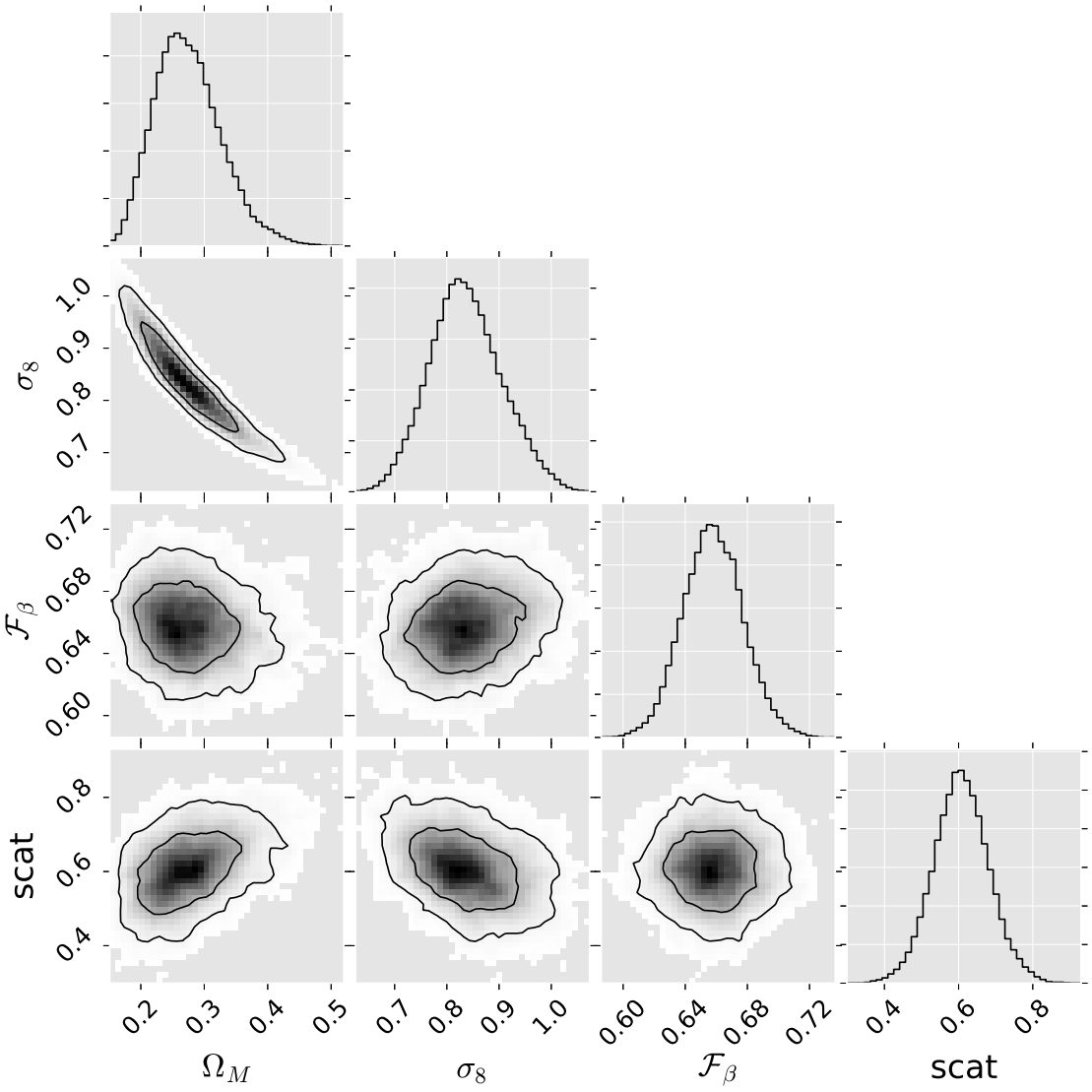

Figure 5.5: Constraints on our model parameters based on the SDSS-C4 mass function when a mass scatter value of $60 \pm 10\%$ and $\mathcal{F}_\beta = 0.65 \pm 0.02$ is assumed. The contours shown for each pair of parameters represents the 68% and 95% confidence intervals from our posterior probability distribution. The histograms represent the posterior distributions for each quantity marginalized over the other parameters.

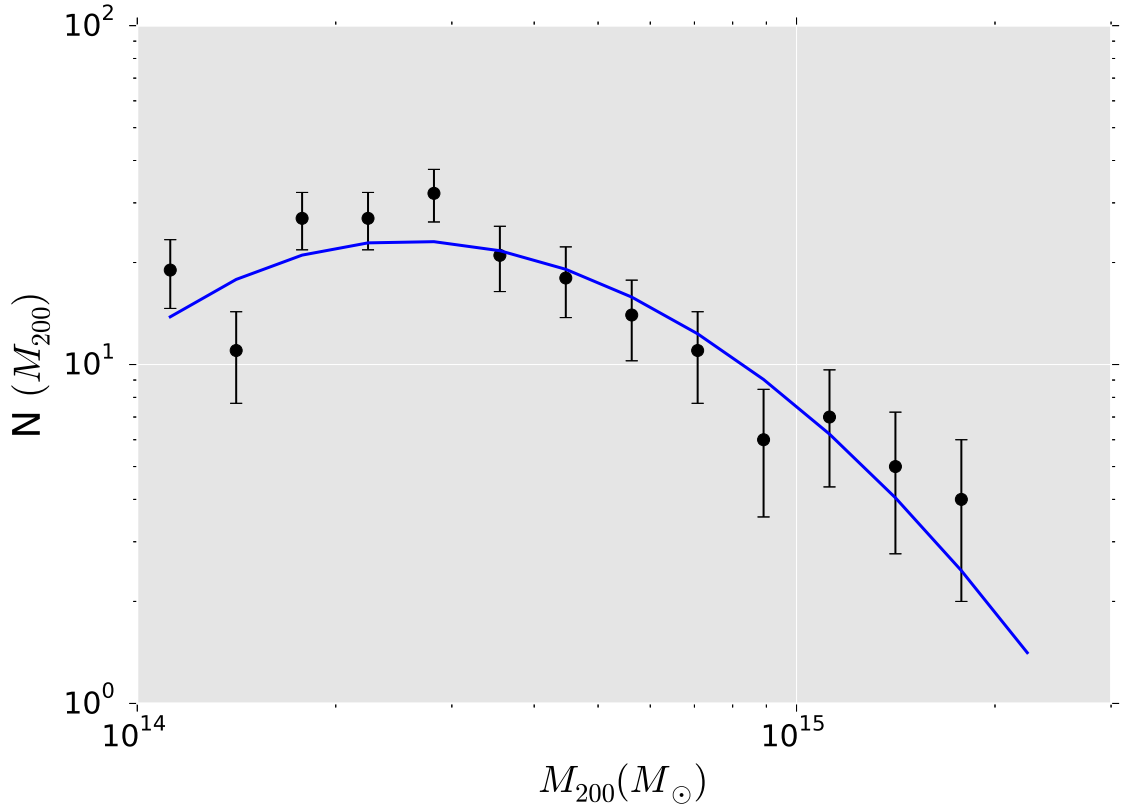

Figure 5.6: The SDSS-C4 mass function. The blue line is the best fit cosmology $\Omega_M = 0.275$ and $\sigma_8 = 0.83$. The posterior of $\mathcal{F}_\beta$ and the average scatter recovers the input prior of $\mathcal{F}_\beta = 0.65 \pm 0.02$ and $\langle\widehat{\kappa}\rangle = 0.6 \pm 0.1$. The error bars are simply illustrative of the statistical Poisson error in each mass bin and do not represent the total scatter due to systematics.

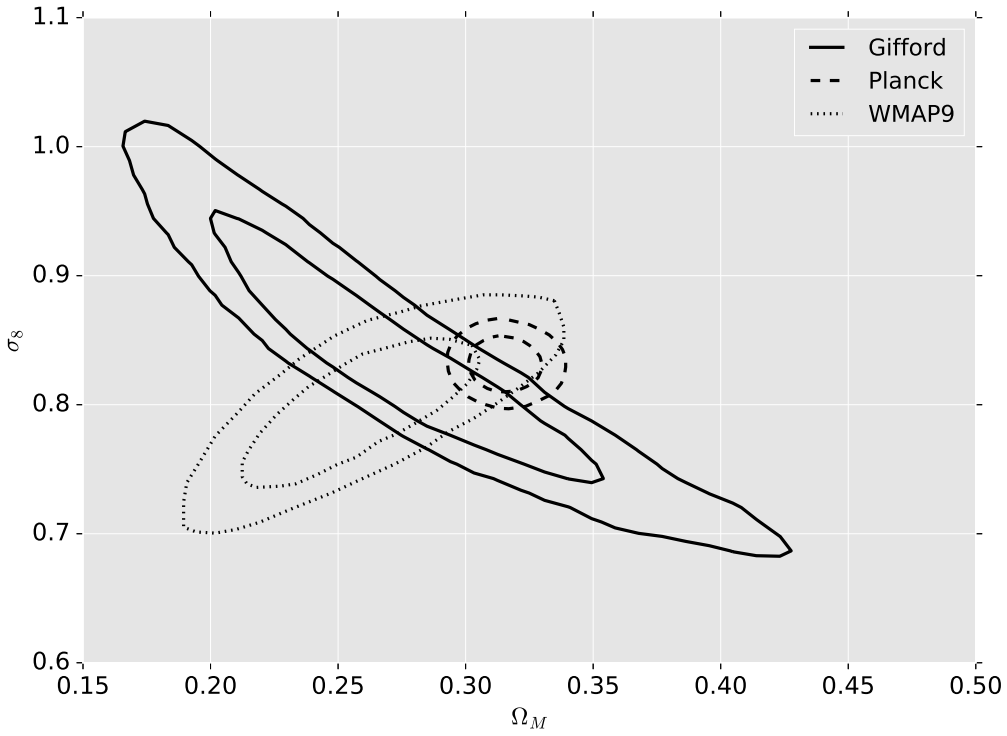

Figure 5.7: A comparison of cosmological constraints from our work (green), Planck (dashed), and WMAP9 (dotted). The inner and outer contours of each set represent the 68% and 95% contours of each experiment.

our confidence regions. Our contours are slightly narrower than Rozo et al. (2010) but agree with their findings. The confidence regions are larger than Vikhlinin et al. (2009), but offset slightly higher in Ω_M and σ_8. Interestingly, Vikhlinin et al. (2009) notes that systematically, their errors in mass could be up to 9% low. Making that correction results in an almost perfect agreement between the two confidence regions.

In literature, widely different values of $\mathcal{F}_\beta$, the normalization filling factor in front of the caustic equation, are still in use. Originally, Diaferio (1999) estimated its value at $\mathcal{F}_\beta = 0.5$ in simulations using identified subhalos as dynamical tracers. Later Serra et al. (2011) found a much larger value of $\mathcal{F}_\beta = 0.7$ described the mass profiles seen when using dark matter particles themselves as tracers of the gravitational potential. In Chapter III we investigate this difference and find that the disparate values are

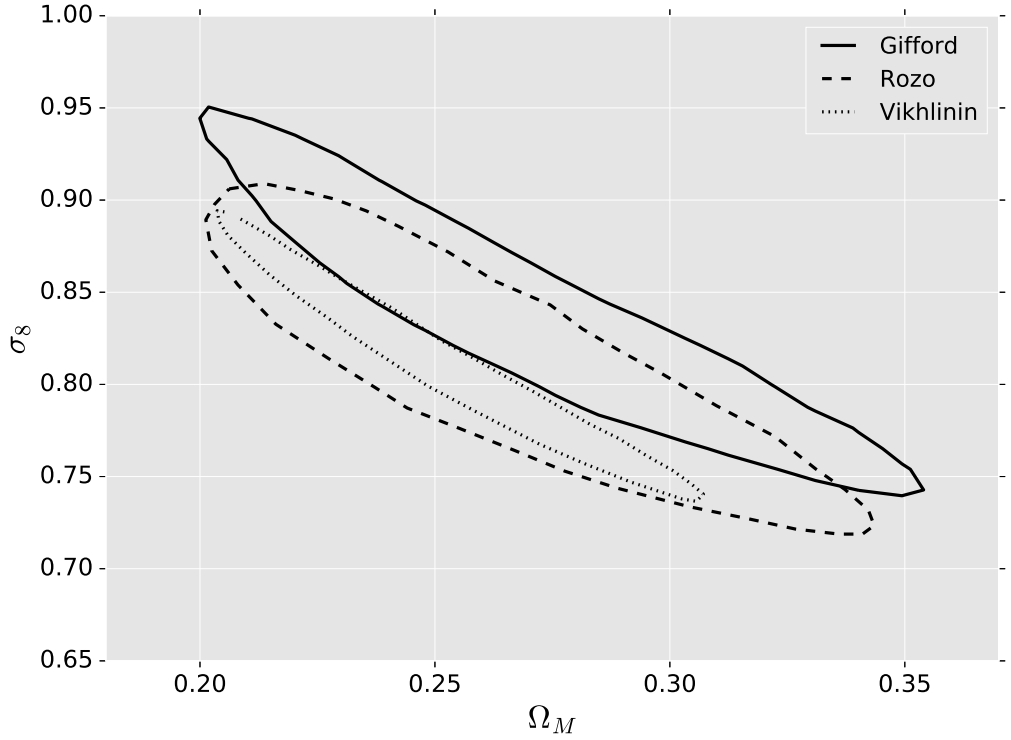

Figure 5.8: A comparison of cosmological constraints from our work (solid), Rozo et al. (2010) (dashed), and Vikhlinin et al. (2009) (dotted). The contours are the 68% confidence intervals and all experiments agree to within this uncertainty.

likely due to the large differences in velocity dispersion measured when using subhalos vs. particles in N-body simulations. In Chapter II we find that a value $\mathcal{F}_\beta = 0.65$, much closer to Serra's value best describes semi-analytic tracers in simulations. We also found that if we did use subhalo populations from the Millennium Simulation as dynamical tracers, using a value of $\mathcal{F}_\beta = 0.5$ would recover unbiased masses.

The above analysis is performed with a strict prior on $\mathcal{F}_\beta$ reflecting the uncertainty we estimate in chapter II. While we do not expect a large error on its value, we test for differences in our cosmological constraints when we relax our prior constraints on $\mathcal{F}_\beta$ from 0.65 ± 0.02 to ± 0.06 which is almost a 10% uncertainty. The results are shown in Figure 5.9. We see the marginalized posterior for $\mathcal{F}_\beta$ closely matches the contours of a more restricted prior on $\mathcal{F}_\beta$, but expands the confidence contours to higher values of σ_8 and lower values of Ω_M.

As in section 5.4.1, we show the marginalized posterior distributions for our nuisance parameters that act as multipliers to the completeness and purity functions to account for statistical uncertainty in these functions with redshift in Figure 5.10. These distributions look slightly different than those in Figure 5.4. The main reason is that the completeness and purity function is likely not exactly the same as our measured values in the simulation at every redshift due to statistical variation. Effects like cosmic variance also play a small role in this difference. The only bin that appears to deviate strongly from our expected completeness function is our lowest redshift bin ($c1$) which indicates we are overestimating the true completeness function in this bin.

5.5 Summary and Discussion

Cluster masses remain an ideal test of structure formation and evolution in our universe. Through the halo mass function, clusters provide tight constraints on the normalization of the power spectrum σ_8 and the matter density Ω_M. Using the halo

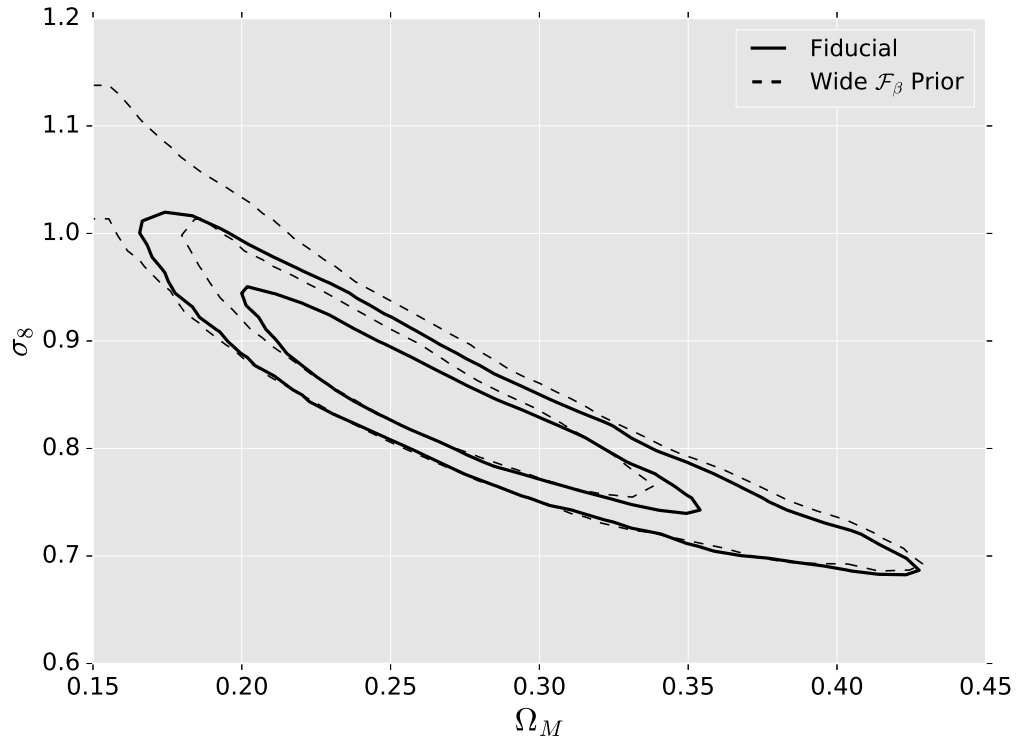

Figure 5.9: A comparison between using two different uncertainties on our prior for $\mathcal{F}_\beta$. The solid contours represent the 68% and 95% confidence regions for $\mathcal{F}_\beta = 0.65 \pm 0.02$. The dashed contours enclose the 68% and 95% confidence regions for $\mathcal{F}_\beta = 0.65 \pm 0.06$.

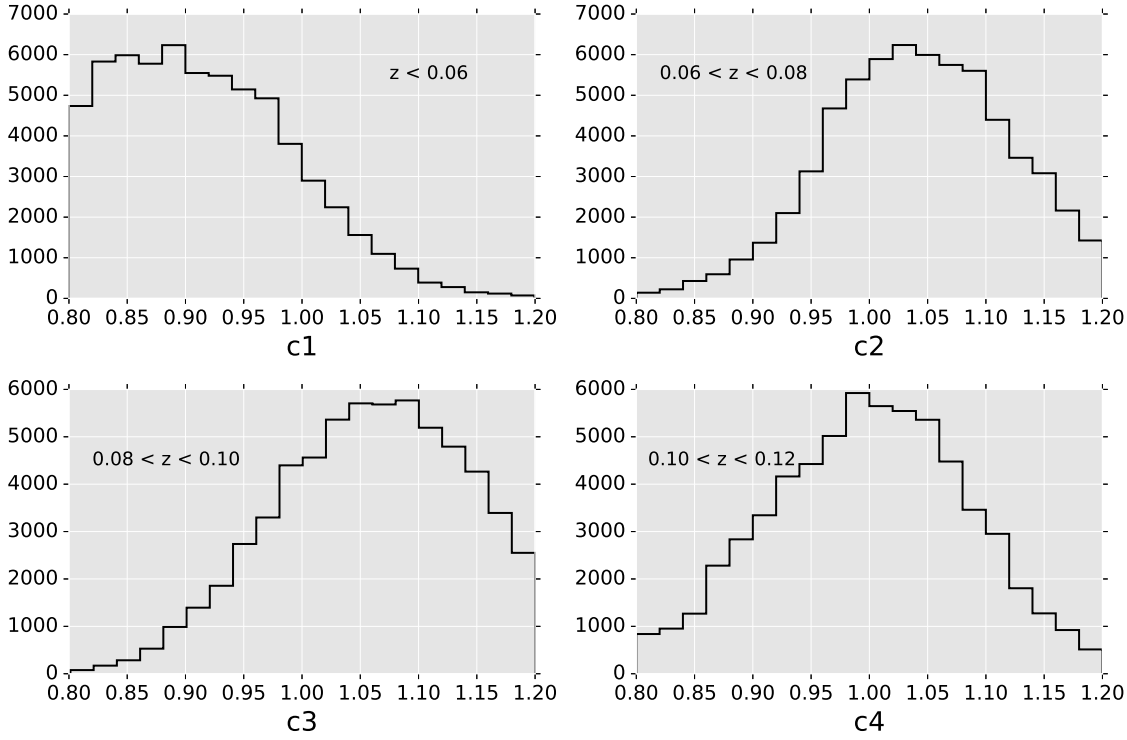

Figure 5.10: A comparison between using two different uncertainties on our prior for $\mathcal{F}_\beta$. The solid contours represent the 68% and 95% confidence regions for $\mathcal{F}_\beta = 0.65 \pm 0.02$. The dashed contours enclose the 68% and 95% confidence regions for $\mathcal{F}_\beta = 0.65 \pm 0.06$.

mass function to constrain cosmological parameters relies on accurate and precise estimates of cluster halo mass, which is not directly observable. While scaling relations with cluster observables like richness, velocity dispersion, X-ray luminosity, and SZ signal are excellent proxies of mass, they must be calibrated by a more direct mass estimator such as weak lensing, hydrostatic masses, or dynamical techniques.

Here we use the caustic technique to estimate cluster masses. The caustic technique has been shown in many circumstances to agree with other estimates of cluster mass (Diaferio et al., 2005; Rines et al., 2007; Sharon et al., 2015). In Chapter II, we complete an in-depth study into the systematics of the technique due to effects such as sampling and radial incompleteness of clusters. We perform a mass function analysis using caustic estimated masses for over 200 clusters in the SDSS-C4 cluster catalog. This is the largest dynamical mass function analysis to date. The goal of this analysis is to constrain the cosmological parameters Ω_M and σ_8 to compare with current state of the art mass function studies.

Using the halo mass function requires understanding the completeness and purity for the C4 cluster catalog as a function of both mass and redshift. To do so, we make use of the Henriques all-sky galaxy catalog built on the Millennium Simulation. We run the C4 algorithm over the Henriques sample and make cuts on richness and estimated mass of those clusters similar to the cuts we make in the SDSS-C4 data set. While we find that completeness is a strong function of both mass and redshift, the completeness in mass at a given redshift may be modeled with a log-linear relationship which allows us to push further down in mass than if the function was more complicated.

The mass scatter plays a large role in determining the shape and normalization of the mass function. Understanding its value is critical to pushing toward precision estimates of cosmological parameters. We use the Henriques-C4 sample to place constraints on the mass scatter we expect from our sample. By comparing the estimated

caustic masses against the true simulated halo mass for halos that are matched to the Henriques-C4 clusters, we find our estimates for mass are unbiased using a value for $\mathcal{F}_\beta = 0.65$ and exhibit a 60% average scatter that we use in the mass function analysis.

For the likelihood model, we use a no-binning technique that is described in Cash (1979). Within the model, we have 9 free parameters: the matter density Ω_M, power spectrum normalization σ_8, caustic filling factor $\mathcal{F}_\beta$, average sample scatter $\widehat{\kappa}$, 4 completeness parameters to account for uncertainty at different redshifts, and one purity parameter that accounts for its uncertainty. The cosmological parameters are treated as free, while the rest of the parameters are restricted. We find a best fit cosmology of $\Omega_M = 0.275$ and $\sigma_8 = 0.83$.

Like other cluster studies, we find agreement with both the WMAP 9 estimates of Ω_M and σ_8, but we also are consistant with the Planck experiment. Our 68% confidence intervals overlap with the same interval in both experiments but barely overlap with the Planck 68% confidence interval. One way to bring our cosmological estimates more in line with Planck would be if we are currently overestimating our completeness by $\sim$ 10%. Large cluster surveys out to higher redshifts and larger volumes will help clusters place tighter constraints on Ω_Λ in the future, and further support or explain the inconsistencies seen currently.

Future work involves better understanding the systematics which limit our mass estimates in large surveys like SDSS. Previous studies have looked at simulations in more ideal ways to estimate bias and scatter in the caustic technique. Improvements can be made by more carefully studying mock catalogs with real cluster finders run over the top like the one in this work. Improvements can come in identifying more clusters. The ability to do so is limited in the SDSS, but applications to the Dark Energy Survey and DESI will result in a wide range of new cluster mass estimates that are individually sampled more heavily than current surveys. Additional wavebands

may be used to more effectively eliminate interloper galaxies in the cluster projected phase-space, further increasing the precision of the technique.

CHAPTER VI

Conclusion

This work investigates the important statistical and systematic effects present when estimating virial masses with an escape velocity method termed the caustic technique. We systematically investigate the ideal scenario that the escape velocity can recover unbiased masses in both, and find that using the virial calibration in 3D does return unbiased masses with only $10-15\%$ scatter which is lower than the 3D mass-estimate scatter of $15-20\%$ presented in Evrard et al. (2008). We also test how the bias and scatter of the estimated caustic masses depends on a host of observational sampling choices such as color, magnitude, and radial completeness. Biases due to cluster redshift incompleteness is a major issue when it comes to estimating any dynamical mass, but is especially important to quantify when it comes to the caustic technique which relies on phase-space density. One way to overcome critical under-sampling of individual clusters that results in biased mass estimates is to stack similar systems into an ensemble phase-space and estimate a mean mass for the stack. Similar systems can be determined through observable mass-proxies such as richness or total luminosity that aren't dependent on redshift sampling/completeness. We develop a new way of directly detecting the projected escape velocity caustic in stacks to avoid velocity bias and recover an unbiased measurement of the mean ensemble mass. Finally, we use the C4 Cluster Survey on low redshift clusters to constrain Ω_M and

σ_8.

6.1 Observational Systematics

Until the work presented in this thesis, the only studies performed with the caustic technique in simulations estimated escape velocity surfaces and masses by randomly sampling particles (Serra et al., 2011; Svensmark et al., 2015) or using dark matter subhalos (Diaferio, 1999). Neither of these sampling techniques represent the phase-space distribution of galaxies in the real universe. This is due to astrophysical effects that include galaxy formation and evolution and dynamical friction. There are also simulation resolution effects that can alter the formation and break-up of subhalos further affecting the phase-space distributions. In Chapter II, we make use of four semi-analytic galaxy catalogs built on top of the Millennium Simulation (Guo et al., 2011; De Lucia & Blaizot, 2007; Bertone et al., 2007; Bower et al., 2006) to test the caustic technique against a variety of observational constraints. With 100 semi-randomly sampled clusters spanning a mass range of $10^{14} - 10^{15}$ $M_{\odot}$, we first test three separate interloper treatments to estimate cluster velocity dispersion and find a shifting-gapper technique utilizing both radius and velocity information works better than either sigma-clipping or simple bounded cuts in just velocity. Interloper removal is essential to the success of the technique as the escape velocity surface is calibrated using the estimated velocity dispersion.

One of the main results of the work presented in Chapter II is to understand how the bias and scatter in caustic mass vary with galaxy sampling. We downsample the cluster phase-space first in magnitude to mimic flux limited galaxy surveys and find that statistically, the caustic technique is an unbiased mass estimator when the phase-space contains 50 galaxies within r_{200}. We also apply a variety of other observational considerations such as only observing red galaxies or only blue galaxies and test mixing fractions of the two. More importantly, we test what happens to caustic mass

estimates when a cluster is radially incomplete. Surveys like SDSS must contend with fiber collisions in the dense cores of galaxy clusters, and sometimes the incompleteness due to a limited number of fiber orientations can be $< 70\%$. Likewise, for very large clusters, many of the galaxies in the outskirts may not be observed in a typical redshift survey of clusters due to observational constraints. We quantify the bias induced by these sampling systematics in the caustic mass.

By comparing with a virial scaling relation, we find that for a fixed number of tracers the caustic technique exhibits a lower amount of mass scatter and bias. Based on 4 semi-analytic galaxy populations in clusters, we also find an $\mathcal{F}_\beta = 0.65$ provides the most unbiased estimate on average for our systems. This is in conflict with the original value of $\mathcal{F}_\beta = 0.5$ by Diaferio (1999). We attribute this disparity to the difference in tracer populations used to estimate caustic surfaces. We use semi-analytic populations with velocity dispersions very close to the underlying dark matter distribution. Diaferio (1999) used subhalos which are known to produce biased (high) velocity dispersions and in turn, require a lower $\mathcal{F}_\beta$ to recover unbiased masses.

6.2 Theoretical Caustic Tests

Algorithmically, the foundation for the caustic technique was presented by Diaferio (1999) and later updated by Serra et al. (2011); however, neither study properly addresses the key theoretical underpinning of the technique itself: Does the caustic edge in 3D radius-velocity $(r - v)$ phase-space return unbiased masses when used in the caustic mass equation? In Chapter III, we test the caustic framework in several ways. First, we look into the role of cluster shape by fitting an NFW profile to both the density profile and escape velocity for each of our 100 clusters. The NFW parametrization contains 2 parameters: the density normalization ρ_0 and the scale radius r_0. When comparing the fits between the density and escape velocity, we find small differences that indicates the cluster potentials may be more spherical than

the density profiles. Based on this result, we find that if an NFW fit to the escape velocity is used to estimate mass, the mass bias is approximately -10%. We also find that uncertainties on the cluster concentration parameter have a small effect on the mass. On average, the NFW does a good job in fitting both the density and potential profiles as evidenced by the $\sim 10\%$ scatter in mass we measure with the technique in 3D.

We also test whether the caustic edge remains robust to tracers that exhibit "velocity bias". In N-body simulations, identified sub-halos within galaxy cluster sized halos exhibit a positive velocity dispersion bias of 10-20% (Wu et al., 2013). This bias mostly derives from the destruction of fast moving subhalos through the dense core of the cluster leaving only the slower infalling members to contribute to the dispersion measurement. In theory, the escape velocity surface will be immune to such effects, but such a test has not yet been performed. We test this by comparing the caustic edge using 3D radial velocities from subhalos and particles and find that by sub-sampling the particles to match the number of subhalos in bins of 3-dimensional radius. We find the particles and subhalos trace the same caustic surface out to $> 2r_{200}$. This is an important result as we show the caustic edge is the only dynamically based observable that is immune to velocity bias.

While previous authors have stated that the caustic technique does not depend on cluster virialization (Diaferio, 1999; Serra et al., 2011), this is simply not the case. Key to the caustic techniques algorithmic implementation is a calibration term that relates the velocity dispersion to the average escape velocity inside a radius of choice. The framework for such a calibration is presented in Binney & Tremaine (1987). Serra et al. (2011) argue the exact radius does not matter, and in Chapter III we test this statement. We find that the caustic calibration method does succeed for many radii (not just the exact radius where the virial condition $2T = -W$ applies), the appropriate offset to the velocity dispersion must be applied to account for the

inequality in the virial equation.

Observing clusters in projection adds a host of new uncertainties which must be carefully understood. When projecting galaxies along the line-of-sight, the velocity anisotropy of galaxy orbits must be taken into account. We test both an exact measured $\beta(r)$ for each halo and find the same scatter as seen in Chapter II when using a constant approximation of $\mathcal{F}_\beta$. We also study how the projected mass scatter and bias depend on various uncertainties in $\langle\beta\rangle$ and concentration. We find that both have a small effect on the estimated masses which we quantify in Chapter III.

6.3 Caustic Masses in Ensemble Clusters

In Chapter II, we discuss how the caustic technique is susceptible to statistical biases when the phase-space sampling drops below 50 galaxies. Many current surveys contain clusters with a few to tens of galaxies, but those clusters lack the galaxy numbers for dynamical techniques and may be too small for X-ray detection or weak lensing shear measurements, but do have observables such as richness that can be calibrated via scaling relations to mass and used for cosmological analysis. In Chapter IV, we develop and test a new stacking algorithm based on the caustic technique using an all-sky light cone in the Millennium Simulation (Guo et al., 2011; Henriques et al., 2012).

We first test the technique through a method called "self-stacking" where we build an ensemble cluster by sampling from the phase-space of a single cluster, randomly projected along multiple lines-of-sight (l.o.s) to the observer. Then, we move to stacking multiple clusters per bin and stack based on their true simulated halo mass. Finally, we remove knowledge of the halo mass and stack multiple cluster into ensembles based on a cluster observable. When creating an ensemble cluster, we vary both the number of galaxies sampled from each l.o.s, as well as the number of l.o.s. We find that when we achieve a total phase-space sampling of 1000, the ensemble

mass estimates are unbiased to within 5%. This is encouraging and suggests that when stacking, scatter in the mass-observable relationship does not play a large role in estimating the average of the individual masses. This makes calibration of mass-observable relationships possible. Stacking also shows very low mass scatter ($< 10\%$) when sampling of the ensemble phase-space is high.

6.4 SDSS-C4 Mass Function

In Chapter V, we measure the SDSS-C4 halo mass function. Cluster masses remain an ideal test of structure formation and evolution in our universe. Through the halo mass function, clusters provide tight constraints on the normalization of the power spectrum σ_8 and the matter density Ω_M. In order to use the halo mass function to constrain cosmological parameters, accurate and precise estimates of cluster halo mass, which is not directly observable, must be made.

We use the caustic mass technique to estimate cluster masses for over 200 systems in the SDSS-C4 cluster catalog and use them to measure the SDSS-C4 mass function. To do so, we make use of the Henriques all-sky galaxy catalog built on the Millennium Simulation to understand the systematics of our sample and test our likelihood analysis. We run the C4 algorithm over the Henriques sample and find that completeness is a strong function of both mass and redshift, and that the completeness in mass at a given redshift may be modeled with a log-linear relationship to fold through the likelihood analysis.

The mass scatter plays a large role in determining the shape and normalization of the mass function. Understanding its value is critical to pushing toward precision estimates of cosmological parameters. We use the Henriques-C4 sample to place only broad constraints on the mass scatter. By comparing the estimated caustic masses against the true simulated halo mass for halos that are matched to the Henriques-C4 clusters, we find our estimates for mass are unbiased using a value for $\mathcal{F}_\beta = 0.65$ and

exhibit a 60% average scatter that we use in the mass function analysis.

We find agreement to within our 68% confidence intervals with both WMAP and Planck. However, the contours agree more with WMAP than Planck, and in order to bring our estimates more in line with the latest results, we must be overestimating our completeness by $\sim 10\%$. Large cluster surveys out to higher redshifts will help clusters place tighter constraints on Ω_Λ in the future, and further support or explain the inconsistencies seen currently. We also see agreement with previous mass function studies using richness and x-ray based mass estimates. Finally, we test our prior assumptions and find that loosening our prior on the parameter $\mathcal{F}_\beta$ increases our uncertainty but does not change our maximum likelihood estimate.

6.5 Future Work

A great deal of progress has been made in the last 10 years on constraining the cosmology that governs our universe; however, the next decade and beyond promises to herald a new age in precision cosmology. The Sloan Digital Sky Survey has set the bar for wide photometric and spectroscopic samples in the optical, but now surveys across almost every available waveband in astronomy are opening up new windows of opportunity for scientific discovery. In the optical and near-infrared, current surveys such as the Dark Energy Survey (The Dark Energy Survey Collaboration, 2005) and DESI (Levi et al., 2013), and future planned surveys such as with WFIRST (Green et al., 2011) and the LSST (LSST Science Collaboration, 2009) will greatly expand the depth of photometric and spectroscopic coverage both in our local universe and well into the past. These results will enable precision cosmology through multiple independent studies including lensing, large-scale structure and Baryonic Acoustic Oscillations, dynamics within and in the outskirts of clusters, and standard candle cosmology with TypeIa Supernovae. At longer wavelengths, the South Pole Telescope has produced a large cluster catalog (Bleem et al., 2015) with SZ measurements that

shows promise when combined through dynamics or weak lensing in scaling relations (Hasselfield et al., 2013).

Galaxy clusters have a major role to play in understanding the universe at large, but much of what remains to be learned involves careful study of the cluster environment. Once thought to be rather simple systems, the dynamics of the baryonic components of galaxy clusters has turned out to be far more complex. With dynamics, understanding and modeling the phase-spaces of clusters may prove to be an excellent way of understanding the gravitational potential in the cluster. New experiments tracing the escape velocity surface to the cluster outskirts can probe alternative theories of gravity and possibly constrain cosmological parameters. The gas in clusters has been shown to be extremely correlated with halo mass (Ettori et al., 2012), but many challenges remain in understanding the various issues surrounding heating and cooling, turbulence and magnetic fields, and substructure. The improvements in hydrodynamic and magneto-hydrodynamic simulations in the coming years will improve our understanding of the baryonic astrophysics in clusters.

As for mass estimation, all techniques from lensing to x-ray to dynamics will benefit from the large spectroscopic and photometric surveys mentioned above. Deeper spectroscopic sampling and photometry in a greater number of wavebands will help refine algorithms aimed at identifying member galaxies thereby raising the accuracy of velocity dispersion estimates. They will also sharpen models for photometric redshift estimation used by weak lensing studies to better constrain the shear profiles of clusters. Finally, they will assist in following-up and confirming x-ray cluster detections. Combined, these methods will all assist in calibrating observable-mass scaling relations in the optical, x-ray, and SZ.

APPENDIX

APPENDIX A

OSMOSreduce: Automated Multi-object Spectrograph Data Reduction

OSMOS Imager and Spectrograph

The OSMOS (Ohio State Multi-Object Spectrograph) is a multi-object spectrograph and imager with a wide field of view on the 2.4m Hiltner Telescope, part of the MDM observatory on Kitt Peak, AZ. OSMOS has a nearly 20' FOV and can be equipped with either the MDM4K or R4K detector systems which cover 18.5' x 18.5' square. Both detectors are 4k devices with 15μm pixels. The MDM4K is more sensitive toward the blue and the R4K is more sensitive in the red. The R4K also has a much higher rate of cosmic ray events. In imaging mode, the all-refractive design projects a plate scale of 0.273" per pixel. There is a wide array of filters currently available including standard UBVRI, Sloan ugriz, and DES i,z,Y.

Here, I will focus on the spectrograph mode that enabled data collection for the purposes of this thesis. Spectroscopy can performed in two modes: Long slit with 0.9, 1.2, 1.4, 3, and 10 arcsecond wide slits available, and multi-slit with masks that are designed by the observer before-hand and are laser-cut into electroformed spherical

shells of NIColoy coated with Copper Oxide (CuO) black. OSMOS contains a 6-position slit wheel that the observer is capable of loading and unloading. Three dispersers are available in the instrument: A triple-prism with R = 100-400 with highest resolution in the UV, the VPH grism R=1600, and a Red grism. Acquisition software is available at the telescope to align and rotate the instrument relative to the observer's targets which can be a difficult task in multi-slit mode.

OSMOSReduce Reduction Pipeline

Multi-object spectroscopy data is saved into .FITS format and must be reduced by the observer. OSMOS masks can contain upwards of 50 slits depending on the size and placement of the slits during the mask design stage. For galaxy clusters, we managed to observe 20-35 galaxies per mask due to the high density of our objects. Currently, the only reduction code available for OSMOS works to correct for the detector bias and was written by the instrument PI Paul Martini. The task of cutting out the slits, distortion correction, source reduction, wavelength calibration, sky subtraction, and redshift estimation is left to the observer. To standardize the reduction process, I created a pipeline titled OSMOSReduce. I implemented this reduction pipeline in Python + ds9 with a range of automated and user controlled tasks to go from raw .FITS format to wavelength calibrated, 1d spectra with optional redshift estimation through a complimentary package I developed titled Zpy. Here, I will walk through the pipeline capabilities with sample screen shots throughout the process. Complete documentation will eventually exist with the code as it is currently open source and may be altered for use at different facilities.

Input requirements

When at the telescope, there are several observations one typically records to assist in the data reduction.

- Comps: These are taken of an arc lamp (Argon/Xenon/Helium/Neon) and are used to wavelength calibrate the spectra. In general we had success using the Argon and/or Xenon lamps for calibration spectra.

- Flats: To correct for detector inconsistencies, either twilight (sky flats) or illuminated screen flats will do.

- Science image(s): It is wise to take several science exposures to reduce detector noise. Our observations of low redshift galaxies require 2 x 30min integrations.

These images are pre-organized into directories by the user and read into memory using the FITS reader in the Astropy Python package (Astropy Collaboration et al., 2013).

There are two other necessary files that must be included in the directory structure. The first is the .OMS file produced during the mask making stage before the observing run. This file contains the physical XY chip positions, WCS on-sky coordinates, and slit shape parameters. OSMOSReduce uses these attributes to identify slits and label objects. The second is the image used during the mask design process to specify the location of the slits. This can be a mosaic or single finder image. Directions regarding file naming procedure and directory structure is present in the pipeline documentation.

Reading and Labeling the Data

The very first procedures run by OSMOSReduce include reading the cluster ID input, defining constants, and reading in the mosaic file. Then, the code will check and see if any bias reduced files exist. Paul Martini has kindly provided some initial reduction code written in Python called proc4k.py. I include this module in the OSMOSreduce package. This code performs the overscan subtraction and removes the relative gain differences for a single 4K image or a list of 4K images. OSMOSReduce

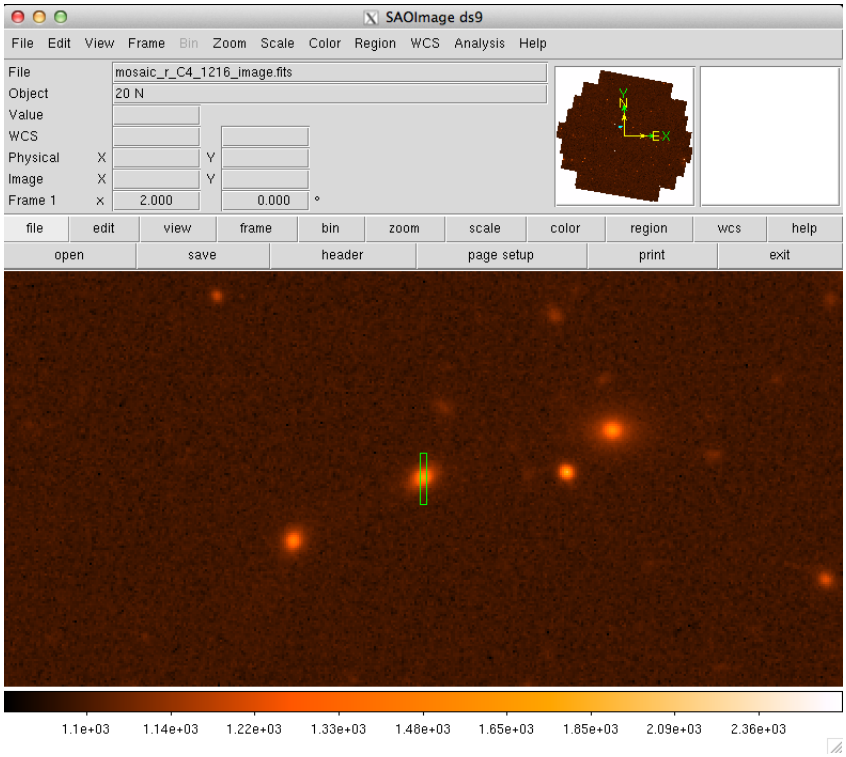

Figure A.1: Using ds9 to identify object types in each slit of the designed mask.

looks for the reduced files, and if they do not exist in the relevant directories, the files that are present are initially reduced with this module. Once reduced, the code reads in the reduced fits files. The code then parses the .OMS file for relevant information on the slits such as position in the x/y direction on the chip, RA/DEC on the sky, and slit width and length. All of these are saved into a Pandas Dataframe (McKinney, 2011) which will form the basis of our sample. Once we have the slit positions, the code utilizes a module called sqlcl.py developed by SDSS to query the SDSS database for information on the objects in the slits. The object information I query includes object id information, position, magnitudes, and spectroscopic and photometric redshifts. If more than 60 objects are needed (SDSS query limit per minute) or additional/different object features are desired, the source code may be edited.

After the images have loaded in ds9, ds9 will zoom in on the first slit on your mask and overlay its position on the mosaic image you have in the directory (see

Figure A.1). The user then uses a terminal window to answer the question if the slit is over a galaxy (g), reference star (r), or empty sky (s). These labels are used to decide which slits will be reduced later. Once you hit an appropriate key, the program will automatically move to the next object until you have run through all slits. This process only needs to be performed once per mask. If the reduction session is terminated before finishing, the results of this object labeling is saved to a file and read in if OSMOSReduce is re-run.

Identifying Dispersed spectra, Correcting Distortion, Object Identification, and Sky Subtraction

Once all slits have been labeled, the ds9 window will switch to a raw image of an arc lamp with all the dispersed light on the chip. Like before, the program will automatically zoom in on the first dispersed spectrum from a labeled galaxy and draw a long rectangular box approximately over the spectrum in ds9 (See Figure A.2). The user's job is to click+drag to move this box so that it encloses all the light from the slit. The user can also make the box wider to account for 'bending' spectra with the drag points on the corners of the green rectangle.

After choosing the area of the chip where the dispersed light resides from the slit, the program will automatically define the upper and lower edge of the dispersed light with a custom edge finding algorithm. The algorithm is intelligent that if parts of a neighboring slit are included in the region specified in ds9, it can identify the correct edges. A second-order polynomial is fit to both upper and lower edge, and the light inside the slit is "flattened" by correcting for this curvature (see Figure A.3).

Next, the program looks to identify the galaxy or object light in the flattened light from the slit. The happens by taking an average of the light along the long axis of dispersion to reveal where object is in y-position along the slit. The object light is fit with a Gaussian and the object is defined to occupy everywhere within 2σ of

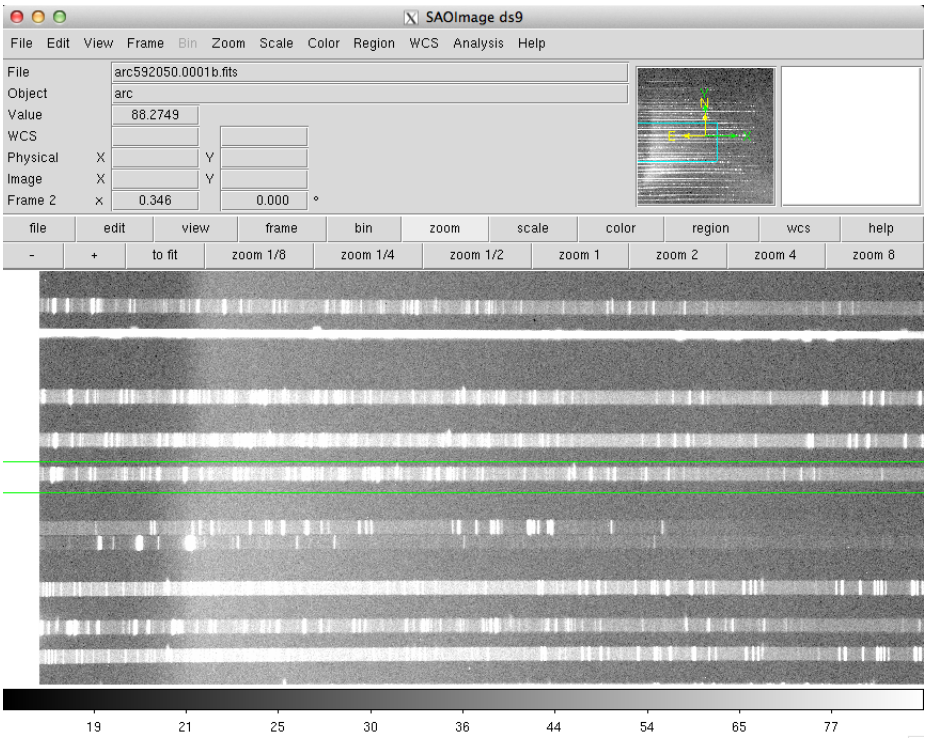

Figure A.2: Selecting the region of dispersed light for each slit on the CCD. Ds9 is used to create the regions.

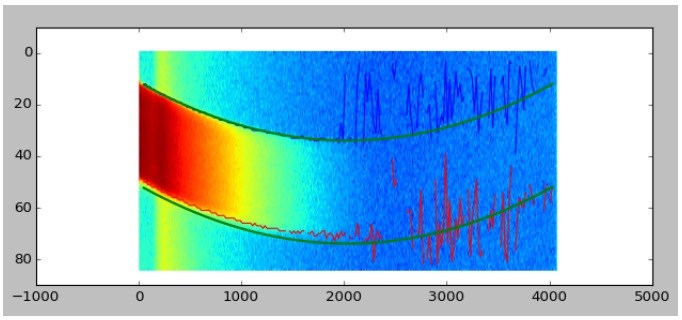

Figure A.3: Identifying the edges of the dispersed light. The curvature is due to optical distortion. The thin blue and red lines are the edges detected by the algorithm. The green lines are the final polynomial fit. The green line does not match the red because the distance between the two green lines must be equal to the size of the slit. This will offset the fit slightly.

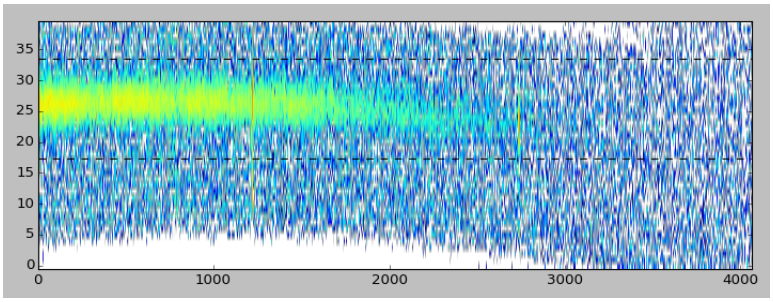

Figure A.4: The galaxy/object light is visible within the slit and outlined by black dashed lines by fitting the galaxy light with a gaussian.

the mean of the fit. The rest of the slit is treated as "sky" and is averaged along the short axis of dispersion to subtract from the object light. A 1d spectrum is created by summing the 2d object spectra along the short axis of dispersion.

The user will then answer the question if this is a good or bad spectra. If at any stage of this process the user does not feel this one object is not high enough quality for further reduction, they may stop the process by labeling this a bad spectra. Reasons may include: Inability to identify slit edges, inability to successfully flatten the slit light, or a bad object is identified in 2d spectrum. Once the question is answered it will move to the next object to repeat the process. Again, if after this stage is fully complete for all objects being reduced, the user may terminate the program at any time and the results of this stage are saved and reloaded with OSMOSReduce is restarted.

Wavelength Calibration

In the wavelength calibration stage of the reduction pipeline, the user now has sky-subtracted 1d spectra of each object as well as 1d spectra of the arc lamp through each slit. Wavelength calibration for multi-slit spectrographs can be tricky because slits are not only vertically separated, but are offset randomly in the horizontal chip direction as well. This means that each slit needs to be calibrated independently to find the correct pixel to wavelength mapping. Because of the large number of

observations we have performed with the OSMOS + VPH grism combination, we have effectively mapped the pixel to wavelength solution for every X-Y position on the chip (see Figure A.5). Due to changes in optics and CCD position, this solution is only approximate, but it allows for very quick processing during the next step of wavelength calibration.

Once the mapper returns an approximate solution for the first slit, the user walks through a two step process to exactly fit a 5th order polynomial to convert pixel values to wavelength using the 1d arc lamp spectrum. The first step is a rough alignment of the observed spectrum with the expected lines for each lamp. The automatic solution will get the user very close to the answer, but a handful of sliders are available to adjust the first 3 orders in the polynomial fit that moves the spectrum to refine the estimate (see Figure A.6 upper). Once this step is complete, the user will close the window and be taken to the exact fitting procedure.

In the exact fitting procedure, the user is walked line-by-line through the lines provided in the arc lamp calibration file. I have developed a peak finder using Scipy's (Jones et al., 2001–) signal module, and the program automatically guesses which peak should be matched to the current line. In Figure A.6 (lower), you can see the current line is on the left highlighted in a thicker red color, and the matched peak has a small orange circle over the peak. For each calibration line, the user can either accept the current peak-line match, select a different peak by clicking near the new peak in the GUI window, or deleting the current line from being used. Regardless of the choice, the program automatically steps to the next line and the process is repeated. Once enough lines are matched, the user may exit the process and a 5th order polynomial is fit to create a mapping for that particular slit. The user then repeats this process for all slits with galaxies/objects for all good spectra. For an experienced user, this step usually takes about 30 seconds per object. The solutions created here have an accuracy to within ~ 1 Angstrom which is consistent with the

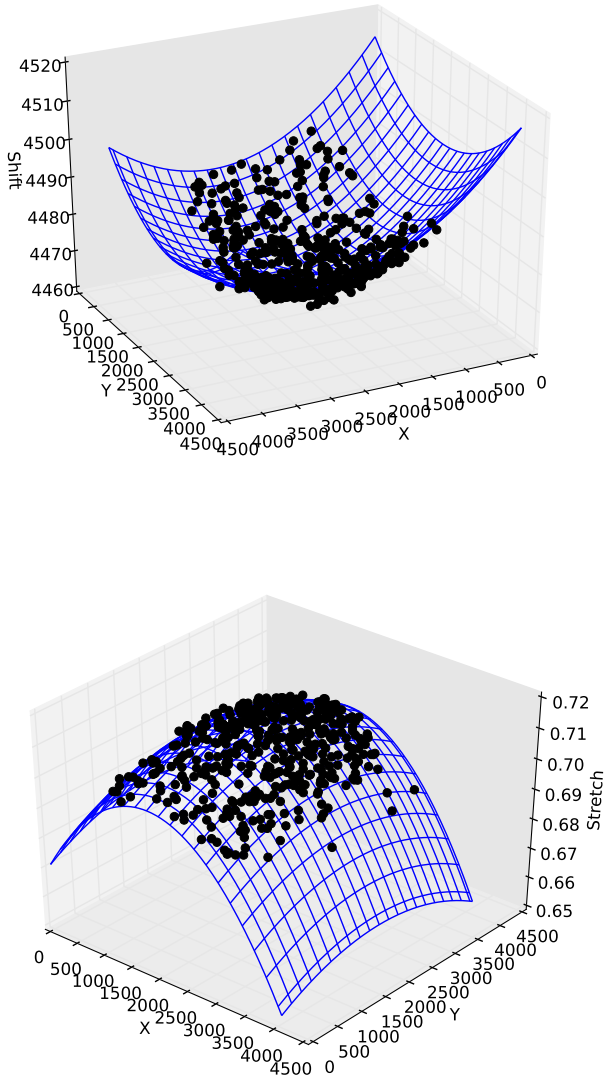

Figure A.5: An example of the the mapping coefficients (black dots) and our fits to those coefficients (blue mesh) for the "stretch" feature or zero-th order of our polynomial (**Upper**) and the "stretch" feature or the first order of our polynomial (**Lower**).

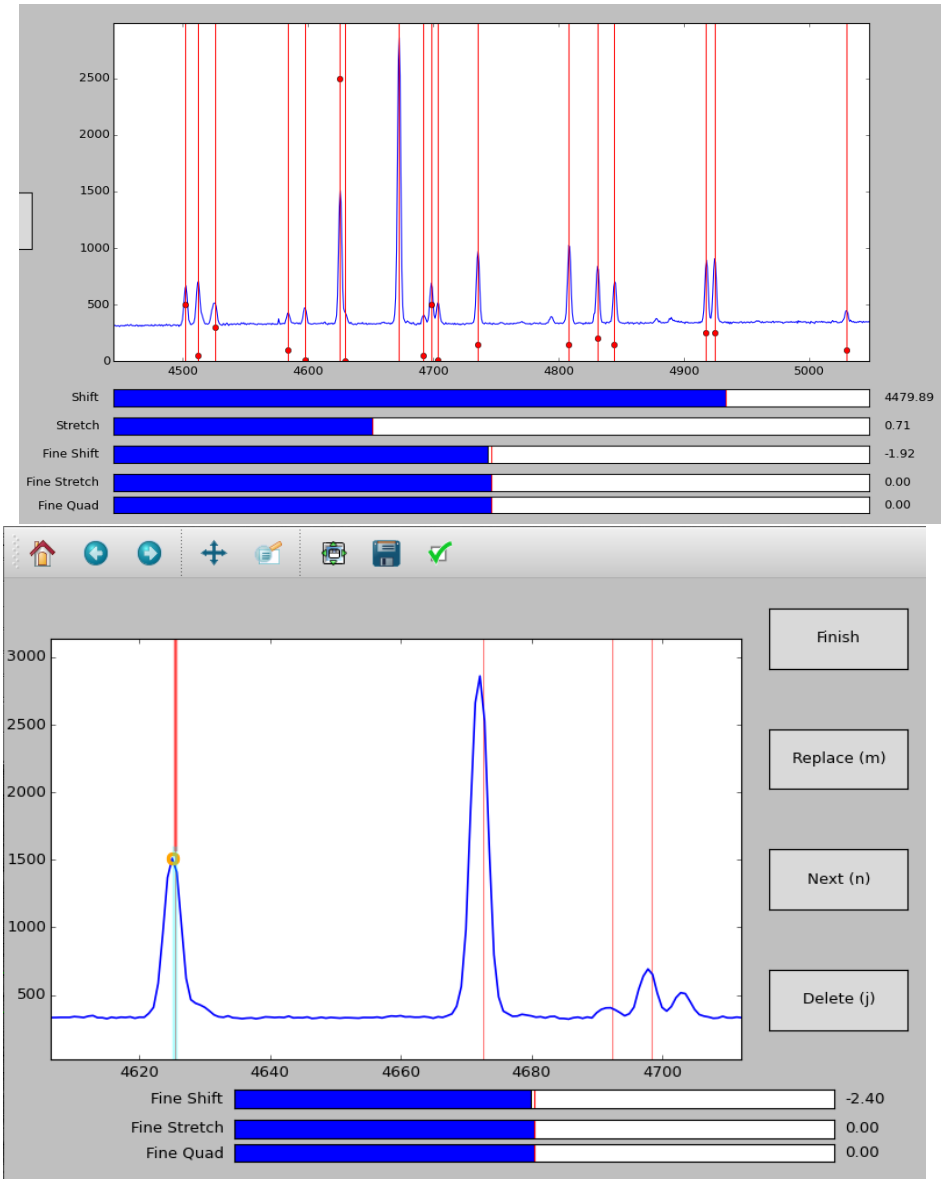

Figure A.6: Example windows of the GUI displayed during the two stages of wavelength calibration. In the first stage (**Upper**), the user uses several sliders to obtain an approximate match between the arc lamp lines expected (vertical red lines) and the observed arc spectrum (blue). In the second stage (**Lower**), the user clicks through the lines that match each expected spectral line in a semi-automated fashion to obtain a solid mapping solution from pixel to wavelength values for that position on the CCD.

result we see from redshift estimation.

Redshift Estimation

The final stage of the pipeline is to estimate redshifts for our objects. There are several ways to perform redshift estimation, but here I have implemented a cross-correlation technique with a template spectrum. For our galaxies, we have tested the code against an SDSS early-type galaxy template as most of our galaxies are red member galaxies of each cluster. The code helps the user measure an accurate redshift completely automatically in most cases, but here I describe potential scenarios the code is prepared to deal with.

The code first takes the template spectrum and shifts it based on a very fine grid in redshift and a correlation coefficient is measured between the continuum subtracted object and template spectra at each point in the grid. This is run automatically and, when completed for an object, a GUI is shown to the user with the object spectrum and the maximum-likelihood redshift with key absorption/emission features over-plotted with the correlation "likelihood" presented below (see Figure A.7). The GUI also allows the user to choose from a series of quality flags to be saved alongside the redshift estimate. This is useful for later when deciding which redshifts to trust from the reduction process. If the object has clear spectral features, the algorithm does an excellent job at recovering the object's redshift. For galaxies in the SDSS, we find an agreement to within 0.3% of the redshifts measured by SDSS. This works out to $< 60 km/s$ in velocity for the redshift of our systems which matches the uncertainties listed in SDSS. When spectral features are not visible, the algorithm does much worse, and the redshift estimate returned by the algorithm is not recommended for use.

Sometimes, the code will struggle to find the correct redshift for a given object, and the pattern matching abilities of the human brain will be a more trustworthy source. In this scenario, the user has the ability to right-click on the spectrum where

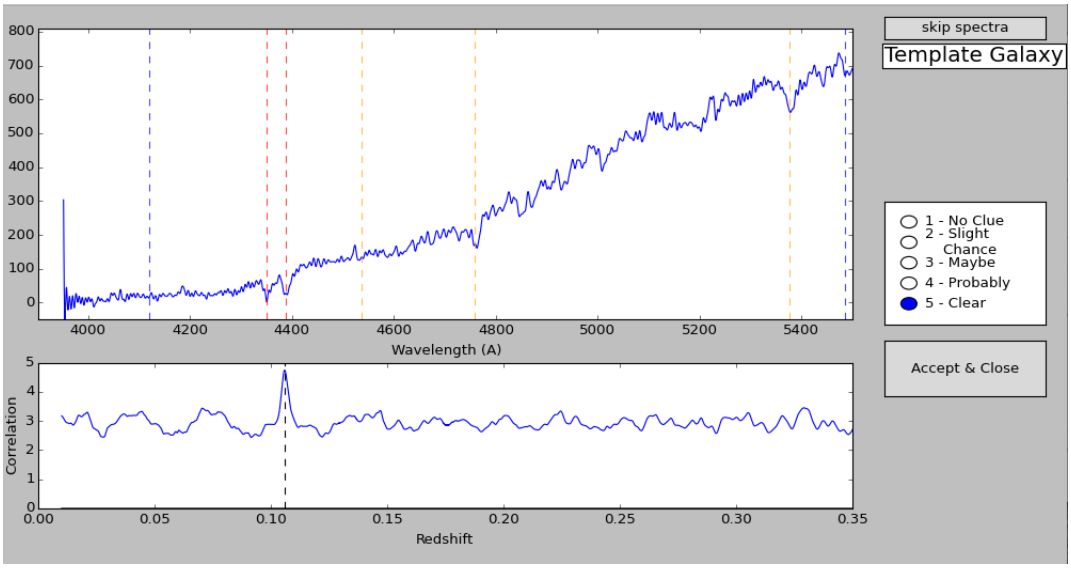

Figure A.7: An example of the redshift estimation GUI displayed during the final stage of reduction. The wavelength calibrated spectrum is plotted in blue in the upper half of the window, with a host of user specified spectral lines (redshifted based on the maximum likelihood value). The user may select a flag on the right side of the window indicating the accuracy/believability of the redshift estimate.

a familiar line is located. The line the user wants to default to in these scenarios is chosen at the beginning of the redshift estimation stage. For our purposes, the Ca H and K lines work well for this exercise with early type galaxies. Right clicking on the spectrum applies a "prior" of Gaussian shape centered on the redshift estimate with a $\sigma_z = 0.06$. This amplifies the correlation "likelihood" in the area specified by the user helping to pull out a particular solution. The new maximum-likelihood redshift is presented to the user (see Figure A.8). If this still fails to match the user's expectations, at this point the user may physically drag the spectrum left and right to match the expected spectral features. Unless the user is very confident in their estimate, the object redshift estimate should be discarded at this point. After all the objects have been reduced and redshifts have been estimated, the final results are written out to a csv file that may be used during analysis.

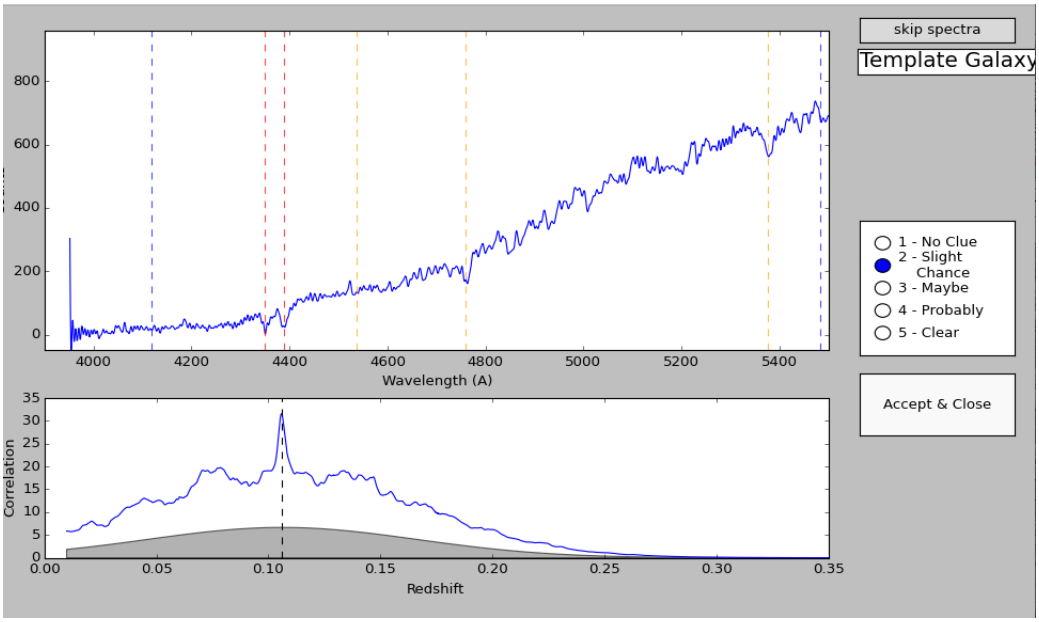

Figure A.8: An example of the redshift estimation GUI displayed during the final stage of reduction. The user select

BIBLIOGRAPHY

BIBLIOGRAPHY

Alam, S., et al. 2015, *ApJS*, 219, 12

Albrecht, A., et al. 2006, ArXiv Astrophysics e-prints

Alpaslan, M., et al. 2012, *MNRAS*, 426, 2832

Andreon, S., & Hurn, M. A. 2010, *MNRAS*, 404, 1922

Angulo, R. E., Springel, V., White, S. D. M., Jenkins, A., Baugh, C. M., & Frenk, C. S. 2012, *MNRAS*, 426, 2046

Astropy Collaboration, et al. 2013, *A&A*, 558, A33

Bahcall, N. A., & West, M. J. 1992, *ApJ*, 392, 419

Becker, M. R., & Kravtsov, A. V. 2011, *ApJ*, 740, 25

Becker, M. R., et al. 2007, *ApJ*, 669, 905

Beers, T. C., Flynn, K., & Gebhardt, K. 1990, *AJ*, 100, 32

Benson, B. A., de Haan, T., Dudley, J. P., et al. 2013, *ApJ*, 763, 147

Bertone, S., De Lucia, G., & Thomas, P. A. 2007, *MNRAS*, 379, 1143

Bett, P., Eke, V., Frenk, C. S., Jenkins, A., Helly, J., & Navarro, J. 2007, *MNRAS*, 376, 215

Biesiadzinski, T., McMahon, J., Miller, C. J., Nord, B., & Shaw, L. 2012, *ApJ*, 757, 1

Bigelow, B. C., & Dressler, A. M. 2003, in Society of Photo-Optical Instrumentation Engineers (SPIE) Conference Series, Vol. 4841, Instrument Design and Performance for Optical/Infrared Ground-based Telescopes, ed. M. Iye & A. F. M. Moorwood, 1727–1738

Binney, J., & Tremaine, S. 1987, Galactic dynamics, ed. Binney, J. & Tremaine, S.

Biviano, A., & Girardi, M. 2003, *ApJ*, 585, 205

Biviano, A., Murante, G., Borgani, S., Diaferio, A., Dolag, K., & Girardi, M. 2006, *A&A*, 456, 23

Biviano, A., & Poggianti, B. M. 2009, *A&A*, 501, 419

Blanton, M. R., et al. 2003, *ApJ*, 592, 819

Bleem, L. E., Stalder, B., de Haan, T., Aird, K. A., Allen, S. W., Applegate, D. E., et al. 2015, *ApJS*, 216, 27

Bocquet, S., Saro, A., Mohr, J. J., Aird, K. A., Ashby, M. L. N., Bautz, M., Bayliss, M., et al. 2015, *ApJ*, 799, 214

Borgani, S., et al. 2001, *ApJ*, 561, 13

Bower, R. G., Benson, A. J., Malbon, R., Helly, J. C., Frenk, C. S., Baugh, C. M., Cole, S., & Lacey, C. G. 2006, *MNRAS*, 370, 645

Bradač, M., Lombardi, M., & Schneider, P. 2004, *A&A*, 424, 13

Budzynski, J. M., Koposov, S. E., McCarthy, I. G., McGee, S. L., & Belokurov, V. 2012, *MNRAS*, 423, 104

Carlberg, R. G., Yee, H. K. C., Ellingson, E., Abraham, R., Gravel, P., Morris, S., & Pritchet, C. J. 1996, *ApJ*, 462, 32

Carlberg, R. G., et al. 1997a, *ApJ*, 485, L13

—. 1997b, *ApJ*, 476, L7

Cash, W. 1979, *ApJ*, 228, 939

Chandrasekhar, S. 1969, Ellipsoidal figures of equilibrium

Chang, C. L., et al. 2009, in American Institute of Physics Conference Series, Vol. 1185, American Institute of Physics Conference Series, ed. B. Young, B. Cabrera, & A. Miller, 475–477

Colberg, J. M., et al. 2000, *MNRAS*, 319, 209

Conway, J. T. 2000, *MNRAS*, 316, 555

Corless, V. L., & King, L. J. 2007, *MNRAS*, 380, 149

Davis, A. J., D'Aloisio, A., & Natarajan, P. 2011, *MNRAS*, 416, 242

Davis, M., et al. 2003, in Society of Photo-Optical Instrumentation Engineers (SPIE) Conference Series, Vol. 4834, Society of Photo-Optical Instrumentation Engineers (SPIE) Conference Series, ed. P. Guhathakurta, 161–172

De Lucia, G., & Blaizot, J. 2007, *MNRAS*, 375, 2

Dehnen, W. 1993, *MNRAS*, 265, 250

Diaferio, A. 1999, *MNRAS*, 309, 610

Diaferio, A., & Geller, M. J. 1997, *ApJ*, 481, 633

Diaferio, A., Geller, M. J., & Rines, K. J. 2005, *ApJ*, 628, L97

Dietrich, J. P., et al. 2014, *MNRAS*, 443, 1713

Dressler, A., et al. 2011, *PASP*, 123, 288

Driver, S. P., Hill, D. T., Kelvin, L. S., et al. 2011, *MNRAS*, 413, 971

Eikenberry, S., Elston, R., Raines, S. N., et al. 2006, in Society of Photo-Optical Instrumentation Engineers (SPIE) Conference Series, Vol. 6269, Society of Photo-Optical Instrumentation Engineers (SPIE) Conference Series

Einasto, J. 1969, Astronomische Nachrichten, 291, 97

Eisenstein, D. J., et al. 2011, *AJ*, 142, 72

Ettori, S., Rasia, E., Fabjan, D., Borgani, S., & Dolag, K. 2012, *MNRAS*, 420, 2058

Evrard, A. E., et al. 2008, *ApJ*, 672, 122

—. 2002, *ApJ*, 573, 7

—. 1996, *ApJ*, 469, 494

Fadda, D., Girardi, M., Giuricin, G., Mardirossian, F., & Mezzetti, M. 1996, *ApJ*, 473, 670

Faltenbacher, A., & Diemand, J. 2006, *MNRAS*, 369, 1698

Flaugher, B., et al. 2015, ArXiv e-prints

Foreman-Mackey, D., Hogg, D. W., Lang, D., & Goodman, J. 2013, *PASP*, 125, 306

Gavazzi, R. 2005, *A&A*, 443, 793

Geller, M. J., Diaferio, A., & Kurtz, M. J. 1999, *ApJ*, 517, L23

Geller, M. J., Diaferio, A., Rines, K. J., & Serra, A. L. 2013, *ApJ*, 764, 58

Gifford, D., Miller, C., & Kern, N. 2013, *ApJ*, 773, 116

Gifford, D., & Miller, C. J. 2013, *ApJ*, 768, L32

Goto, T. 2005, *MNRAS*, 359, 1415

Green, J., et al. 2011, ArXiv e-prints

Gruen, D., Seitz, S., Becker, M. R., Friedrich, O., & Mana, A. 2015, *MNRAS*, 449, 4264

Guo, Q., et al. 2011, *MNRAS*, 413, 101

Hasselfield, M., et al. 2013, *ApJS*, 209, 17

Henriques, B. M. B., White, S. D. M., Lemson, G., Thomas, P. A., Guo, Q., Marleau, G.-D., & Overzier, R. A. 2012, *MNRAS*, 421, 2904

Henry, J. P., Evrard, A. E., Hoekstra, H., Babul, A., & Mahdavi, A. 2009, *ApJ*, 691, 1307

Hoekstra, H., Hartlap, J., Hilbert, S., & van Uitert, E. 2011, *MNRAS*, 412, 2095

Hoekstra, H., Herbonnet, R., Muzzin, A., Babul, A., Mahdavi, A., Viola, M., & Cacciato, M. 2015, *MNRAS*, 449, 685

Hoessel, J. G., Gunn, J. E., & Thuan, T. X. 1980, *ApJ*, 241, 486

Host, O., Hansen, S. H., Piffaretti, R., Morandi, A., Ettori, S., Kay, S. T., & Valdarnini, R. 2009, *ApJ*, 690, 358

Jenkins, A., Frenk, C. S., White, S. D. M., Colberg, J. M., Cole, S., Evrard, A. E., Couchman, H. M. P., & Yoshida, N. 2001, *MNRAS*, 321, 372

Jones, E., Oliphant, T., Peterson, P., et al. 2001–, SciPy: Open source scientific tools for Python, [Online; accessed 2015-10-25]

Kaiser, N. 1987, *MNRAS*, 227, 1

Knebe, A., et al. 2011, *MNRAS*, 415, 2293

Koester, B. P., et al. 2007, *ApJ*, 660, 239

Kravtsov, A. V., Vikhlinin, A., & Nagai, D. 2006, *ApJ*, 650, 128

Lau, E. T., Nagai, D., & Kravtsov, A. V. 2010, *ApJ*, 708, 1419

Le Fèvre, O., et al. 2003, in Society of Photo-Optical Instrumentation Engineers (SPIE) Conference Series, Vol. 4841, Society of Photo-Optical Instrumentation Engineers (SPIE) Conference Series, ed. M. Iye & A. F. M. Moorwood, 1670–1681

Lemze, D., Broadhurst, T., Rephaeli, Y., Barkana, R., & Umetsu, K. 2009, *ApJ*, 701, 1336

Lemze, D., et al. 2012, *ApJ*, 752, 141

Levi, M., et al. 2013, ArXiv e-prints

Lima, M., & Hu, W. 2005, *Phys. Rev. D*, 72, 043006

Lin, Y.-T., Mohr, J. J., & Stanford, S. A. 2004, *ApJ*, 610, 745

LSST Science Collaboration. 2009, ArXiv e-prints

Mahdavi, A., Hoekstra, H., Babul, A., Bildfell, C., Jeltema, T., & Henry, J. P. 2013, *ApJ*, 767, 116

Mamon, G. A., Biviano, A., & Boué, G. 2013, *MNRAS*, 429, 3079

Mantz, A., Allen, S. W., Ebeling, H., Rapetti, D., & Drlica-Wagner, A. 2010a, *MNRAS*, 406, 1773

Mantz, A., Allen, S. W., Rapetti, D., & Ebeling, H. 2010b, *MNRAS*, 406, 1759

Martini, P., et al. 2011, *PASP*, 123, 187

Mateo, M., Bailey, J. I., Crane, J., Shectman, S., Thompson, I., Roederer, I., Bigelow, B., & Gunnels, S. 2012, in Society of Photo-Optical Instrumentation Engineers (SPIE) Conference Series, Vol. 8446, Society of Photo-Optical Instrumentation Engineers (SPIE) Conference Series, 4

McKinney, W. 2011

McLean, I. S., Steidel, C. C., Matthews, K., Epps, H., & Adkins, S. M. 2008, in Society of Photo-Optical Instrumentation Engineers (SPIE) Conference Series, Vol. 7014, Society of Photo-Optical Instrumentation Engineers (SPIE) Conference Series

McLeod, B. A., Fabricant, D., Geary, J., Martini, P., Nystrom, G., Elston, R., Eikenberry, S. S., & Epps, H. 2004, in Society of Photo-Optical Instrumentation Engineers (SPIE) Conference Series, Vol. 5492, Society of Photo-Optical Instrumentation Engineers (SPIE) Conference Series, ed. A. F. M. Moorwood & M. Iye, 1306–1313

Meneghetti, M., Rasia, E., Merten, J., Bellagamba, F., Ettori, S., Mazzotta, P., Dolag, K., & Marri, S. 2010a, *A&A*, 514, A93

—. 2010b, *A&A*, 514, A93

Merloni, A., et al. 2012, ArXiv e-prints

Merten, J., et al. 2015, *ApJ*, 806, 4

Miller, C. J., & Batuski, D. J. 2001, *ApJ*, 551, 635

Miller, C. J., Nichol, R. C., & Batuski, D. J. 2001, *ApJ*, 555, 68

Miller, C. J., Nichol, R. C., Genovese, C., & Wasserman, L. 2002, *ApJ*, 565, L67

Miller, C. J., et al. 2005, *AJ*, 130, 968

Mo, H. J., Jing, Y. P., & White, S. D. M. 1996, *MNRAS*, 282, 1096

Murray, S. G., Power, C., & Robotham, A. S. G. 2013, Astronomy and Computing, 3, 23

Nagai, D., Vikhlinin, A., & Kravtsov, A. V. 2007, *ApJ*, 655, 98

Navarro, J. F., Frenk, C. S., & White, S. D. M. 1997, *ApJ*, 490, 493

Neto, A. F., et al. 2007, *MNRAS*, 381, 1450

Pillepich, A., Porciani, C., & Reiprich, T. H. 2012, *MNRAS*, 422, 44

Planck Collaboration. 2011, *A&A*, 536, A10

Planck Collaboration, et al. 2014a, *A&A*, 571, A16

—. 2014b, *A&A*, 571, A20

—. 2015, ArXiv e-prints

Postman, M., et al. 2012, *ApJS*, 199, 25

Press, W. H., & Schechter, P. 1974, *ApJ*, 187, 425

Rasia, E., et al. 2006, *MNRAS*, 369, 2013

—. 2012, New Journal of Physics, 14, 055018

Reiprich, T. H., & Böhringer, H. 2002, *ApJ*, 567, 716

Retana-Montenegro, E., van Hese, E., Gentile, G., Baes, M., & Frutos-Alfaro, F. 2012, *A&A*, 540, A70

Rines, K., Diaferio, A., & Natarajan, P. 2007, *ApJ*, 657, 183

—. 2008, *ApJ*, 679, L1

Rines, K., Geller, M. J., Diaferio, A., & Kurtz, M. J. 2013, *ApJ*, 767, 15

Rines, K., Geller, M. J., Diaferio, A., Kurtz, M. J., & Jarrett, T. H. 2004, *AJ*, 128, 1078

Rines, K., et al. 2003, *AJ*, 126, 2152

Rozo, E., et al. 2010, *ApJ*, 708, 645

—. 2009, *ApJ*, 699, 768

Sahlén, M., et al. 2009, *MNRAS*, 397, 577

Saliwanchik, B. R., Montroy, T. E., Aird, K. A., Bayliss, M., Benson, B. A., et al. 2013, ArXiv e-prints

Saro, A., et al. 2015, *MNRAS*, 454, 2305

Saro, A., Mohr, J. J., Bazin, G., & Dolag, K. 2013, *ApJ*, 772, 47

Seitz, C., & Schneider, P. 1997, *A&A*, 318, 687

Serra, A. L., & Diaferio, A. 2013, *ApJ*, 768, 116

Serra, A. L., Diaferio, A., Murante, G., & Borgani, S. 2011, *MNRAS*, 412, 800

Sharon, K., et al. 2015, ArXiv e-prints

Shaw, L. D., Weller, J., Ostriker, J. P., & Bode, P. 2006, *ApJ*, 646, 815

Sheth, R. K., & Tormen, G. 1999, *MNRAS*, 308, 119

—. 2002, *MNRAS*, 329, 61

Song, J., Zenteno, A., Stalder, B., et al. 2012, *ApJ*, 761, 22

Springel, V., et al. 2005, *Nature*, 435, 629

Springel, V., White, S. D. M., Tormen, G., & Kauffmann, G. 2001, *MNRAS*, 328, 726

Stien, C. M. 1981, The Annals of Statistics, 9, 1135

Stoughton, C., Lupton, R. H., Bernardi, M., et al. 2002, *AJ*, 123, 485

Svensmark, J., Wojtak, R., & Hansen, S. H. 2015, *MNRAS*, 448, 1644

The Dark Energy Survey Collaboration. 2005, ArXiv Astrophysics e-prints

Tinker, J., Kravtsov, A. V., Klypin, A., Abazajian, K., Warren, M., Yepes, G., Gottlöber, S., & Holz, D. E. 2008, *ApJ*, 688, 709

Vanderplas, J., Connolly, A., Ivezić, Ž., & Gray, A. 2012, in Conference on Intelligent Data Understanding (CIDU), 47 –54

Vikhlinin, A., et al. 2009, *ApJ*, 692, 1060

von der Linden, A., et al. 2014, *MNRAS*, 439, 2

Wang, Y., Yang, X., Mo, H. J., van den Bosch, F. C., Weinmann, S. M., & Chu, Y. 2008, *ApJ*, 687, 919

Warren, M. S., Abazajian, K., Holz, D. E., & Teodoro, L. 2006, *ApJ*, 646, 881

White, M., Cohn, J. D., & Smit, R. 2010, *MNRAS*, 408, 1818

Wing, J. D., & Blanton, E. L. 2011, *AJ*, 141, 88

Wojtak, R., & Łokas, E. L. 2010, *MNRAS*, 408, 2442

Wu, H.-Y., Hahn, O., Evrard, A. E., Wechsler, R. H., & Dolag, K. 2013, *MNRAS*, 436, 460

York, D. G., et al. 2000, *AJ*, 120, 1579

Zwicky, F. 1933, Helvetica Physica Acta, 6, 110